Universitat de Barcelona

On the characterisation of the Galactic warp in the Gaia era

Hoda Abedi

Universitat de Barcelona
Departament d'Astronomia i Meteorologia

On the characterisation of the Galactic warp in the Gaia era

Memòria presentada per
Hoda Abedi

per optar al grau de
Doctor en Física

Barcelona, Febrer de 2015

Programa de doctorat en Física
Línia de recerca en Astronomia i Astrofísica

Memòria presentada per
Hoda Abedi

per optar al grau de
Doctor en Física

Directors de la tesi:

Dra. Francesca Figueras
Dr. Luis A. Aguilar

Tutora de la tesi:

Dra. Francesca Figueras

Acknowledgement

I would like to thank my supervisors Francesca Figueras and Luis Aguilar for all I have learned from them. You both are the best teachers any student can ask for. Thank you Francesca for all of your support and patience, aspiring guidance and immense knowledge. You always made time to help and advise me. I have been a pleasure for me to work with you. Also, I really appreciate you being so sensitive and supportive towards women's right. Thank you Luis for being such an incredible teacher and making the most complicated topics in dynamics so simple to learn. You are a brilliant astronomer and it has been an honour for me to work with you.

I also would like to thank Mercè Romero for her help specially during the first year of my PhD to learn different tools needed for our test particle simulations. I want to thank Cecilia Mateu for her constant help and precious contribution to our paper. I wish to thank Martin López-Corredoira and Francisco Garzón for our fruitful collaboration. Especially I would like to thank Martin for his valuable help and sharing his knowledge with us.

I want to thank the Gaia team at the UB, especially Jordi Torra, Carme Jordi, Xavi Luri, Claus Fabricius, Lola Balaguer, Josep Manel Carrasco and Jordi Portell from whom I learnt a lot about all different aspects of the Gaia mission. I especially would like to thank Lola who always greet me with a smile and help me with all different administrative work even when she was loaded with work. Thanks Dani for being so kind and fixing all the problems I faced with my machine. Santi, Maria M., Roger and Laia, thanks for our productive science meetings and all of your help during these years. Nora, Juanjo, Raul, Javier and Marcial, thank you for making our Gaia team a happy, fun and productive team. Erika and Max, thanks for being such a sweet, caring and supportive friends during these years.

Thanks to all the great scientists involved with the GREAT-ITN network for all of your efforts. I consider myself very lucky to be a part of this training program. I learned a lot during all of schools, workshops and conferences. Nadia, Iulia, Carmen, Cheng, John, Fabo, Lovro, Matty, Tristan, Tatyana, Toni, Lisa, André, Sergi and Alejandra, thanks for creating such a fun, friendly and motivating atmosphere in all of our meetings. I am going to miss our GREAT group.

I want to thank Tsafi, Rien, Iris, Allon, Wouter and Milou for their love and care and for welcoming me into their wonderful family. I would especially like to thank my amazing parents for their love and support in the moments of joy and pain and my brothers, Soroush and Soheil

for being the sweetest, funniest and the most caring. Finally, I want to thank the love of my life and my best friend, Edo. Without your emotional and spiritual support, I could not have done this work. I can not wait to spend rest of my life with you under the same roof.

Resum en Català

Els discs de les galàxies són fins i plans, però acostumen a presentar una curvatura a la seva part externa. Des de mitjans del segle XX, quan varen començar a ser disponibles les primeres mesures de la línia de 21 cm de l'hidrogen neutre, es va poder observar aquesta forma corbada a la nostra galàxia (Burke 1957; Kerr et al. 1957; Westerhout 1957; Oort et al. 1958, entre d'altres). Aquests estudis independents mostren que la desviació vertical del pla supera els 300 pc a distàncies galactocèntriques de 12 kpc. Més recentment, Reylé et al. (2009), a partir de mesures de la distribució de la pols i les estrelles, utilitzant dades del Two Micron All Sky Survey (2MASS) en l'infraroig proper, troben que la component estel·lar, en primera aproximació, es pot modelitzar per una forma en S (S-shaped warp) amb una pendent significativament inferior a la observada amb l'hidrogen neutre. Aquests autors també troben que el pendent de la component de pols te un valor intermedi entre el pendent de la component estel·lar i la de gas. A més, obtenen que el radi on comença la forma corbada és aproximadament 8.4 kpc. Diversos autors han provat d'estimar l'angle de fase de la línia dels nodes en respecte a la línia Sol – centre galàctic. Els valors obtinguts estan dins el rang $\sim -5^\circ$ (López-Corredoira et al. 2002) i $\sim 15^\circ$ (Momany et al. 2006). Mentre que els estudis que utilitzen els recomptes estel·lars ens proporcionen un ajust als paràmetres geomètrics de la curvatura, és clar que la cinemàtica de l'aquesta component estel·lar s'ha d'ajustar amb d'altres models de curvatura més complexes.

Utilitzant els catàlegs de moviments propis Hipparcos i Tycho-2, diversos autors han provat d'estudiar la empremta cinemàtica d'aquesta curvatura del disc galàctic (Miyamoto & Zhu 1998; Drimmel et al. 2000; Bobylev 2010, entre d'altres). Per exemple, (Drimmel et al. 2000), analitzant els moviments propis de les estrelles OB, van concloure que la cinemàtica observada en la direcció de l'anticentre galàctic era inconsistent amb l'esperada per una curvatura estable, de llarga durada i no transitòria. Per aquestes curvatures s'espera un moviment vertical positiu cap a l'anticentre, però a partir d'aquestes dades aquests autors obtenen un moviment vertical sistemàticament negatiu. Discuteixen que aquesta tendència podria ésser explicada o bé mitjançant una curvatura amb un moviment de precessió important o per l'existència d'un error sistemàtic significatiu en les distàncies fotomètriques. Aquests estudis ens mostren la dificultat que tenim a dia d'avui d'extreure i separar l'empremta cinemàtica de la curvatura d'altres efectes pertorbadors propers i locals. Ara, iniciada la dècada de Gaia, s'obre una nova dimensió no explorada, el poder disposar de bona precisió cinemàtica dels diferents traçadors estel·lars que participen de la curvatura galàctica a radis galactocèntric grans, superiors al radi solar.

En aquesta tesis explorem aquesta dimensió mitjançant el desenvolupament d'un nou model cinemàtic per la curvatura galàctica. Ens proposem analitzar les capacitats de caracteritzar la curvatura que se'ns obriran en un futur immediat donada l'alta qualitat astromètrica que tindran les dades que ens oferirà Gaia.

En aquesta tesi volem avaluar la capacitat de diversos mètodes estadístics de identificar i caracteritzar la curvatura del disc estel·lar de la Galàxia en la era de Gaia. Per portar a terme aquests objectius hem utilitzar una família de mètodes estadístics anomenats Great Circle Cell Counts (GC3). Aquests mètodes poden treballar amb mostres d'estrelles per les quals disposem de tota la informació en l'espai sis dimensional de posicions i velocitats, l'anomenat espai de les fases (mètode mGC3, introduït per Mateu et al. 2011); també per mostres d'estrelles per les que no disposem de la informació en velocitats radials (mètode nGC3, desenvolupat més recentent per aquests autors); o mostres d'estrelles per les que només disposem d'informació sobre la posició (mètode GC3, introduït per primera vegada per Johnston, Hernquist & Bolte 1996). A més, també hem introduït el mètodes anomenats LonKin, els quals analitzen bàsicament la tendència del moviment vertical mig de les estrelles en funció de la longitud galàctica.

En aquest treball hem desenvolupat expressions analítiques pel camp de forces d'un potencial tipus Miyamoto-Nagai de disc corbat. Començant per una model de potencial galàctic axisimètric de A&S, procedim a distorsionar el potencial d'acord amb dos models diferents de curvatura: 1) un model amb una línia de nodes recta i 2) un model amb una línia de nodes que presenta una torsió a mesura que augmenta el radi galactocèntric. Considerem inicialment un conjunt de partícules prova que relaxem en un potencial de A&S. A continuació anem corbant el potencial del disc adiabàticament, fent que les partícules segueixin lligades al potencial i no quedin pas enrere. In alguns casos s'introdueix adiabàticament una torsió a partir d'una transformació purament geomètrica de les coordinades de les partícules en l'espai de les fases. La distribució cinemàtica de les nostres mostres sintètiques es construeix de manera que puguin ser associades a tres poblacions traçadores diferents: estrelles OB i A de la seqüència principal i estrelles gegants de l'anomenat Red Clump (RC).

El mètode mGC3 assumeix que les estrelles en un cert radi galactocèntric estan confinades en una banda de cercle màxim, amb la seva posició galactocèntrica i el vector velocitat perpendiculars al vector normal al pla, el que defineix en particular aquest cercle màxim. Identifiquem el pic de la distribució en el que anomenem el mapa polar de recomptes estel·lars, és a dir el mapa que mostra el nombre d'estrelles associades a cada gran cercle, mitjançant un ajust bayesià. Aquest ajust ens proporciona la identificació del angle d'inclinació de l'anell i l'angle de torsió així com els seus corresponents intervals de confiança.

Hem generat diversos catàlegs simulats realistes d'estrelles OB, A i del RC utilitzant la informació proporcionada pel model de Galàxia de Besançon i considerant el model d'extinció interestel·lar 3D de Drimmel et al. (2003). Hem aplicat a aquest catàleg els models d'error en els paràmetres astromètric i fotomètrics que creiem presentaran les dades de Gaia així com les seves limitacions observacionals (magnitud límit). Aquests catàlegs ens han permès provar els

mètodes estadístics desenvolupats, analitzant el rang d'aplicabilitat i identificant les principals limitacions. Observem que la introducció de la informació cinemàtica en els mètodes (mGC3 i nGC3) millora significativament la recuperació de l'angle d'inclinació de la curvatura, angle que aconseguim recuperar amb una discrepància inferior a $\sim 0.75^\circ$ per la majoria dels casos. Observem com, utilitzant només la informació posicional (mètode GC3), recuperem una inclinació sempre i sistemàticament sobreestimada en un factor $\sim 2^\circ$. Encara que aparentment petit, per distàncies galactocèntriques $r \lesssim 12$ kpc, on l'angle d'inclinació és petit, aquest factor representa un error superior al 100%. Hem pogut identificar i quantificar els biaixos en els resultats obtinguts. Aquests són de dos tipus: els que deriven del pas de la paral·laxi a la distància com els deguts a un tall en magnitud aparent.

Hem demostrat que les estrelles OB i les estrelles del RC són bons traçadors de la curvatura del disc galàctic. Les estrelles A només poden ser utilitzades per determinar les característiques del la curvatura d radis galactocèntrics inferiors a ~ 12 kpc, principalment debut a la seva més feble brillantor intrínseca. Utilitzant dades amb bona qualitat astromètrica (error relatiu en paral·laxi inferior o igual al 20%), hem aconseguit recuperar amb una precisió remarcable l'angle d'inclinació de la curvatura amb els tres traçadors disponibles, sempre que tenim un bon nombre d'estrelles en el radi corresponent. En aquest treball proposem un criteri empíric per a identificar quina és la distància límit a la qual els resultats obtinguts a partir dels mètodes nGC3 i mGC3 comencen a presentar uns resultats esbiaixats. Això s'ha fet per a la mostra d'estrelles que tenen error relatiu en la distància inferior al 20%. D'acord amb aquests resultats, veiem que hauríem de descartar de l'anàlisi els radis galactocèntrics pels quals el nombre d'estrelles ha reduït en un factor inferior al $\lesssim 10\%$ respecte del nombre d'estrelles del radi més proper ($9 < r_{obs} < 10$ kpc). Observem com podem recuperar be els paràmetres de la mostra d'estrelles OB amb bons paràmetres astromètrics a la que hem imposat una inclinació i una torsió al potencial donada. Els valors es recuperen amb un error inferior $< 3^\circ$ per a totes les distàncies. És important esmentar que en tots els treballs amb els mètodes GC3 sempre hem utilitzat les paral·laxis trigonomètriques (mai les distàncies). Hem de tenir en compte que per d'altres traçadors cinemàtics com ara les estrelles Cefeides o les RR Lyrae podrem disposar de bones paral·laxis fotomètriques per a portar a terme aquest anàlisi. També, per estrelles més febles, podrem disposar en un futur de paral·laxis fotomètriques amb l'error suficient per emprendre aquest estudi ($\Delta\varpi/\varpi > 20\%$). Comparant les diferents variants dels mètodes proposats aquí podem veure clarament les avantatges d'utilitzar la informació cinemàtica que ens aportarà Gaia.

En aquesta primera part del treball hem desenvolupat un primer i simplificat model cinemàtic per analitzar la curvatura i possible torsió del disc de la nostra galàxia. La simplicitat del model ens ha permès avaluar l'eficiència i la limitació del us de les dades de Gaia per a caracteritzar aquesta estructura a les parts externes del nostre disc galàctic. Hem explorat i quantificat les limitacions del mètode. A partir d'aquest treball esperem que la base de dades de Gaia, junt amb els mètodes desenvolupats aquí, conformin una bona combinació per a caracteritzar la curvatura del disc galàctic de la Via Làctia.

En la segona part del treball hem utilitzat el mètode LonKin per a analitzar la traça cinemàtica de la curvatura del disc galàctic en l'espai dels observables de Gaia. Hem comprovat que aquesta traça és molt més significativa quan s'analitza el comportament del moviment propi en latitud galàctica, és a dir la component vertical al pla. Aplicant aquest mètode a la nostra mostra simulada d'estrelles gegants K del Red Clump (RC), observem que el màxim del valor mig del moviment propi en latitud galàctica s'obté en la direcció de l'anticentre galàctic, un màxim que creix a mesura que augmentem el radi galactocèntric de les estrelles de la mostra. El següent pas ha estat buscar aquesta traça cinemàtica en els catàlegs de moviments propis actualment disponibles. Per fer-ho, hem plantejat una estratègia que ens ha permès utilitzar les dades fotomètriques de 2MASS per seleccionar les estrelles de Red Clump del catàleg UCAC4 (Zacharias et al. 2013). Sorprenentment, l'aplicació del mètode LonKin a aquestes dades mostra un mínim en la direcció de l'anticentre, un comportament completament oposat a l'esperat. Molt probablement això es deu als importants errors sistemàtics que presenten aquests catàlegs, sobretot a la velocitat angular residual del sistema de referència del catàleg respecte al sistema de referencia inercial, obtingut a partir de quàsars y objectes extragalàctics. És important mencionar aquí que la traça cinemàtica que presenta la curvatura del disc galàctic en el nostre model cinemàtic és de l'ordre de ~ 1 mas yr^{-1}, mentre que alguns dels resultats publicats recentment per a aquesta discrepància entre les components de la velocitat angular del sistema de referència inercial i el del catàleg (Bobylev 2010; Fedorov et al. 2011) són aproximadament del mateix ordre. Hem aplicat un ajust de mínims quadrats a les nostres dades amb l'objectiu d'estimar quines correccions a les components de la velocitat angular de rotació del sistema respecte a l'inercial hauríem d'aplicar per tal que les dades observacionals s'ajustessin als resultats obtinguts pel model. És important mencionar aquí que estem prenent la hipòtesi que el nostre model reflecteix el comportament de la curvatura del disc galàctic de la Via Làctia, hipòtesi que, com s'ha discutit anteriorment, pot no ser certa. Els resultats obtinguts per a la correcció de la component de la velocitat residual en la direcció de rotació galàctica, ω_{2g}, presenta un acord raonable amb els valors recentment publicats(Bobylev 2010; Fedorov et al. 2011). Com que el catàleg UCAC4 és complet només fins a magnitud ~ 16, el nombre de quàsars que conté és d'uns pocs centenars. A causa de la seva distància, és raonable suposar que aquests objectes tenen un moviment propi nul. Considerant aquesta hipòtesi, i tenint en compte el baix nombre d'objectes disponibles, hem realitzat un nou ajust per mínims quadrats per a aquests objectes del catàleg UCAC4 que ens ha permès una nova estimació de les components de la velocitat residual del sistema de referència. Com era d'esperar, els resultats obtinguts presenten errors grans, sent els valors obtinguts per a aquestes components sempre compatibles amb zero al nivell de 2-sigma. Com a primera conclusió, aquest estudi ens mostra molt clarament la necessitat de conèixer amb bona precisió la rotació residual del sistema de referència respecte al sistema inercial, així com qualsevol altre efecte sistemàtic en els moviments propis, abans de procedir a la determinació precisa de la traça cinemàtica deguda a la presència de la curvatura del disc galàctic. Gaia, sens dubte, ens ofereix aquesta oportunitat. S'espera aconseguir la inercialització del sistema de referència de Gaia, amb les dades finals de la missió, amb una precisió de l'ordre de 0.4μas yr^{-1},

una qualitat mil cops superior a la disponible en aquests moments.

Per acabar, en l'últim capítol de la tesi, hem abordat un estudi similar a l'anterior utilitzant el catàleg de moviments propis PPMXL (Roeser et al. 2010). Hem seguit una estratègia semblant per a la selecció de les estrelles de Red Clump d'aquest catàleg y la determinació de les seves distàncies a partir de la fotometria infraroja. A diferència del cas anterior, hem estudiat el comportament mig de les velocitats verticals (components W de la velocitat) amb l'azimut galàctic. Aquest catàleg presenta l'avantatge de tenir una magnitud límit de V$\sim$ 20, per la qual cosa conté centenars de milers de quàsars. Això ens ha permès derivar els possibles efectes sistemàtics (zonals) en els moviments propis a partir d'aquests objectes. Aplicar aquesta correcció a cada zona del cel ha permès reduir significativament aquests efectes sistemàtics. Com a novetat, hem ajustat a les estrelles del Red Clump un model analític simple capaç de reproduir el desplaçament vertical degut a la curvatura del disc galàctic. Creiem que hem estimat el desplaçament d'oscil·lació vertical degut a la curvatura amb un nivell de detecció de 2σ, un desplaçament que tendeix a disminuir l'amplitud actual de la curvatura del disc galàctic. Com que aquesta oscil·lació només s'observa en la curvatura sud, interpretem els resultats considerant que la traça principal en forma de S de la curvatura és una estructura estable, amb un temps llarg de resposta, mentre que la irregularitat en la part sud és probablement deguda a un procés transitori. Aquesta feina ha estat desenvolupada per Martin López-Corredoira i Francisco Garzón de l'IAC. La meva contribució a aquesta feina ha estat l'anàlisi de la traça vertical de la curvatura en el context del model cinemàtic proposat en aquesta tesi. Hem realitzat diferents simulacions de partícules test considerant diverses estratègies per a l'evolució i creixement de la curvatura del disc – diferent nivells de transitorietat- i diferents paràmetres per a la seva geometria. En alguns casos, el potencial del disc ha sigut curvat en un règim impulsiu, és a dir, amb una variació ràpida en el temps, mentre que en d'altres, la curvatura creix adiabàticament. També s'ha considerat casos més complexos en els quals primer el sistema té un creixement adiabàtic i després l'amplitud creix impulsivament. L'últim dels casos considerat pretén ajustar millor les dades obtingudes. Els nostres resultats mostren que un decreixement impulsiu de l'amplitud de la curvatura reprodueix qualitativament la traça en la velocitat vertical que mostren les dades del catàleg PPMXL. Un canvi impulsiu de potencial del disc galàctic amb el temps indicaria que les estrelles poden no estar en equilibri estadístic amb el potencial corbat del disc i, per tant, aquesta traça observada en la part sud de la curvatura podria desaparèixer en pocs períodes orbitals.

Actualment estem desenvolupant i analitzant altres casos més complexos en els quals la curvatura perd la seva simetria nord-sud. Anomenem a aquests models lopsided models. El camp de força corresponent a aquest cas ja ha estat calculat i aplicat a les primeres mostres de partícules test. Amb aquest model lopsided no esperem trobar un únic pic ben definit en la família de mapes polars del mètode GC3. Al contrari, depenent dels paràmetres geomètrics imposats a aquest model lopsided, esperem trobar diverses formes que requeriran un estudi i interpretació molt més complexes.

També ens proposem en un futur, dissenyar, desenvolupar i ajustar un model per a l'eixamplament del disc galàctic (flare en anglès). Estudiarem com la incorporació d'aquesta variació en l'estructura radial del disc afecta a la traça cinemàtica de la curvatura galàctica així com a la recuperació dels seus paràmetres geomètrics mitjançant l'ús de la família de mètodes GC3.

En relació a la feina realitzada amb el catàleg UCAC4, el següent pas serà aplicar la família de mètodes GC3 a les seves estrelles de RC i comparar els resultats obtinguts abans i després de corregir els moviments propis de la velocitat residual del sistema de referència. Així mateix, aplicarem aquests mètodes a les estrelles que seran seleccionades utilitzant dades fotomètriques addicionals del catàleg IPHAS.

Abstract

We explore the possibility of detecting and characterising the warp of the stellar disc of our Galaxy using synthetic Gaia data and two available proper motion catalogues namely UCAC4 and PPMXL. We develop a new kinematic model for the galactic warp. With Gaia, the availability of proper motions and, for the brightest stars radial velocities, adds a new dimension to this study. A family of Great Circle Cell Counts (GC3) methods is used. They are ideally suited to find the tilt and twist of a collection of rings, which allow us to detect and measure the warp parameters. To test them, we use random realisations of test particles which evolve in a realistic Galactic potential warped adiabatically to various final configurations. In some cases a twist is introduced additionally. The Gaia selection function, its errors model and a realistic 3D extinction map are applied to mimic three tracer populations: OB, A and Red Clump stars. We show how the use of kinematics improves the accuracy in the recovery of the warp parameters. The OB stars are demonstrated to be the best tracers determining the tilt angle with accuracy better than ~ 0.5 up to galactocentric distance of ~ 16 kpc. Using data with good astrometric quality, the same accuracy is obtained for A type stars up to ~ 13 kpc and for Red Clump up to the expected stellar cut-off. Using OB stars the twist angle is recovered to within $< 3^\circ$ for all distances. In this work we have developed a first and simplified kinematic model for our Galactic warp. The simplicity of the model has allowed us to evaluate the efficacy and limitations of the use of Gaia data to characterise the warp. These limitations have been fully explored and quantified. From the work done so far, we expect that the Gaia database, together with the methods presented here, will be a very powerful combination to characterise the warp of the stellar disc of our Galaxy. Moreover, We introduce LonKin methods that help us detect the kinematic signature of the warp in the vertical motions of stars as a function of galactic longitude. Applying this method to the UCAC4 proper motions, we do not obtain a similar trend as the one we expect from our warp model. We explore a possible source of this discrepancy in terms of systematics caused by a residual spin of the reference frame with respect to the extra-galactic inertial one. We also look into a deeper proper motion survey namely the PPMXL. The effect of systematics in this catalogue was reduced using hundreds of thousand quasars present in this survey. An analytical fit to the vertical velocity trend of red clump stars suggests a vertical oscillation in the southern warp with a rather high frequency that tends to decrease the amplitude of the warp. We analysed this trend in the context of our warp model and an abrupt decrease of the warp's amplitude in a very short time of about one hundred Myr

could explain this trend.

The author is supported by the Gaia Research for European Astronomy Training (GREAT-ITN) network funding from the European Union Seventh Framework Programme, under grant agreement n°264895. This thesis has carried out at the Department d'Astronomia i Meteorologia (Universidad de Barcelona) and at the Instituto de Astronomía (Universidad Nacional Autónoma de México). This work was also supported by the MINECO (Spanish Ministry of Science and Economy) - FEDER through grants AYA2012-39551-C02-01 and ESP2013-48318-C2-1-R. Simulations were carried out using Atai, a high performance cluster, at IA-UNAM and bonaigua at DAM/UB.

Contents

Part I

INTRODUCTION

1

General introduction

1.1 Background

In 1610, Galileo performed the first telescope observations of the sky and discovered that the stream of diffuse white light seen in a summer night, actually consists of a large number of faint stars. In the mid-eighteen century, Immanuel Kant suggested that the Solar system is bound with the gravitational force of the Sun and the rotation of the planets around it, prevent them from collapsing. He also concluded that the Milky Way should have the same arrangement as the Solar system. Kant believed that some of the nebulae, which are faint, diffused patches of light seen in the night sky, might be separate galaxies themselves, similar to the Milky Way. Kant referred to both the Milky Way and the extragalactic nebulae as "island universes". In 1785, William Herschel made some telescope observations with which he could glimpse the Milky Way's structure. Using the observations from both, northern and southern hemispheres, he counted the number of stars that lie within different apparent brightness bins in different regions of the sky. He derived distances to these stars assuming they all share the same intrinsic brightness. In this way, he could obtain the distribution of stars in the Milky Way. In this map, the distribution was flattened with the Sun placed close to the centre of it.

At the beginning of the 20th century, using photographic plates, Jacobus Kapteyn could gather a lot of information on stars' brightness and their small displacements in the sky (today, known as *proper motions*) from year to year. Moreover, using the spectra of stars he could measure the line-of-sight velocity. All of these data, led him to deduce an oblate spheroidal distribution for the Milky Way. Also, he found that, similar to the Herschel's work, the Sun is

located close to the centre of the Galaxy. The missing point in both of these two works, was that the light absorbing effect of the interstellar dust was not taken into account. Therefore, the distance of stars was overestimated and as a result, the Sun appeared to be located close to the centre of the Galaxy.

Studying the distribution of globular clusters, Harlow Shapley, around 1915, expected to observe a uniform distribution throughout the sky as a function of what we now call *galactic longitude* (Shapley 1917, and following papers). To his surprise, Shapley found the number of globular clusters had a maximum towards the direction of the constellation Sagittarius. He argued that this point must indicate the location of the centre of the Galaxy. The globular clusters contain Cepheid stars, a type of variable pulsating star whose period-luminosity relation can be used to determine the distances to globular clusters. He calculated the distance from the Sun to the centre of the Galaxy to be about 15 kpc which is very different from the Kapteyn's Universe. At present, we know that the Sun is placed at about 8.5 kpc from the Galactic centre (Bovy et al. 2012). Again, the unknown effect of the interstellar dust falsified the distance estimate of Shapley. He also argued that the spiral nebulae are not island universes and they belong to the Milky Way (Shapley & Shapley 1919). On the other hand, Heber Curtis had observed quite a few novae (bright stellar sources that appear for a short while before fading away) within the Great Andromeda Nebula (M31). Curtis noticed that these novae were, on average very much fainter than those seen within the Milky Way, which implies that they are located much further away. He became a supporter of the island universes hypothesis, which held that the spiral nebulae were actually independent galaxies. This disagreement between Shapley and Curtis led to the "Great debate" in 1920 (Shapley & Curtis 1921). A few years later, Edwin Hubble using the observations from the 100" Hooker telescope at Mount Wilson, managed to resolve this problem. He could measure the distance to the Andromeda nebula using the Cepheids in this nebula, to be around 300 kpc (Binney & Merrifield 1998). This measured distance was far too large to be a part of Milky Way. Therefore, he could confirm that Milky Way is one of the many galaxies in the observable universe and the spiral nebulae are actually *spiral galaxies*.

Bertil Lindblad made a more detailed theoretical model for the Milky Way. Studying the globular clusters, he concluded that the mass of the proposed model for Milky Way by Shapley was closer to the truth than the one of Kapteyn. Since it would provide stronger gravitational forces which was needed to bind the globular clusters to the Milky Way. He also proposed that the Milky Way was symmetric about the central axis of the system and stars were rotating about this axis (Lindblad 1927). The first person to publish a study modelling the distribution of mass in the Solar neighbourhood was Jaan Oort (Oort 1932). This was a local study, nevertheless its importance lays in that it was the first quantitative dynamical estimation. Using the kinematics in the Solar neighbourhood, he showed that the stars must be following almost circular orbits in a disc with differential rotation.

The discovery of the radio emission of gas in the Milky Way (Jansky 1933) helped astronomers

to get a better picture of Milky Way and its large-scale structures. This is mainly due to the fact that the Hydrogen line at 21 cm emitted by Hydrogen is unaffected by interstellar extinction (Binney & Merrifield 1998). Studying its Doppler shift, the line-of-sight velocities could easily be obtained. Maartin Schmidt, a Dutch student of Oort, developed in his thesis a quantitative mass model for the entire Galaxy based in a series of oblate spheroids (Schmidt 1956). This merits to be mentioned as it was the first global mass model of our Galaxy. This model, however, produces a decaying rotation curve at the Sun's position. At that time it was not known that our Galaxy has a flat rotation curve. This is because, for geometrical reasons, the radio data can be converted into a rotation curve, only for points inside the solar orbit. From 21 cm observations, the astronomers realised that the Galactic disc is not simply an axisymmetric structure and some non-axisymmetric components are present. The disc is not completely flat, but at large radii, it twists upward at one side and downward at the opposite side which is called a *warp*. There are some spiral shaped regions in the gas density maps where the density is greatly enhanced (Oort et al. 1958) known as *spiral arms*. Towards the centre of the Galaxy, the line-of-sight velocities showed a non-circular motion that should be induced by a strong non-axisymmetric potential which is known as the *Galactic bar* (Peters 1975).

Nowadays, the great advances in technology, provides astronomers with better and bigger observational instruments that cover ever larger swaths of the electromagnetic spectrum. Using infrared images and radio-telescope surveys of the interstellar gas, the main features of the Milky Way are better understood. In Fig. we present HI layers of the Milky Way disc. The colour contours show the disc being warped up and the grey contours represent it being warped down.

What interests us the most in this thesis, are the astrometric surveys which are devoted to precise measurements of positions, parallaxes and proper motions. These measurements help us understand the motion of each star in its orbit around the centre of the Galaxy. The advent of *Hipparcos* satellite, launched at 1989, provided us with high precision astrometric data in the Solar neighbourhood. The accurate measurements of parallaxes and proper motions of stars, allowed a determination of their distance and tangential velocity. The resulting Hipparcos Catalogue, a high-precision catalogue of 118,218 stars, was published in 1997. However, although tantalising, the results from Hipparcos were constrained to the solar neighbourhood only and furthermore, the sampling depth varies enormously across the sky, which made the statistical modelling a very complicated task.

These drawbacks gave form to the next astrometric space mission: *Gaia* . In December 2013, the Gaia spacecraft was launched with the goal of performing micro-arcsecond astrometry for approximately 1 billion stars (approximately 1% of the Milky Way population). Stars will be observed distributed all across the Galaxy, complete up to Gaia magnitude passband brighter than 20, which provides a comprehensive and uniformly sampled probe of the stellar component of our Galaxy. In Fig. 1.1, we present the expected distribution of the stars observed by Gaia from the Milky Way as seen face-on (top panel) and edge-on (bottom panel). This cornerstone astrometric space mission of ESA, will monitor each of its target stars about 70 times over

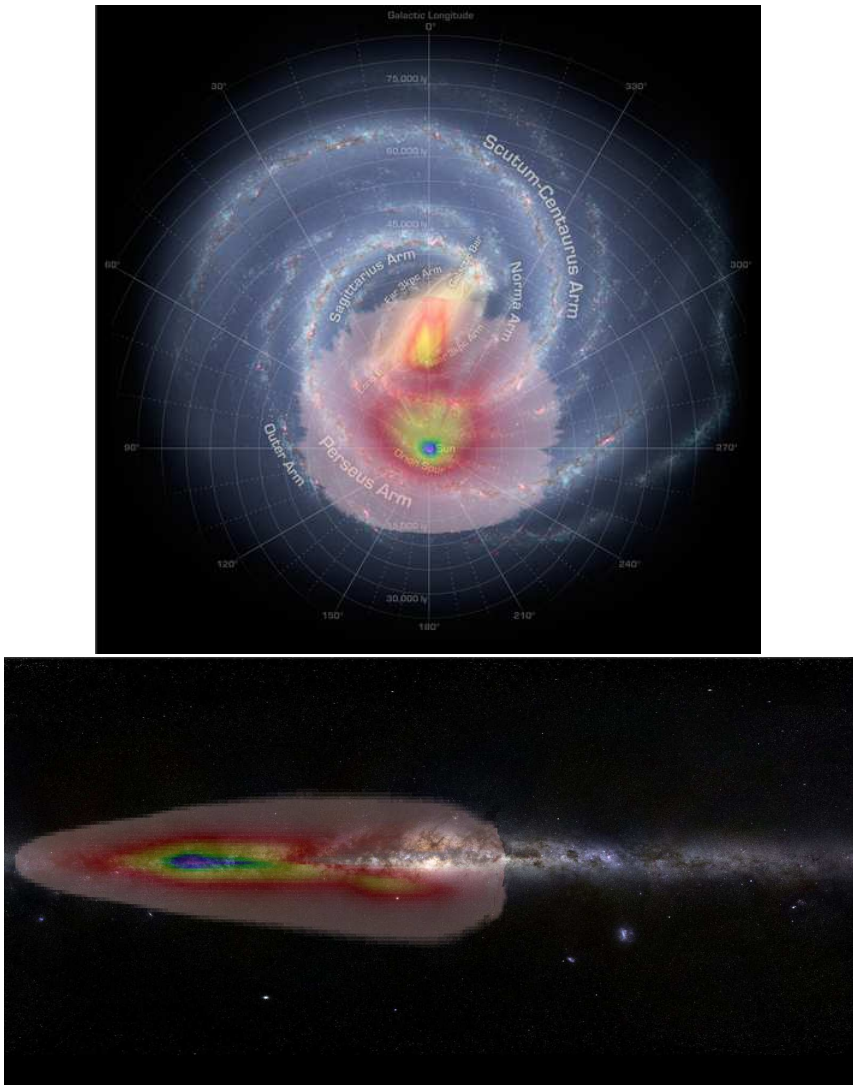

Figure 1.1: The expected 2D distribution of the contents of the Gaia catalogue in the Milky Way as seen face-on (top panel) and edge-on (bottom panel). The distribution was plotted on top of an artistic top view of our Galaxy. The colours of the overlaid distribution show the expected density of the stars observed by Gaia in different regions of the Galaxy, ranging from purple-blue for very high densities, to pink for low densities. The image was produce using the simulated Gaia catalogue (GUMS v8) based on the Besançon Galaxy Model (Robin et al. 2003) produced by the DPAC-CU2. Credits: X. Luri & the DPAC-CU2.

the period of its five-year operation. Gaia's data comprises absolute astrometry, broad-band photometry, and low-resolution spectro-photometry. This accurate knowledge of velocities and three-dimensional positions gives a new insight into the structure and dynamics of Milky Way.

1.2 This thesis

As mentioned in the previous section, the disc of our Galaxy is not flat, but becomes warped as we move to the outermost galactocentric radii. The advent of Gaia which will provide us with accurate astrometry from space, opens up a new opportunity on improving our knowledge of the stellar component of the galactic warp. On of the aims of this thesis is to estimate the Gaia capabilities in detecting and characterising the structure and dynamics of the galactic warp, not only using stellar positions but also considering their velocities.

In order to characterize the galactic warp in the stellar component of the disc using high precision Gaia astrometric information, new numerical tools to extract the relevant information are needed and they need to be calibrated, so when applied, we can assign meaning to their results. For this we need tools and a synthetic database in which apply them. Ideally, the synthetic database should be a random realization of a positional and kinematical model of the warp which is "observed" applying the Gaia selection function, together with its expected observational errors and the application of a suitable model for extinction. This "mock Gaia catalogue" will thus provide us with a map from a model of which we know all parameters, to the expected Gaia observations. We can then use this map to calibrate our tools. We aim to analyse at what significant level Gaia can measure the warp in different stellar populations. This requires the use of an efficient and robust method that help us accurately measure the geometrical properties of the warp, even after considering the Gaia errors. We use the family of GC3 methods as introduced by Mateu et al. (2011) which is ideally suited to measure the tilt and twist of a warped disc. moreover, we introduce a LonKin methods where we look for the kinematic signature of the warp in the vertical motions of disc stars.

In this work, we do not develop a fully self-consistent simulation of a warp, but rather a first simplified kinematic model for our Milky Way warp. This is because it is not our goal to dwell into dynamical scenarios, but rather have a reasonable toy model with which to asses the real possibilities of Gaia in detecting and characterising the warp. Using a set of test particles who are initially distributed in a disc under a Galactic potential model, we perform a numerical integration to calculate the path of stars while gradually warping the disc potential. Adopting different photometric and kinematic properties, we can generate various stellar populations.

We also devote a part of this work to study the kinematic signature of the Milky Way warp using the available proper motion catalogues such as UCAC4 (Zacharias et al. 2013) and PPMXL (Roeser et al. 2010). Using different methods, we try to minimise the effect of systematic errors in the proper motions. Selecting red clump stars from these catalogues, we look at the trend of

their vertical motions.

1.3 Introductory definitions

We need several frames of reference to describe the positional and kinematical information of the Galaxy features and stellar trace population that we will be using. Throughout this thesis, we use a Galactcocentric Cartesian coordinate whose X-axis goes along the Sun-Galactic centre direction; the Y-axis perpendicular to it, positive in counter-clockwise direction as seen from the North Galactic Pole; and the Z-axis perpendicular to the flat Galactic plane.

We use (U, V, W) velocity components in this thesis. These are heliocentric velocity components that are measured with respect to a inertial Cartesian frame of reference that is centered at the Sun position at ($x_\odot = -8.5$, $y_\odot = 0$, $z_\odot = 0$) kpc. This frame , at present, does not rotate with the Galaxy. U is the radial velocity component, which is positive towards the GC; V is the azimuthal component, positive in the direction of Galactic rotation; and W is the component perpendicular to the plane, positive towards the North Galactic Pole.

With our warp simulation, we calculate (v_x, v_y, v_z) which are Galactocentric velocity components measured in an inertial, cartesian frame, anchored at the galactic center, and whose axes coincide at present, with the heliocentric frame. For moving from this frame of reference to the heliocentric one, we should remove the effect of Galactocetric velocity of the Local Standard of Rest (LSR) and the motion of the sun with respect to the LSR. The LSR is defined at the position of the Sun, as the velocity vector of the local circular orbit assuming an azimuthally averaged mass distribution for the Galaxy. The relation between the Galactocentric frame of reference and the heliocentric one is illustrated in the figure 1.2. In this figure the definition of the vectors are as follows:

- $\overrightarrow{V}_g$ is the Galactocentric velocity of the star or (v_x, v_y, v_z),
- $\overrightarrow{V}_h$ is the heliocentric velocity of the star or (U, V, W),
- $\overrightarrow{V}_{LSR}$ is the Galactocentric velocity of LSR which is $(0, \Theta_\odot, 0)$,
- $\overrightarrow{v}_\odot$ is the peculiar velocity of the Sun with respect to the LSR.

As seen in this figure, the relation between Galactocentric velocity of the star, $\overrightarrow{V}_g$, and the heliocentric velocity of the star, $\overrightarrow{V}_h$, is:

$$\overrightarrow{V}_h = \overrightarrow{V}_g - \overrightarrow{V}_{LSR} - \overrightarrow{v}_\odot \tag{1.1}$$

If we write the above equation for different components, we get:

$$U = v_x - u_\odot \tag{1.2}$$

$$V = v_y - \Theta_\odot - v_\odot \tag{1.3}$$

$$W = v_z - w_\odot \tag{1.4}$$

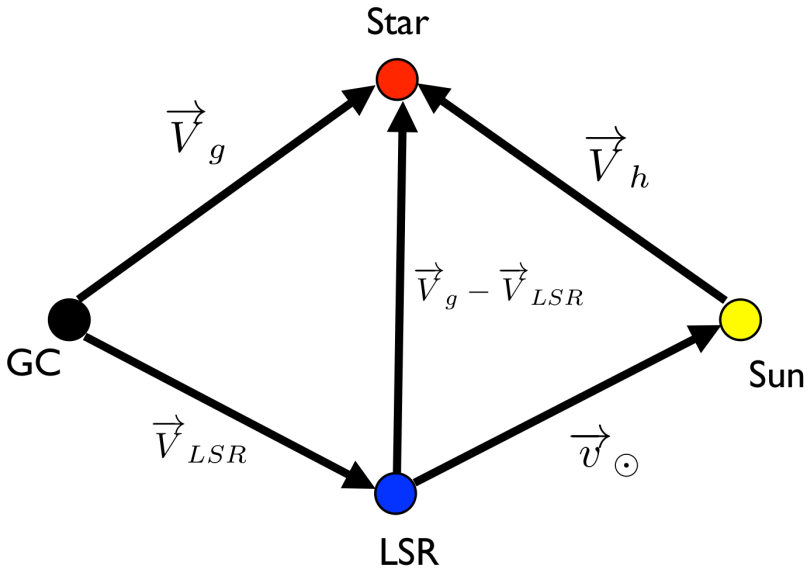

Figure 1.2: The relation between the Galactocentric frame of reference and the heliocentric one. $\overrightarrow{V}_g$ is the Galactocentric velocity of the star, $\overrightarrow{V}_h$ is the heliocentric velocity of the star, $\overrightarrow{V}_{LSR}$ is the Galactocentric velocity of LSR and $\overrightarrow{v}_\odot$ is the motion of the Sun with respect to the LSR.

2

The warp in the disc of the Milky Way and in other galaxies

2.1 Warps in galaxies

Disks of galaxies are mostly thin and flat, but moving to the outermost visible radii, they are often warped. In Fig. 2.1 we show an example of a galaxy with a prominent warp. Warps can have different shapes, usually a warped disk is twisted upward at one side and downward at the opposite side, in such a way that if looking at the galaxy edge-on, it resembles an integral sign. Therefore, these are commonly called "integral-sign-shaped" or "S-shaped" warps. There also exist "U-shaped" warps where both sides of the plane rise and "L-shaped" with only one-sided warp (Sánchez-Saavedra et al. 2003) (see Fig. 2.2).

It is widely accepted that warps of disc galaxies are a common phenomena (as common as spiral structure). From observational studies in external galaxies, two empirical sets of laws have been derived (Kuijken & Garcia-Ruiz 2001).

- Briggs's laws (Briggs 1990)

    1. Discs are generally flat inside the R_{25} radius, that is inside the solar Galactocentric radius in our Milky Way (MW), and the line of nodes is straight out to $R_{26.5}$ [1].
    2. Further out, the line of nodes advances in the direction of galactic rotation.

[1] R_x is the radius (projected in the sky) of the isophote that corresponds to x mag arcsec^{-2}.

Figure 2.1: An example of a spiral galaxy with a prominent warp. This edge-on view of ESO 510-G13 is taken by WFPC2 of Hubble Space Telescope. Image credits: NASA and Hubble Heritage Team (STScI/AURA).

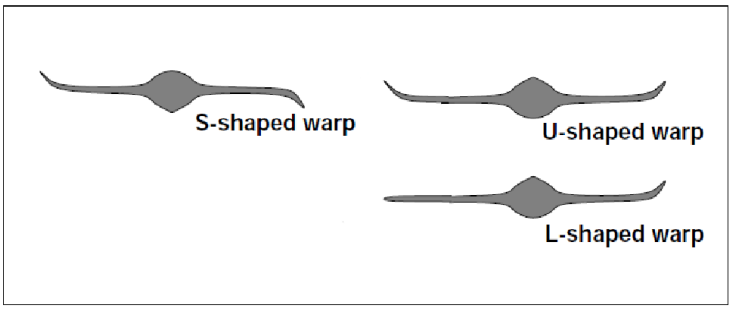

Figure 2.2: Different types of warps of the galactic disks as viewed edge-on (Sánchez-Saavedra et al. 2003).

The first law indicates that the self-gravity of the disc is important. In other words, the self gravity causes the different parts of the disc to precess as a rigid body and therefore the line of nodes stays straight (Kuijken & Garcia-Ruiz 2001). The second law implies that warps are not quite in equilibrium at large radii. This can be due to the differential rotation of the Galaxy wining over the self-gravity of the disc at large galactocentric radii, or the interaction between the disk and the environment at these radii (Kuijken & Garcia-Ruiz 2001).

- Bosma's laws (Bosma 1991)

  1. At least half of spiral galaxies are warped.
  2. It is less probable for galaxies with a small dark matter halo core radii to be warped. Note that the halo core radius was determined using the rotation curve decomposition.

  The first law suggests that warps are either, repeatedly regenerated, or a long-lived phenomenon. The first scenario needs a perturbing agent to warp the disc more or less continuously, while second needs a way of maintaining a coherent pattern against the destructive effects of differential precession (García-Ruiz et al. 2002). The second law could point a link between the warp of the disc and the halo potential (Kuijken & Garcia-Ruiz 2001).

As discussed by Cox et al. (1996), as the stellar warps usually follow the same warped surface as do the gaseous ones, there is strong evidence that warps are mainly a gravitational phenomenon. In any case, warped discs represent a theoretical challenge and, if properly understood, can be a valuable probe into the mass distribution in the outer disc and the halo in its vicinity (Binney 1992).

2.2 The Galactic warp as observed in optical, IR and radio

From the time when the first 21-cm hydrogen-line observations of our Galaxy became available, the large-scale warp in the HI gas disc became apparent (Burke 1957; Kerr et al. 1957; Westerhout 1957; Oort et al. 1958, among others). These independent studies showed that the maximum deviation of the plane exceeds 300 pc at a Galactocentric distance of 12 kpc. More than fifty years later, Levine et al. (2006) has re-examined the outer HI distribution proposing that the warp of gas is well described by three Fourier modes of azimuthal frequency 0, 1 and 2, all of which grow with the Galactocentric radius. The m=0 mode gives a vertical offset and m=1 produces an integral-sign-shaped warp, while the m=2 mode, or "saddle" mode, accounts for a large asymmetry between the northern ($l \sim 90°$) and southern warps ($l \sim 270°$). The amplitude of the 1 mode increases with radius over the entire range of radius from where the warp starts. The growth of 0 and 2 modes which are responsible for the warp asymmetry, begins where the stellar disc ends.

A more recent picture of the warp in the stellar component of our Galaxy is shown in Fig. 2.3, which shows the star counts obtained from Two Micron All Sky Survey (2MASS) near infrared data. The dashed line indicates the $b = 0°$ plane. We can clearly see that towards positive longitudes, the stars tend to warp up and towards negative longitudes, they warp down. Using this data, Reylé et al. (2009), found the northern warp of the stellar component, to be well modelled by an S-shaped warp with a significantly smaller slope than the one seen in the HI warp. While the southern warp can not be easily reproduced by any simple model. They also found that the slope of the warp in the dust has an intermediate value between the warp of the stellar and gas components. Moreover, they obtain the starting radius of the stellar warp to be at 8.4 kpc. López-Corredoira et al. (2002) also confirmed the existence of a warp in the MW's old stellar population whose slope follows the one of the gas. In this paper, using the 2MASS data, they estimate the maximum amplitude of the stellar warp as a function of Galactocentric radius, by fitting a power-law to the data. This is presented in Fig. 2.4 together with the the northern and southern warps in the gas obtained by Burton (1988). We will use this figure later to define our warp model.

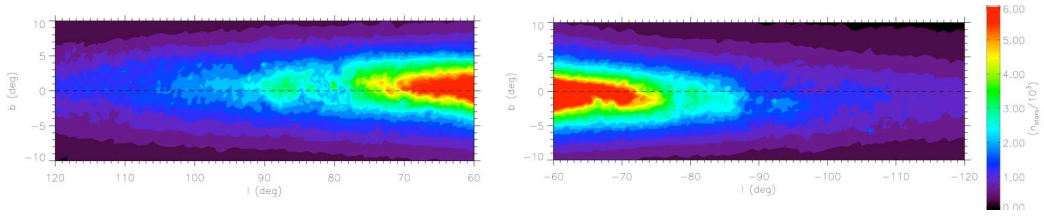

Figure 2.3: MW star counts using 2MASS data in Galactic longitude vs. latitude plane as presented in Reylé et al. (2009). The dashed line indicates the $b = 0°$ plane. Left panel shows the Northern warp, on the right, the Southern warp. Figure taken from Reylé et al. (2009).

Several authors have tried to estimate the phase angle of the line of nodes with respect to the Sun-Galactic centre line. Values range between $\sim -5°$ (López-Corredoira et al. 2002) and $\sim 15°$ (Momany et al. 2006). These morphological studies of the MW warp do not allow us, at present, to disentangle which are the mechanisms that are able to explain it.

2.3 Different scenarios for the origin of the Galactic warp

Many efforts have been directed toward understanding warps on a theoretical basis and, several mechanisms have been proposed for their existence (see the excellent reviews by Binney & Merrifield 1998; Sellwood 2013). In what follows we summarize some of the most widely proposed mechanisms.

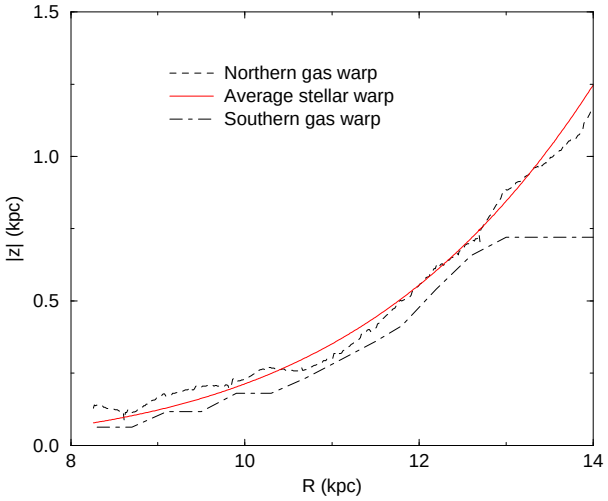

Figure 2.4: Maximum amplitude of the stellar warp (solid line) which is the best power-law fit to the 2MASS data in comparison with the one measured by Burton (1988) for the northern and southern warp gas (dashed and dot-dashed lines). Figure taken from López-Corredoira et al. (2002).

2.3.1 Bending modes

This mechanism posits that warps are free normal modes of oscillation of the galactic disc. Lynden-Bell (1965) suggested that warps could result from a persisting misalignment between the spin axis and the disc normal, a suggestion that was later elaborated by Hunter & Toomre (1969). Before the discovery of dark matter halos, Hunter & Toomre (1969) showed that the stability of bending modes depends on the shape of the density falloff near the edge of the disc. They found that the discrete bending modes do not exist in a cold, razor-thin disc, unless the surface density vanished abruptly at the edge of the disc (which is not the case for an exponential disc). These bending modes are considered to be a superposition of outgoing and ingoing waves, provided that the disc's outer edge can reflect outgoing waves, which can not be the case for a disc with a smoothly vanishing disc (Toomre 1983).

The distribution of matter in the halo would control the ability of the disc to sustain a long-lived bending wave. For a disc embedded in a rigid, axisymmetric, but flattened dark halo, and misaligned with the equator of the halo, the resulting torque from the halo together with the rotation of the disc, will cause it to precess about the halo's minor axis. Since in general, different parts of the disc have different precession frequencies, then without an important stabilizing action of the disc self-gravity, the warp would wind up and disappear. Sparke & Casertano (1988) showed that the bending modes are still possible when the self-gravity is taken

into account, and they are not sensitive to the details of the disc edge. However, it was found that a careful arrangement in the mass distribution (shape and density profile) is needed to obtain these long-lived modes, making this an unlikely scenario. On top of this, it turns out that the response of a non-rigid halo to the precession of a massive disc in its centre, which was not taken into account in the original mode calculations, invalidates this approach. Nelson & Tremaine (1995) explored the dynamical interaction between a warped disc and its surrounding halo. They found that in realistic circumstances the warp will be damped within one dynamical time of the disc. Dubinski & Kuijken (1995) also showed that the halo responds to an inclined processing disc within few local orbital periods and gets aligned to it. The conclusion is that warps can not be due to a misalignment between the disc and the inner halo. Binney & Merrifield (1998) confirmed the strong response of the halo to the precessing disc. They show that the halo response causes the line of nodes of a warped disc, that is started from the configuration of a normal mode, to wind up within a few dynamical times.

2.3.2 Misaligned infall

There is a likely misalignment between the late infalling material angular momentum axis and the disc spin axis in hierarchical galaxy formation scenarios. Jiang & Binney (1999) using an N-body simulation, showed that an integral-sign-shaped warp with a comparable amplitude to those observed can be generated when a live halo accretes material, whose angular-momentum vector is slightly inclined with respect to the initial symmetry axis of the disc embedded in it. While this work was done using a disc composed of rigid rings coupled by gravitation, Shen & Sellwood (2006) used a N-body simulation with a disc of particles with random motions and confirmed that warps can be induced by misaligned cosmic infall. Their simulations showed that the warp persists for a few Gyr, even when the external torque was removed. Furthermore, their simulated warped disc had a flat inner region following Briggs's law. All of these work, make this scenario to be a very plausible one.

López-Corredoira et al. (2002) showed that using a model of an intergalactic accretion flow which intersects a galactic disc can generate a warp in the disc. This torque should be produced by an intergalactic medium flow velocity of $\sim 100\ km/s$ with a mean baryon density of around $10^{-25}\ kg/m^3$. This low density flow is within the range of values compatible with observation.

2.3.3 Gravitational interaction with satellites

The tidal interaction between galaxies (forcing by satellites) has also been proposed to produce warps, especially the asymmetrical ones. García-Ruiz et al. (2002) using a simulation with N-body particle model for the halo plus tilted rings representing the disc, demonstrated that the tidal forces from the Large Magellanic Clouds (LMC) can not generate a warp with an amplitude or orientation as that presented by the warp in the Milky Way. In contrast, Weinberg & Blitz

(2006) used perturbation theory to demonstrate that a Magellanic Cloud (MC) as the origin for the MW warp can explain most quantitative features of the outer HI layer identified by Levine et al. (2006). In their model, the disc could feel both the direct tidal field from the MC and the force from the halo wake (self consistent response) excited by the MC. In Fig. 2.5, we can see the disc response to the tidal effect of the MC. They claimed the reason why the model of García-Ruiz et al. (2002) is not warp-producing, is that they have chosen an unlucky sets of parameters and they needed to investigate a variety of models. Bailin (2003) considering the mass and the orbit of the Sagittarius dwarf galaxy (Sgr), showed that it can be a possible origin of the MW warp. In Fig. 2.6 we show the schematic drawing of the orbits of the Sgr and the LMC as proposed by him.

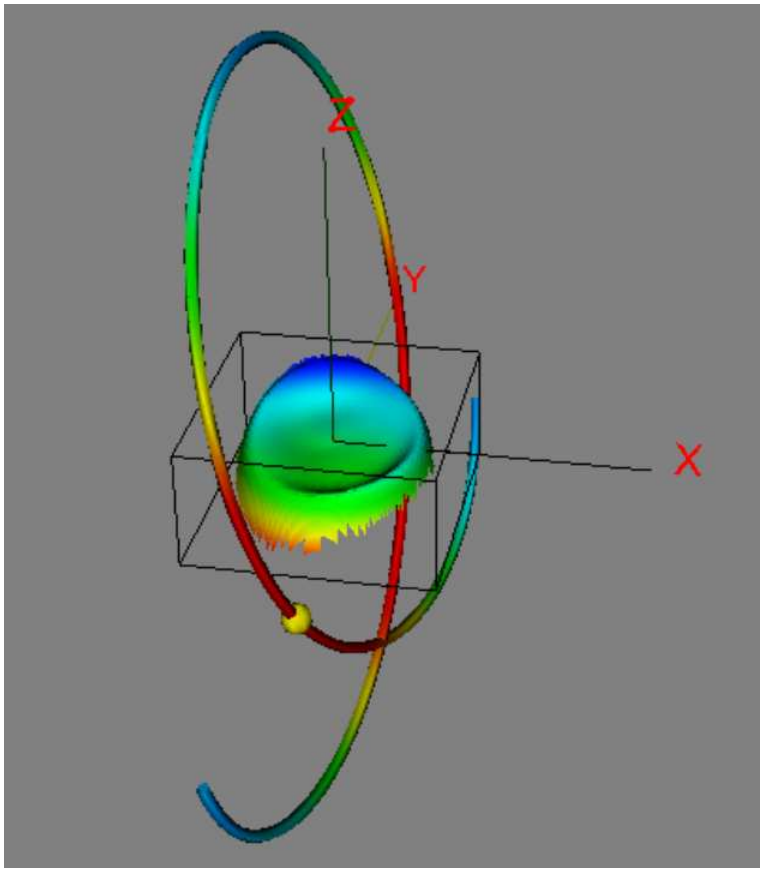

Figure 2.5: A warp excited by a MC passage modelled by Weinberg & Blitz (2006). The tube is the computed MC orbit, color coded to be blue at apocenter and red at pericenter. Note that in this snapshot, the MC is moving upwards. The yellow sphere is the position of the MC at the current time. The Sun is placed at $(-8.5, 0, 0)$ kpc. Figure taken from Weinberg & Blitz (2006).

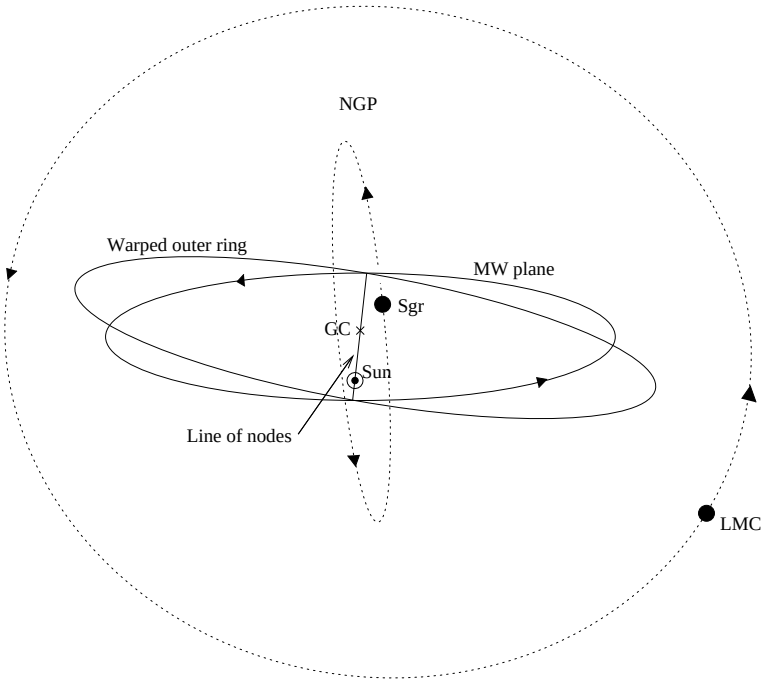

Figure 2.6: Schematic drawing of the orbits of the Sgr dwarf and the LMC as proposed by Bailin (2003). The plane of Sgr's orbit intersects the line of nodes of the warp and is orthogonal to the plane of the LMC's orbit. Not to scale. He suggested that the MW warp and the Sgr are coupled. Figure taken from Bailin (2003).

2.4 The kinematic signature of the warp

All previously mentioned modelling attempts did not use kinematical information about the warp, constraining themselves to fit the geometrical warp. It is clear that kinematics can also be fitted and will further constraint warp models. In this section we talk about modelling efforts that included this extra component.

The first kinematic warp analysis was inferred from Hipparcos proper motions of OB type stars (Drimmel et al. 2000). These authors concluded that the kinematics observed toward the Galactic anti-centre were inconsistent with the one expected for a long-lived warp. For a long-lived Galactic warp, they expected to observe positive vertical motions towards the anti-centre, but from the data they obtain a negative systematic vertical motion. They showed that this trend could be explained by a very high warp precession rate ($\sim$ -25 $\mathrm{km\,s^{-1}\,kpc^{-1}}$) and /or a very large photometric error ($\sim$ 1 magnitude). The later could cause the observed systematic vertical motions to be smaller than their true values. Later, Bobylev (2010), using the Tycho-2 kinematic data for red clump stars, he first corrected for the estimated residual rotation of the Hipparcos reference frame. Calculating the angular velocity of the observed rotation of the stellar system around the Sun-Galactic centre axis, he considered it as the kinematic signature of the Galactic warp in the solar neighbourhood. Previous to this work, Miyamoto & Zhu (1998) performed the same analysis using the proper motions of O-B5 stars from Hipparcos. They derived a similar systematic rotation with a positive angular velocity ($\Omega_W \sim +4$ $\mathrm{km\,s^{-1}\,kpc^{-1}}$), whereas the one obtained by Bobylev (2010) was negative ($\Omega_W \sim$ -4 $\mathrm{km\,s^{-1}\,kpc^{-1}}$). We suspect the reason for this discrepancy is the fact that Bobylev (2010) considered that the Hipparcos reference frame has a residual rotation with respect to the extragalatic inertial one and corrected for that. More recently, Bobylev (2013) using a sample of 200 classical Cepheids, obtained a value of $\Omega_W \sim$ -15 $\mathrm{km\,s^{-1}\,kpc^{-1}}$ which exceeds the value deriven from red clump stars by a factor of 4. However, he proposed that a study on larger sample of Cepheids with more accurate data is needed for confirming his results. Discrepant results obtained from all these works demonstrate the difficulty, at present, to disentangle the kinematic signature of the warp from other nearby and local perturbations.

At present, what is needed is better information that could help us to disentangle among the various competing scenarios. The warp of our own Galaxy is the one closest to us and thus, potentially a lot of detailed information may be gleaned from it. At the dawn of the Gaia era, a whole hitherto unexplored dimension opens up: adding good kinematical information of in situ stars partaking in the warp. This dimension must be explored: To what extent is it that Gaia data will be able to characterize the stellar disc warp and up to what distance? To answer this question, new detection and characterization tools must be devised and tested with Gaia mock catalogues and their limits identified.

Part II

Modeling the Galactic warp

Our test bench will be a series of test particles ensembles that represent random realizations of our various warped and twisted models of the galactic disc. Ideally, they should be built in a way that they have the imprint of the warp in their phase space coordinates. We can then convert these particle ensembles into sets of simulated stars by adding stellar parameters to them. The next step is to convert their properties into Gaia observables and apply the Gaia selection function, together with an error and extinction model, in order to produce Gaia mock catalogues that correspond to the warp models we started with.

Unfortunately, we do not have random realizations of particles that correspond directly to a warped model, so we have to build them ourselves. For this, we start with an axisymmetric galaxy mass model with a flat disc, and create a random realization of it. We then proceed to warp adiabatically the initially flat disc potential, while the test particles are integrated in this time-varying potential. Finally, we let the ensemble to relax for a few more dynamical timescales with the potential in its fixed, final configuration.

In the case of twisted warps, the warp is first applied as previously described, but then the twist is introduced as a direct geometrical transformation applied to the phase space coordinates.

In this part of the thesis we describe our warp model, the random realization of the initial flat disc and the way in which the warping is applied.

3

The warp model

3.1 Introduction

The aim of this chapter is to construct a kinematic model for the galactic warp. We want to generate an ensemble of particles in phase space that follows a warped model of the Galaxy's disc, we could do this with three different approaches: 1) an N-body simulation that results in a warped disc; 2) a test-particle simulation that follows a warped potential, or one that is warped gradually in time and finally; 3) a simple coordinate transformation of particle coordinates. The first approach would be a self-consistent dynamical warp while the second would not, however, it could be made to be in statistical equilibrium with the warped disc potential . The third approach is just a geometrical transformation where no self-consistency, nor statistical equilibrium is assured. An N-body simulation, although the best approach, is very expensive in terms of computational time, does not give you control on the final state of the system being simulated and necessarily needs to pick a particular origin scenario for the warp, something we do not aim to do yet. The second approach, while still realistic in the sense that the particle coordinates are set by the potential that is being warped through a real orbit integration, is not as simple (or presumably arbitrary) as the purely geometrical transformation of the third approach. In this thesis, we use the second approach to warp the galactic disk and the third approach for twisting the line of nodes.

For the second and third approaches described above, a first ingredient required to model a galactic disc warp is a transformation that can be applied to an initially flat potential function or particle phase space configuration, and distort it according to a specific warp model. In this

chapter we introduce three warp models: the untwisted warp model in which a warp with a straight line of nodes is introduced adiabatically to an initially flat potential, while the test particles are integrated in the time-varying potential; the twisted warp model, where the line of nodes of the final configuration from the previous model is twisted using a direct coordinate transformation; and the lopsided warp model, which is similar to the first model, except that the warp model is now lopsided. Note that for the cases with a straight line of nodes, the line of nodes is defined to coincide with the X-axis, which goes along the Sun-galactic centre direction.

We need to establish the mathematical transformation that allows us to introduce the warp into an initially flat potential and derive the resulting force field, or alternatively, to the position and velocity vectors of an ensemble of test particles. In the rest of this chapter we do this. In Sec. 3.2 we present our initial flat galactic potential, in Sec. 3.3 we show different approaches for defining a geometrical model for the warp. Sec. 3.4 describes our untwisted warp model and in Sec. 3.5 we present the warp model with a twisted line of nodes.

3.2 The axisymmetric potential model

We use an axisymmetric potential form as a basis for our warp model. The reason we do that, is because of simplicity. Introducing non-axisymmetries (e.g. bars or spiral arms) introduce a whole new level of mathematical complexity in the description and besides, we do not expect the disc non-axisymmetric components to play an important role on the warp, which appears at large galactocentric distances. Nevertheless, in Appendix B, we present simulations where we add a 3D spiral arm potential to confirm that this non-axisymmetric component does not significantly affect the warp signature.

We model the axisymmetric part of the MW's potential following Allen & Santillan (A&S) (Allen & Santillan 1991). This 3D potential model consists of a spherical bulge, a Miyamoto-Nagai disc (Miyamoto & Nagai 1975) and a massive spherical halo. The rotation curve of this potential model follows the one of the MW. The adopted observational constraints of the model are summarised in Table 3.1. The total axisymmetric mass is $M_T = 9 \times 10^{11}\,\mathrm{M}_\odot$. This is in good agreement with the recent observational value derived from Xue et al. (2008), who constrained the mass to be $M_T = 10^{+3}_{-2} \times 10^{11}\,\mathrm{M}_\odot$. The particular masses of the components of this model are presented in Table 3.2. This is a reasonable dynamical model that has the advantage of being completely analytical. Moreover, its mathematical simplicity makes it very suitable for numerical test particle computations.

3.3 Different approaches for the geometrical model for the warp

There are different approaches for defining a geometrical model for the warp. First we try a simple transformation that involves displacing points along the direction orthogonal to the disk.

Table 3.1: Adopted observational constrains in the A&S axisymmetric potential model (Allen & Santillan 1991).

Distance Sun-galactic centre	$R_\odot = 8.5$ kpc	
Local circular velocity	$V_c(R_\odot) = 220\ \mathrm{km\,s^{-1}}$	
Local total mass density	$\rho = 0.15\,\mathrm{M_\odot\,pc^{-3}}$	
Rotation curve	R(kpc)	$V_c(\mathrm{kms^{-1}})$
	0.43	259.8±10
	1.28	226.2±9.7
	2.55	201.5±9.7
	4.25	213.5±7.5
	6.38	224.0±7.8
	10.63	209.0±15
	15.94	223.0±20
	56.63	206.0±40

Table 3.2: Model constants in the A&S axisymmetric potential model (Allen & Santillan 1991).

Central mass	$M_1 = 1.4 \times 10^{10}\mathrm{M_\odot}$
Disc mass	$M_2 = 8.6 \times 10^{10}\mathrm{M_\odot}$
Halo mass	$M_3 = 8.0 \times 10^{11}\mathrm{M_\odot}$
Total mass	$M_T = 9.0 \times 10^{11}\mathrm{M_\odot}$

Although this is easily accomplished, we will show that this warping transformation introduces shape distortions. In particular, circular orbits are distorted into ellipses. Since this is not dynamically justified, a second approach to warp the disk is developed, in which we apply a tilt to rings. We will show that this second warping transformation does not distort shapes.

3.3.1 The first approach

First we define a mathematical mapping that allows us to "warp" either the potential, density functions, or particle positions, to generate a warp. This is accomplished by just shifting points vertically according to a warping function Δz_w that gives the vertical shift as a function of the r spherical coordinate on the disk. The dependence that we choose is a power law (r^α), such that $\Delta z_w(r_2) = \Delta z_2$.

We define the following parameters:

- r_1 is the spherical galactocentric radius where the warp begins.
- r_2 is the spherical galactocentric radius where the warp ends.
- Δz_2 is the height that the warp has achieved at r_2.
- α is a power law index that controls the shape of the warp.

The warp function is given by:

$$\Delta z_w(r\,;\, r_1, r_2, \Delta z_2, \alpha) = \begin{cases} 0, & r \leqslant r_1 \\ \Delta z_2 (\frac{r-r_1}{r_2-r_1})^\alpha, & r > r_1 \end{cases} \tag{3.1}$$

This function bends the z-axis upwards using a power-law. We use a power-law because this is the function López-Corredoira et al. (2002) used for fitting the 2MASS data to obtain the maximum amplitude of the warp as a function of galactocentric radius (see Fig. 2.4). Note that for the linear case where $\alpha = 1$, the r-derivative of the function is discontinuous at r_1. All other α values produce continuous slopes. In order to illustrate this, in Fig. 3.2 we plot this warp function for different values of α. We can see that by increasing α, the warping is done in a more smooth manner.

We now introduce an azimuthal dependence to produce a continuous warp of a disk. For this, we use a simple cosine function whose argument is the galactocentric azimuthal coordinate ϕ displaced from the origin by an amount ϕ_0 which corresponds to the direction of the maximum height of the warp:

$$\Delta z_w(r, \phi\,;\, r_1, r_2, \Delta z_2, \alpha, \phi_0) = \Delta z_w(r\,;\, r_1, r_2, \Delta z_2, \alpha) \times \cos(\phi - \phi_0) \tag{3.2}$$

In Fig. 3.1, we show an example for the case: $r_1 = 1/4$, $r_2 = 2$, $z_2 = 1$ and $\alpha = 3$.

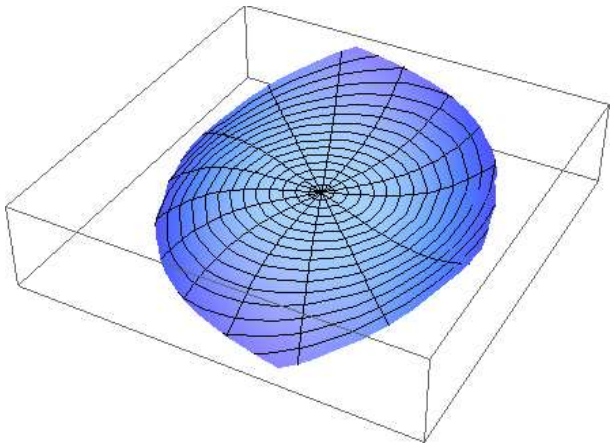

Figure 3.1: An example of a warped disc, produced using the first geometrical approach for: $r_1 = 1/4$, $r_2 = 2$, $z_2 = 1$ and $\alpha = 3$.

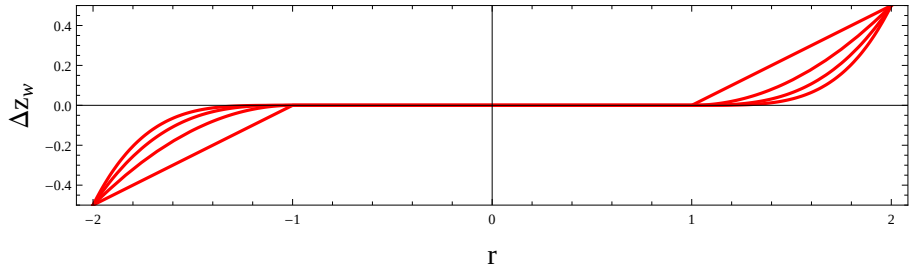

Figure 3.2: The warp function presented in Sec. 3.3.1, for $r_1 = 1$, $r_2 = 2$, $\Delta z_w = 0.5$ and α equal to 1, 2, 3 and 4 (top to bottom curves on the positive r side).

The problem with this approach

This approach has a serious drawback: it produces spatial distortions. The reason is that it displaces points along the vertical direction only, and this distorts shapes. For instance, a circle on the unwarped galactic plane is distorted into an ellipse whose axis ratio increases with radial distance. In the left handed panel of Fig. 3.3, a circular ring is transformed into an elongated elliptical ring by applying a purely vertical displacement, like the one presented here. Moreover, the distortion being introduced is more than just a geometrical nuisance. From the dynamical point of view, we can not justify distorting an originally circular orbit into an elliptical one, so this is a serious flaw for this scheme.

3.3.2 The second approach

In order to solve the above mentioned problem, we introduce the warp in a different way. We now rotate the coordinates around the x–axis with a tilt angle ψ. We specify the tilt angle as a function of the galactocentric spherical radius. For this, we use a function similar to the one used in the first approach (Eq. 3.1), except that it now describes the tilt angles rather than the vertical displacements (see Sec. 3.4 for more details). In the right handed panel of Fig. 3.3, we plot a flat ring that has been transformed into a tilted one using this approach. This warping approach, does not introduce shape distortions. Therefore, we will use it for our warp model. Note that in both of these approaches we define the warp model as function of spherical galactocentric radius not the cylindrical one. The reason for this is that the spherical r stays invariant when applying the either of these two approaches whereas this is not the case for cylindrical radius. This allows us reverse the warping, if necessary, and go back to the initial flat state.

3.4 The untwisted warp model

As a first warp model, we consider a non-precessing warp with a straight line of nodes, i.e. with null twist angle. To accomplish this, we use the second approach explained in Sec. 3.3.2. We rotate the galactocentric Cartesian coordinates around the x-axis with a tilt angle ψ that is a function of the galactocentric spherical radius r:

$$\psi(r; r_1, r_2, \psi_2, \alpha) = \begin{cases} 0, & r \leqslant r_1 \\ \psi_2(\frac{r-r_1}{r_2-r_1})^{\alpha}, & r > r_1 \end{cases} \tag{3.3}$$

where r_1 and r_2 are the galactocentric radii where the warp begins and ends respectively, which are chosen to be at $r_1 = 8$ kpc (roughly taken from with the starting radius of the warp from Reylé et al. 2009) and $r_2 = 20$ kpc. The tilt angle of the warp increases as a power law, and at r_2 it has a value equal to ψ_2. From observations we know that at a galactocentric distance

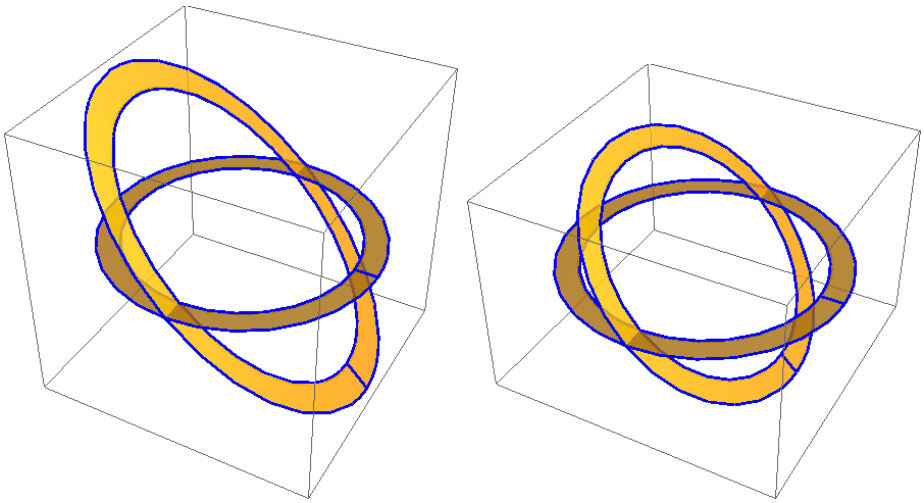

Figure 3.3: *Left*: Distortion introduced by vertical shifting. The horizontal circular ring is elongated by this transformation in the direction orthogonal to the line of nodes. This transformation does not preserve spatial shapes. *Right*: A horizontal ring being warped by the tilt transformation as presented in Sec. 3.3.2. In this case no distortion is introduced in the ring.

of 12 kpc, the maximum height of the warp is about 630 pc (López-Corredoira et al. 2002), which corresponds to a maximum tilt angle of $\sim 3^\circ$ at 12 kpc. By fitting our warp model to these values, we obtain: $\alpha = 2$ and $\psi_2 = 27^\circ$. This model is hereafter called the Untwisted Warp Fiducial (UWF) model. In Figure 3.4, the maximum amplitude of the warp is plotted as a function of galactocentric radius for our UWF model as well as the one obtained from observations by López-Corredoira et al. (2002). Note that our UWF model only resembles the one of López-Corredoira et al. (2002) and we do not pretend to fit the whole trend introduced by them. The UWF model overestimates the values obtained from the observations at large radii. So we introduce another warp model of the same properties but with $\psi_2 = 13.5^\circ$, which we will call hereafter as the Untwisted Warp Half (UWH) model. These two different warps model two extremes of the MW's actual warp. The top panel of Fig. 3.6 shows a schematic plot of a warped disc following the UWF model. In what follows we will use these untwisted models to warp the potential. In order to see how our UWF model affects the disc potential, we present the equipotential contours of the Miyamoto-Nagai disc potential in its original shape and after getting transformed by our UWF model in Fig. 3.5.

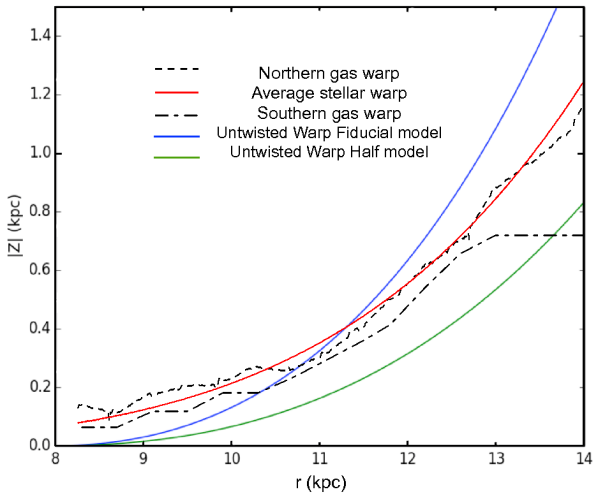

Figure 3.4: Maximum amplitude of the vertical height of the warp as a function of the galactocentric radius for the full and half warp models respectively in blue and green. Black dashed and dot-dashed lines and the solid red line show results from observations as indicated in the legend (López-Corredoira et al. 2002).

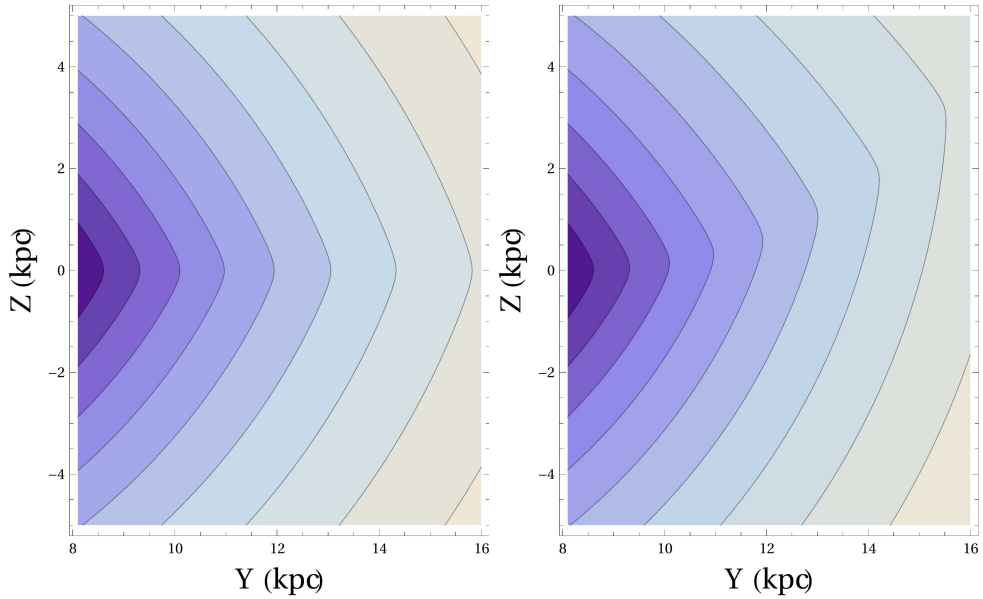

Figure 3.5: The equipotential contours of the Miyamoto-Nagai disc potential before (left-hand panel) and after (right-hand panel) being warped with our UWF model. Notice that in these two plots the scale is the same on both axes.

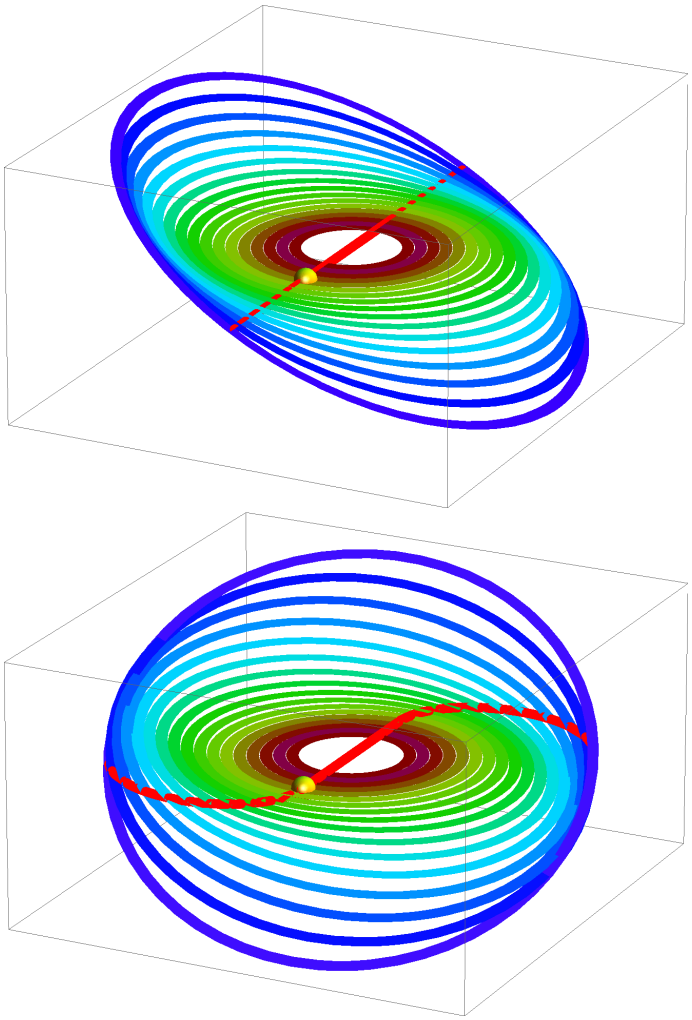

Figure 3.6: Schematic plot of a warped disc. The thick red line shows the line of nodes and the yellow sphere presents the position of the Sun. Top panel shows a warped disc with a straight line of nodes following our UWF model and in the bottom panel we present a warped disc with twisted line of nodes as described in our TW2 model.

3.5 The twisted warp model

In order to model more complex shapes for the galactic warp, we introduce a warp model with a twisted line of nodes. In this model we take the test particles that are integrated and relaxed in the warped potential modelled with the UWF and rotate their phase-space coordinates with respect to the Z-axis. Note that this twist model is used to twist the phase-space coordinates of the particles. We do not apply this model to the potential, because, if we twist the line of nodes of our already warped potential, we do not expect the particles to be able to follow the potential and reach statistical equilibrium with it. The rotation is done using using the following prescription for the twist angle ϕ as a function of radius::

$$\phi(r; r_1, r_2, \phi_{max}) = \begin{cases} 0, & r \leqslant r_1 \\ \phi_{max}(\frac{r-r_1}{r_2-r_1})^2, & r > r_1 \end{cases} \tag{3.4}$$

As for the tilt, the twist begins at $r_1 = 8$ kpc and finishes at $r_2 = 20$ kpc. We consider two twist models in this paper; one with $\phi_{max} = 20°$ and the other one with $\phi_{max} = 60°$, which we hereafter will call the TW1 and TW2 models respectively. These values for ϕ_{max} are chosen to test Gaia capabilities to measure the twist. No observational constrains for this parameter for MW's gas or the stellar component are available at present. From external galaxies we know (according to Briggs 1990, third rule) that at large radii the line of nodes measured in the plane of the inner galaxy advances significantly in the direction of galaxy rotation for successively larger radii, so the line of nodes forms a loosely wrapped leading spiral. Fig. 3.6 bottom panel shows a schematic plot of a warped disc following the TW2 model.

3.6 The warp transformation

3.6.1 The general transformation

We will use two coordinate systems. The first, denoted by (x, y, z) corresponds to the ensemble of particles in the initial flat disc model. The second, denoted by (x', y', z') will correspond to the same test particles, but once the warp has been applied. We will call the map $f : (x, y, z) \rightarrow (x', y', z')$ the "forward transformation" (FWD). Fig. 3.7 shows the FWD transformation: The point p is mapped onto point p'. This transformation is summarised below:

$$f : p \rightarrow p'$$

$$\begin{aligned} x' &= f_x(x, y, z), \\ y' &= f_y(x, y, z), \\ z' &= f_z(x, y, z). \end{aligned} \tag{3.5}$$

In this figure, the original coordinates (x, z) are shown in green while the transformed coordinates (x', z') are shown in red. The original black Cartesian mesh is transformed to the blue mesh and the thick black dashed lines are the original coordinates of p in the warped mesh. Notice that the velocity vector associated to p (red arrow) has been transformed to the one of p' (green arrow) so that it keeps the same orientation with respect to the blue mesh as it had with respect to the black mesh, but its orientation with respect to the final (x', z') coordinate system has changed. We define the inverse (INV) transformation to map the point p' to the point p:

$$
\begin{aligned}
f^{-1} : p' &\rightarrow p \\
x &= f_x^{-1}(x', y', z'), \\
y &= f_y^{-1}(x', y', z'), \\
z &= f_z^{-1}(x', y', z').
\end{aligned} \tag{3.6}
$$

If we want to warp the velocities, we just apply the FWD transformation:

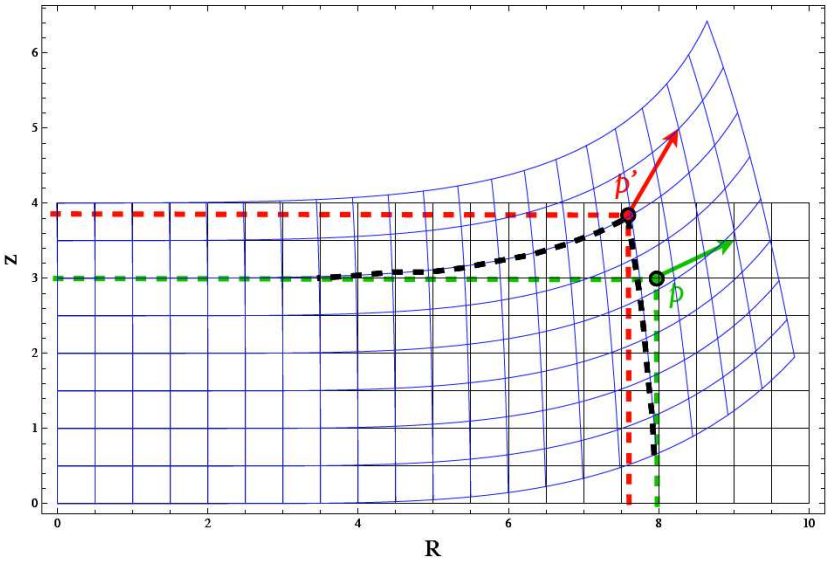

Figure 3.7: An illustration of the warp transformation

$$
\begin{aligned}
v'_x &= f_{v_x}(x, y, z, v_x, v_y, v_z), \\
v'_y &= f_{v_y}(x, y, z, v_x, v_y, v_z), \\
v'_z &= f_{v_z}(x, y, z, v_x, v_y, v_z).
\end{aligned} \tag{3.7}
$$

Notice that the velocity transformation depends on the full phase space coordinates, as opposed to the spatial coordinate transformation that only depends on the original spatial coordinates. Since the transformation is only a rotation with a tilt that depends on galactocentric radius, velocity vectors are re-oriented, but not changed in magnitude.

3.6.2 Warping the phase space coordinates

We now derive the equations needed to achieve this FWD transformation. For the case of the warp, this FWD transformation, is a right-hand rotation along the positive x-axis by an angle ψ (as already mentioned in Sec. 3.4). Applying this warp transformation, in Fig. 3.8, the black ring is transformed to the red one. Similarly, a point with (x, y, z) coordinates is mapped to the (x', y', z') coordinates. To accomplish a rotation of an angle ψ using the x-axis as pivot and in the sense that this is a clockwise rotation when seen from the positive y-axis, we multiply the coordinates by the following rotation matrix:

$$\begin{pmatrix} x' \\ y' \\ z' \end{pmatrix} = \begin{pmatrix} 1 & 0 & 0 \\ 0 & cos(\psi) & sin(\psi) \\ 0 & -sin(\psi) & cos(\psi) \end{pmatrix} \begin{pmatrix} x \\ y \\ z \end{pmatrix} \tag{3.8}$$

where the tilt angle ψ is given by Eq. 3.3. Now, we want to see how the kinematics get affected

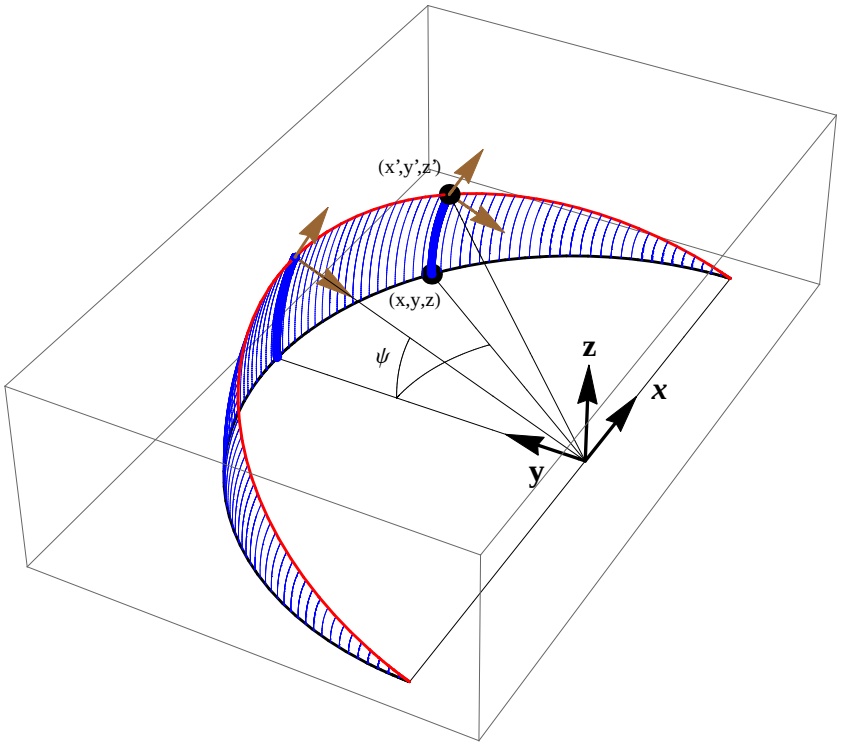

Figure 3.8: Geometry of the warp transformation applied to both positions and the kinematics. The warp transformation is a right-hand rotation along the positive x-axis by an angle ψ. The original coordinates are (x, y, z) , the transformed coordinates are: (x', y', z'). Notice that the tilt produces a rotation of the velocity vectors in the y-z plane. The x component of the velocities is not affected.

by the warp transformation. Looking at Fig. 3.8, we see that that the x-component of the

velocity is not affected by the tilt transformation (remember, the x-axis is the rotation axis), while the y and z velocity components are rotated by an angle ψ in the clockwise direction, when seen from the positive x-axis.

If (V_x, V_y, V_z) are the original velocities in the unwarped model and (V'_x, V'_y, V'_z) are the transformed velocities in the warped model, the transformation equations are given by:

$$\begin{pmatrix} V'_x \\ V'_y \\ V'_z \end{pmatrix} = \begin{pmatrix} 1 & 0 & 0 \\ 0 & cos(\psi) & sin(\psi) \\ 0 & -sin(\psi) & cos(\psi) \end{pmatrix} \begin{pmatrix} V_x \\ V_y \\ V_z \end{pmatrix} \tag{3.9}$$

which we recognize as the same transformation applied to positions (Eq. 3.8). Note that the tilt angle ψ (as given by Eq. 3.3), is a function of the position and therefore the warped velocity components is a function of both initial position and velocity (as seen in Eq. 3.7).

3.6.3 Warping the potential

We now show the way in which the warp transformation is applied to obtain the force field due to the warped disc. Since the potential is a scalar function (as opposed to the force which is a force field), it is much easier to transform the potential and then use the gradient operator on the transformed potential to obtain the warped force field. In Fig. 3.9 we show how is that the potential is warped. Let Φ be the warped potential and Φ_0 the unwarped potential, where we assume that Φ is obtained by applying the warping transformation to Φ_0 . It is then clear that the value of the warped potential at some particular point p, is the same as the value of the unwarped potential but using the coordinates of p in the system where the potential is not warped:

$$\Phi(q') = \Phi_0(q) \tag{3.10}$$

where q' represents the coordinates of the point on the coordinate system where the potential appears warped (red dashed coordinate lines), while q are the coordinates in the system where the potential is not warped (green dashed coordinate lines), e.g. the lines of fixed coordinate q look warped in the coordinate system q'. It is clear to see that:

$$\Phi(q') = \Phi_0(q) = \Phi_0(q[q']) \tag{3.11}$$

Obviously, $q[q']$ is an INV transformation:

$$\Phi(x', y', z') = \Phi_0[f_x^{-1}(x, y, z), f_y^{-1}(x, y, z), f_z^{-1}(x, y, z)] \tag{3.12}$$

The force due to the unwarped potential is simply (green coordinate lines):

$$\overrightarrow{F^0}(q) = -\frac{\partial}{\partial q}\Phi_0(q) \tag{3.13}$$

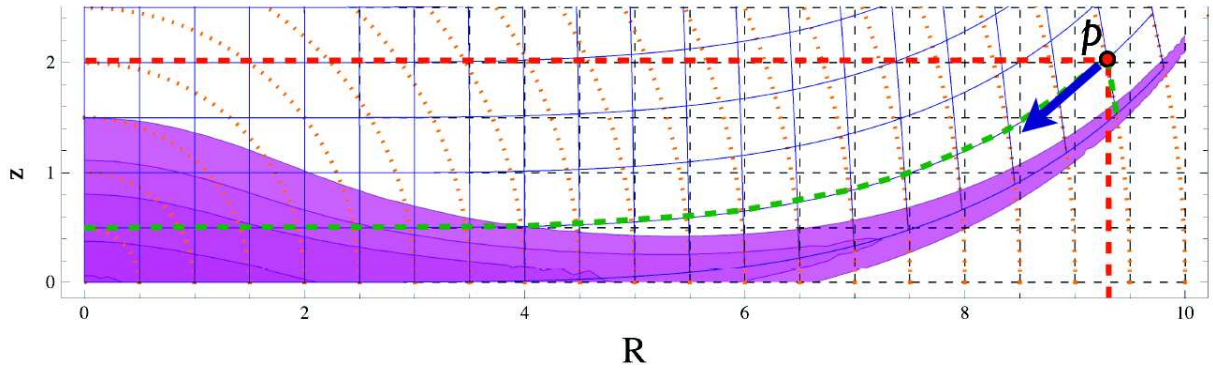

Figure 3.9: An illustration of the warp transformation applied to the galactic disc.

Notice that in Fig 3.9 the force (blue arrow) is parallel to the R-axis of the system where the potential is not warped (green dashed lines). The force due to the warped potential is then (red coordinate lines):

$$\begin{aligned}
\overrightarrow{F}(q') &= -\frac{\partial}{\partial q'}\Phi(q') \\
&= -\frac{\partial}{\partial q}\Phi(q') \cdot \frac{\partial q}{\partial q'} \\
&= -\frac{\partial}{\partial q}\Phi_0(q[q']) \cdot \frac{\partial q}{\partial q'} \\
&= \overrightarrow{F^0}(q[q']) \cdot \frac{\partial q}{\partial q'}
\end{aligned} \tag{3.14}$$

In the first step we have just used the definition of the force. In the second step we have used the chain rule to change to a gradient in the green coordinate system, where the potential is not warped. In the third step we have used the relation between Φ and Φ_0 that we found in Eq. 3.10. In the last step we use expression for the unwarped force in Eq. 3.13. The i-component of the F-force is given by:

$$F_i(q') = \sum_j F_j^0(q)\,\frac{\partial\, q_j}{\partial\, q_i'} \tag{3.15}$$

we must remember that q' is just the coordinates of the point where we want to evaluate the force due to the bended potential, while q are the corresponding coordinates in the coordinate system where the potential is not bended. Since the argument of F is q', we need to do the transformation from it to q, to use as argument of the unwarped potential force. This is accomplished with an INV transformation, f^{-1}. Notice that $\frac{\partial\, q_j}{\partial\, q_i'}$ are the elements of the Jacobian matrix of f^{-1} (see Eq. 3.6).

3.6.4 Forces of the warped Miyamoto–Nagai disc

To calculate the force field of the warped Miyamoto-Nagai potential we follow Eq. 3.15. In this equation F^0 corresponds to the original Miyamoto-Nagai potential and F corresponds to the force due to the warped potential. The (x', y', z') represent the coordinates used to describe the warped potential, while (x, y, z) are the ones used to describe the original flat potential. The INV transformation allows us to go from the first to the latter (see Eq. 3.6). The force field of the flat Miyamoto-Nagai disc potential is as follows:

$$F_x^0 = \frac{x}{(x^2 + y^2 + (a + \sqrt{z^2 + b^2})^2)^{\frac{3}{2}}} \tag{3.16}$$

$$F_y^0 = \frac{y}{(x^2 + y^2 + (a + \sqrt{z^2 + b^2})^2)^{\frac{3}{2}}} \tag{3.17}$$

$$F_z^0 = \frac{z(a + \sqrt{z^2 + b^2})}{\sqrt{z^2 + b^2}(x^2 + y^2 + (a + \sqrt{z^2 + b^2})^2)^{\frac{3}{2}}} \tag{3.18}$$

where a and b coefficients are adopted following A&S potential model (Allen & Santillan 1991), which are as follows: $a = 5.3178$ kpc, $b = 0.2500$ kpc. All we need to do now is to obtain the elements of the Jacobian matrix of f^{-1}.

As mentioned before, our warp model is accomplished by a simple rotation around the x-axis, which constitutes our line of nodes:

$$\begin{pmatrix} x \\ y \\ z \end{pmatrix} = \begin{pmatrix} 1 & 0 & 0 \\ 0 & cos(\psi) & -sin(\psi) \\ 0 & sin(\psi) & cos(\psi) \end{pmatrix} \begin{pmatrix} x' \\ y' \\ z' \end{pmatrix} \tag{3.19}$$

Where $\psi(r') = \psi_2(\frac{r'-r_1}{r_2-r_1})^\alpha$. Note that r' is the spherical galactocentric radius. The $\frac{\partial q_j}{\partial q_i'}$ terms can easily be calculated from Eq. 3.19:

$$\frac{\partial x}{\partial x'} = 1 \tag{3.20}$$

$$\frac{\partial y}{\partial x'} = -y'\, sin(\psi) \left(\frac{\partial \psi}{\partial x'}\right) - z'\, cos(\psi) \left(\frac{\partial \psi}{\partial x'}\right) \tag{3.21}$$

$$\frac{\partial z}{\partial x'} = y'\, cos(\psi) \left(\frac{\partial \psi}{\partial x'}\right) - z'\, sin(\psi) \left(\frac{\partial \psi}{\partial x'}\right) \tag{3.22}$$

$$\frac{\partial x}{\partial y'} = 0 \tag{3.23}$$

$$\frac{\partial y}{\partial y'} = cos(\psi) - y'\, sin(\psi) \left(\frac{\partial \psi}{\partial y'}\right) - z'\, cos(\psi) \left(\frac{\partial \psi}{\partial y'}\right) \tag{3.24}$$

$$\frac{\partial z}{\partial y'} = sin(\psi) + y' cos(\psi) \left(\frac{\partial \psi}{\partial y'}\right) - z' sin(\psi) \left(\frac{\partial \psi}{\partial y'}\right) \tag{3.25}$$

$$\frac{\partial x}{\partial z'} = 0 \tag{3.26}$$

$$\frac{\partial y}{\partial z'} = -sin(\psi) - y' sin(\psi) \left(\frac{\partial \psi}{\partial z'}\right) - z' cos(\psi) \left(\frac{\partial \psi}{\partial z'}\right) \tag{3.27}$$

$$\frac{\partial z}{\partial z'} = cos(\psi) + y' cos(\psi) \left(\frac{\partial \psi}{\partial z'}\right) - z' sin(\psi) \left(\frac{\partial \psi}{\partial z'}\right) \tag{3.28}$$

Where:

$$\frac{\partial \psi(r')}{\partial x'} = \frac{\alpha\ \psi_2\ x'}{r'(r_2 - r_1)} \left(\frac{r' - r_1}{r_2 - r_1}\right)^{\alpha - 1} \tag{3.29}$$

$$\frac{\partial \psi(r')}{\partial y'} = \frac{\alpha\ \psi_2\ y'}{r'(r_2 - r_1)} \left(\frac{r' - r_1}{r_2 - r_1}\right)^{\alpha - 1} \tag{3.30}$$

$$\frac{\partial \psi(r')}{\partial z'} = \frac{\alpha\ \psi_2\ z'}{r'(r_2 - r_1)} \left(\frac{r' - r_1}{r_2 - r_1}\right)^{\alpha - 1} \tag{3.31}$$

Now using these elements of the Jacobian matrix, the warped force field in Cartesian coordinates can easily be calculated using Eq. 3.15.

4

Building the warped test particle ensembles

4.1 The Initial conditions

In this chapter we describe how we get the random realization of the initial flat disc, and the way in which the warping is applied. We generated random realizations of the density distribution that corresponds to the Miyamoto-Nagai disc used in the A&S Galactic model. This is done using the Hernquist method (Hernquist 1993) (see Appendix A for more details). The velocity field is approximated using gaussians whose first order moments are set by Jeans' equations with the epicyclic approximation. The asymmetric drift is taken into account in the computation of the tangential components of the velocities. We generated test particles to represent three different stellar populations: red clump K-giant (RC) stars, and main sequence A and OB type stars. For them, we assign the corresponding scale height and velocity dispersions at the Sun's position for each test particle ensemble (see Table 4.1). The total number of stars for each tracer are shown in Table 4.2. These are calculated in such a way that the number of stars of each tracer in a cylinder of radius 100 pc centred on the Sun position is normalized to the number found in this cylinder using the new Besançon Galaxy Model (Czekaj et al. 2014). We locate the Sun at Galactocentric cartesian coordinates $(-8.5, 0, 0)$ kpc. We adopt a circular velocity for the Local Standard of Rest (LSR) of $V_c(R_\odot) = 220$ kms^{-1} which is consistent with our imposed potential model, i.e. A&S model. Also, we consider a peculiar velocity of the Sun with respect to the LSR of $(U, V, W)_\odot = (11.1, 12.24, 7.25)$ kms^{-1} (Schönrich et al. 2010).

The Galactic warp is a feature of the outer parts of the Galactic disc. In order to avoid integrating the path of particles that will not be of use later, after generating the initial conditions,

Table 4.1: The velocity dispersions (σ_U, σ_W) of different stellar tracers at the Solar neighbourhood and the corresponding disc scale heights (z_d) (Aumer & Binney 2009).

Tracer	RC	A	OB
σ_U [km/s]	30	15	10
σ_W [km/s]	16	9	6
z_d [pc]	300	100	50

Table 4.2: The local surface number density (Σ) and the total number of stars of each tracer. Number of stars outside the lindblad hole refers to the number of stars with apocentre radius larger than 8 kpc.

Tracer	RC	A	OB
Σ $[stars/pc^2]$	0.056	0.048	0.003
Number of stars	57×10^6	48×10^6	3.2×10^6
Number of stars outside the Lindblad hole	36×10^6	30×10^6	1.8×10^6

we discard the ones whose apocentre radius is smaller than 8 kpc. This is done using the Lindblad diagram as explained in Appendix B. This technique is valid for spherical potentials only, but in the limit of particles with very limited vertical motion as our disc particles, this should not introduce a serious error. In Table 4.2 the total number of stars satisfying this condition is presented.

4.2 Adiabatic and Impulsive regimes

We apply our untwisted warp models to the Miyamoto-Nagai disc potential of A&S. In order to be able to integrate the test particles in this warped potential, we use the warped forces calculated in Sec. 3.6.4.

Starting from a set of test particles that are relaxed in the A&S potential, if we abruptly bend the disc potential, the particles will loose their near-circular orbits and increase their velocity dispersion. To avoid this, we should warp the potential adiabatically, in other words, we should do it slowly enough, so that the particles can follow the bended potential and not be left behind. To do this, we make ψ_2, the maximum tilt angle parameter in our warp transformation (see Eq. 3.3), a function that grows with time and reaches its maximum value ψ_{max} at time t_{grow}. To describe a gradual increase, we use the following function from Dehnen (2000):

$$\psi_2 = \psi_{max}\left(\frac{3}{16}\xi^5 - \frac{5}{8}\xi^3 + \frac{15}{16}\xi + \frac{1}{2}\right), \;\; \xi \equiv 2\frac{t}{t_{grow}} - 1. \tag{4.1}$$

Where $-1 \leq \xi \leq 1$ and ψ_2 varies smoothly and has null derivatives at both ends of the range. In order to get an idea of how slow the warping process should be, we run some test simulations with one particle at an initial circular orbit at 14 kpc from the Galactic centre. In Fig. 4.1 we plot the integrated path of this particle while the potential is gradually being warped. The warping is introduced progressively through a time $t_{grow} = n \times P$ where P is the orbital period of a star with a circular orbit at 20 kpc in the A&S potential which is about 590 Myr. In the quickly warped potential, i.e. in an impulsive regime, the particle acquires a sizeable amount of motion orthogonal to the instantaneous plane of the warped disc potential, whereas in the adiabatic case, the particle moves along this warped disc. In order to warp the potential in the adiabatic regime we choose $t_{grow} = 6P$ which is about 3.5 Gyr. This is not meant to be an actual time-scale in which a warping may develop in a real galactic disc, as we are not simulating an actual warping mechanism. Rather, this is the time-scale for our warping transformation meant to provide us with a reasonable set of particles within a warped potential.

Warping the disc adiabatically with time gives us an ensemble that is in statistical equilibrium which means the mean values of the parameters of the system (for instance in this case, the vertical motions) are invariant with time. This can be clearly seen in Fig. 4.1, in the part of the particle's orbit that corresponds to the time where the particle is integrated in the final state of the wraped potential (the blue lines). For the case of $n = 6$, where the warping is done adiabatically, the particle keep its circular orbit within the warped plane of the disc whereas for $n = 1$ and $n = 0.125$, where the potential gets warped in a very short time scale, the particle gain some vertical motion with respect to the instantaneous plane of the warped disc. In this thesis our main focus is on simulating warped systems that are in statistical equilibrium. This is due to the fact that the behaviour of the system that is warped in impulsive regime depends on the initial conditions and the behaviour of the agent that is responsible for the warp. These will add more free parameters to our model and therefore we try to avoid it. Nevertheless, in Chap. 9 we perform simulations with impulsive warp generation, but the aim of this study is only to try to mimic the qualitative trend seen in observations with the simulations (See Sec.9.5.1 for more details).

4.3 The integration process

The 3D numerical integration of test particle orbit in the galactic potential is performed using a 7-8 th order Runge-Kutta integrator with adaptive time step (Dormand & Prince 1981). The integration is done in three stages as shown in Fig. 4.2. First, we integrate the initial conditions in the flat A&S potential, to allow them to reach a reasonable state of statistical equilibrium with this axisymmetric potential. The integration time at this stage depends on the velocity dispersion of the tracer, the colder they are, the more time they need to reach the statistical equilibrium with the potential. After some trial and error, and being conservative, we opted for an integration time of 10 Gyr for RC stars, 20 Gyr for A type stars and 30 Gyr for OB stars.

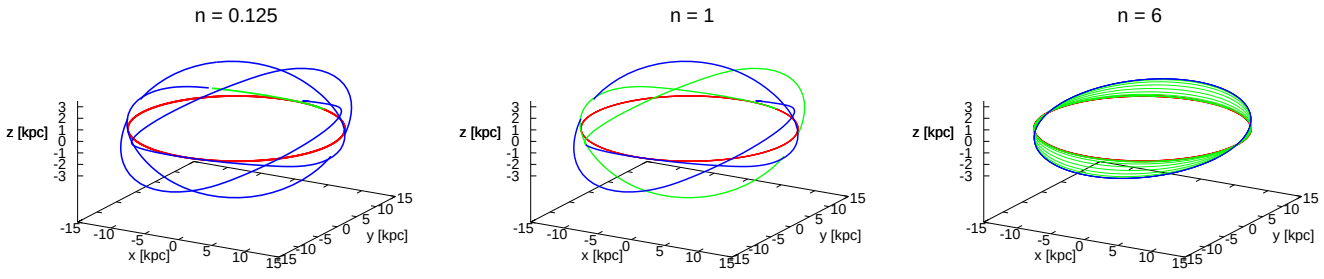

Figure 4.1: The orbit of a star with an initial circular orbit with a Galactocentric radius of 14 kpc integrated for $t_1 = 2P$ in the A&S potential with a flat Miyamoto-Nagai disc (in red), then integrated for $t_{grow} = n \times P$ while the disc potential is gradually being warped as a function of time (see Eq. 4.1) (in green) and finally integrated for $t_2 = 2P$ in the final state of the warped potential (in blue). Each panel shows the orbits for different values of n. Note that P is the orbital period of a star with a circular orbit in the A&S potential located at 20 kpc. It is clear that as we increase the value of n, i.e. warping the potential more slowly, the star can follow the potential more closely and acquire less motion orthogonal to the instantaneous plane of the warped disc potential. Choosing $n = 6$, the potential is being warped adiabatically enough that the star can keep its circular orbit within the warped plane.

Next, we adiabatically warp the potential for $t_{grow} = 3.5$ Gyr. In the last part, we integrate the particles in the final state of the warped potential for $t_2 = 2P$ to let the particles relax in this newly warped potential. Again, we do not pretend this is an actual time during which real stars have orbited unperturbed around the Galaxy. This is just a time to relax our initial conditions within the assumed potential. In order to check for the energy conservation during the stages where the potential is time independent, in Fig. 4.3 we plot the relative energy during the orbit integration for a particle with an initial planar circular orbit at $r = 14$ kpc. The colors correspond to the integration strategy as illustrated in Fig. 4.2. We can see that the energy is conserved in the red and blue parts and it is not in the green part. This is something we expect, as in this green part the potential is a function of time and thus, energy is being introduced. Having checked different circular and eccentric orbits, we conclude that during the stages where the potential is time independent, energy conservation is better than 0.01% in all cases. For the cases where we want to generate a twisted warp, twisting the line of nodes (see Sec. 3.5) is done at this point, i.e. after finishing the integration. The samples we get here are the *Perfect samples* to which we will refer later in this paper.

A point that must be considered is that, when applying the warp transformation to a potential, the corresponding density (in the sense of being proportional to the Laplacian of the transformed potential) does not coincide with the density that is obtained from applying the transformation to the original density function. This may introduce a discrepancy, in the sense

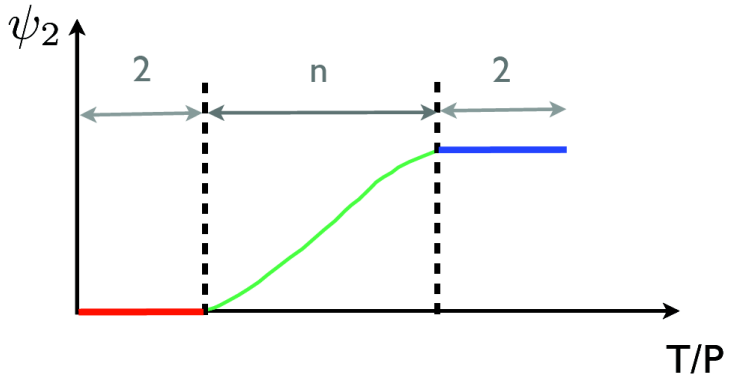

Figure 4.2: The strategy used for integrating the test particles. Note that P is the orbital period of a star with a circular orbit at 20 kpc in the A&S potential. The colors correspond to those used in Fig. 4.1.

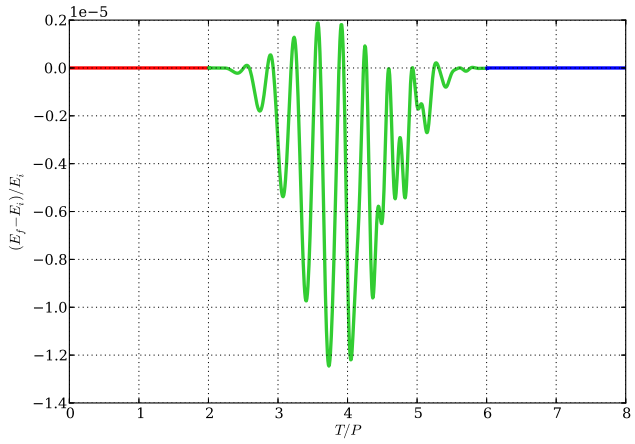

Figure 4.3: The relative energy as a function of integration time over P (P is the orbital period of a star with a circular orbit at 20 kpc in the A&S potential). In the red and blue parts where the potential is not changing with time, the energy is conserved. The colors correspond to those used in Figs 4.1 and 4.2.

that the parameters of the estimated warp (obtained using the test particle distribution) do not coincide with those that were applied to the potential. However, we must point out that we are only recovering the tilt and twist angles that define the transformed planes of symmetry of the original functions and these do coincide, as the Laplacian preserves these planes. This is shown in Fig. 4.4, where we present the equipotentials of the warped Miyamoto-Nagai disc potential (UWF model),together with the isodensity contours of the warped density function. Notice that their planes of symmetry coincide.

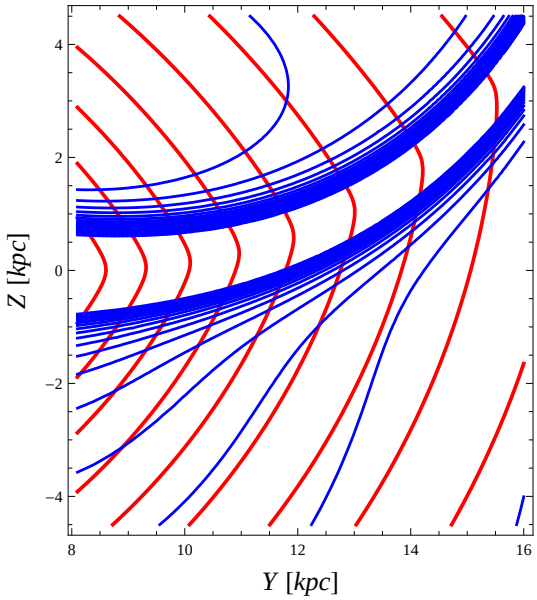

Figure 4.4: The equipotential and isodensity contours of the warped Miyamoto-Nagai disc potential of the A&S model respectively in red and blue. The plot is done in the Y-Z plane for X=0. It is clear that the position of the warped plane of symmetry coincides for both, warped potential and warped density function.

In Fig. 4.5 we present the final snapshot of the simulation for different stellar populations in X-Y and Y-Z projections. In X-Y projection we can see a hole in the centre which is due to discarding stars whose orbits are in the central part of the Galaxy using Lindblad diagram (see Appendix B). Note that in Y-Z projection, we can see density peaks in red locating slighty above and below the plane at respectively y$\sim$5 kpc and y$\sim$-5 kpc. This is just due to the fact that stars with various X positions are projected on the Y-Z plane and the ones with large X coordinate, have non-zero tilt angles and therefore they get projected above the plane at the positive Y-axis and below the plane at negative Y. Again note that the reason why we do not get a density peak at the centre in Y-Z projection is due to the Lindblad hole we impose.

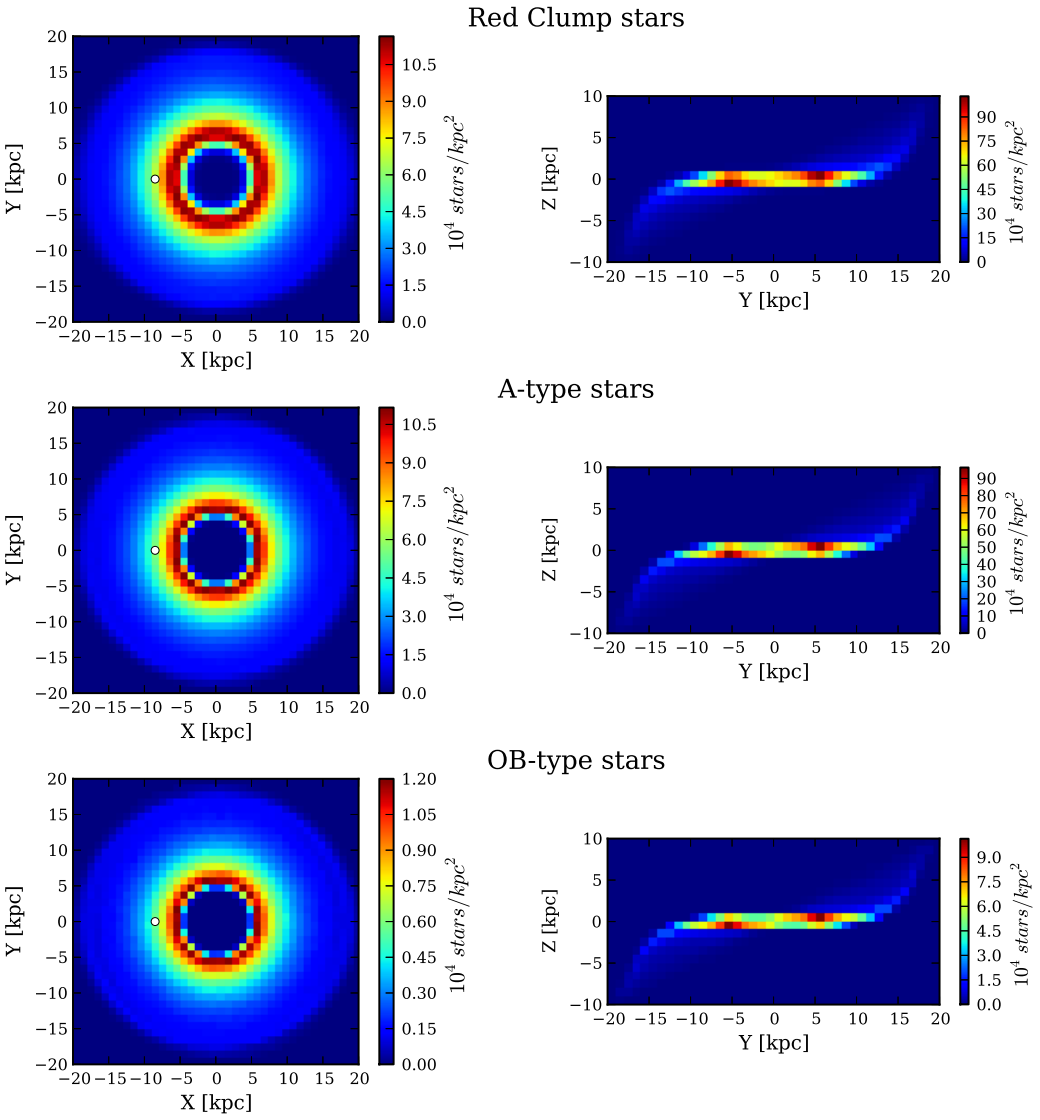

Figure 4.5: The distribution of stars of each warped tracers (warped with UWF model) in X-Y (left panels) and Y-Z (right panels) planes. The distribution of RC, A and OB stars are shown in the top, middle and bottom panels respectively. The colour scale indicates the surface density (10^4 stars / kpc^2). This scale is different for each tracer population to better illustrate the surface density. Note that the Sun is located at $(x, y, z) = (-8.5, 0, 0)$ kpc as labelled with a white filled circle in the left panels. Therefore, in the Y-Z projection, the Sun is projected on top of the Galactic centre at Y=0.

Part III

Methods for warp detection and characterization

5

The LonKin methods

5.1 Introduction

In a warped galactic disc, stars that follow the plane of the disc acquire a vertical velocity component that varies as a function of position along the orbit. For the case of a warp formed by flat tilted rings, as those introduced by our warp transformation (see Eq. 3.3), the variation in vertical velocity is sinusoidal with its extrema at the galactocentric azimuths that correspond to the line of nodes and becoming zero at the azimuths that correspond to the line orthogonal to the line of nodes (see Fig. 5.1).

From our warp simulation we obtain the 6 dimensional phase-space components of the warped stellar population which are in galactocentric coordinates. Using equations 1.2, 1.3 and 1.4, we calculate their heliocentric (U, V, W) velocity components. Finally, their proper motion along Galactic longitude, $\mu_l\, cos(b)$, and towards Galactic latitude, μ_b, is computed as follows:

$$k\,\rho\,\mu_b = -sin(b)cos(l)\,U - sin(b)sin(l)\,V + cos(b)\,W \tag{5.1}$$

$$k\,\rho\,\mu_l\,cos(b) = -sin(l)\,U + cos(l)\,V \tag{5.2}$$

Where ρ is the heliocentric distance to the star, l and b are the Galactic longitude and latitude, respectively. And, $k = 4.74\ \frac{\mathrm{kms}^{-1}}{\mathrm{mas\,yr}^{-1}\,\mathrm{kpc}}$ is a coefficient for unit conversion. In what follows, we discuss in detail how a warped disc will affect the trend of vertical velocity component and μ_b proper motion. In this chapter we introduce a couple of related methods that aim to identify

the signature of a flat tilted rings warp model based in the vertical motion of the star in the warp.

5.2 LonKin1

As mentioned before, the warp of the Galactic disc only affects the vertical motion of the stars. Therefore, the best way of detecting its kinematic signature is to look at the W velocity component of stars. We define the *LonKin1* method to be the trend of medians of W velocities as a function of Galactic longitude seen in different galactocentric radius bins. First, we use this method to check the W trend of the full sample of RC stars relaxed in the flat, axisymmetric A&S potential, so that we can use this trend later as a control case. In Fig. 5.2 top panel we can see a constant trend of W as a function of longitude which is expected, since the disk is flat and the medians of the vertical velocities do not change significantly in longitude in an axisymmetric potential. But we expect this median value to be equal to zero, whereas in this plot, it has a value of about $-7.25\ \mathrm{km\,s^{-1}}$. This is due to the fact that the Sun has a positive vertical motion with respect to the LSR ($w_\odot$), therefore, as seen from the Sun, the vertical velocity of all the stars will be subtracted by $w_\odot \sim 7.25\ \mathrm{km\,s^{-1}}$. In Fig. 5.2 bottom panel, we correct for this Solar motion, and we can see a constant zero trend for the W velocity components.

Now, we perform this analysis on the Perfect sample of warped RC stars (see Sec. 4.3). Results are shown in Fig. 5.3; in top panel we show the results for the median W velocities and in bottom panel we present the ones after correcting for the vertical Solar motion. We can see a sinusoidal like behaviour that is following what we explained before with Fig. 5.1. Note that in the later figure, the trend is shown as a function of galactocentric azimuth and that's why it has a perfect sinusoidal shape. Whereas in Fig. 5.3, the use of Galactic longitude lead us to get a distorted sinusoidal trend with a flat peak. This trend is what is expected since sweeping in equal longitude bin sizes, we cover the $l = 180°$ direction more densely than any other directions. Therefore, the maximum value of W can be seen in a larger region in longitude compared to galactocentric azimuth.

Since the amplitude of the warp grows with galactocentric radius, in order to see the effect of this growth on kinematics, we bin the stars in galactocentric distances of 1 kpc starting from 9 kpc to 15 kpc. In Fig. 5.3, we can see that the amplitude of the trend increases with radius which was expected; having stars reaching larger vertical displacements requires higher vertical velocities. Also note that as you go to larger distances, the corresponding figure approaches the pure sinusoidal form, since the difference in position between the Sun and the galactic center becomes less important. It is worth mentioning that when plotting the W as a function of Sun-centered galactic longitude, the W=0 points do not locate at the same longitude for different galactocentric radii. For instance, moving from $r = 10$ kpc to $r = 15$ kpc, the longitudes at which the W velocity is zero changes from $l \sim 50°$ to $l \sim 60°$. This effect is present at Fig. 5.3, but perhaps it is a bit difficult to see due to its scale. In both Figs 5.2 and 5.3 the error bars

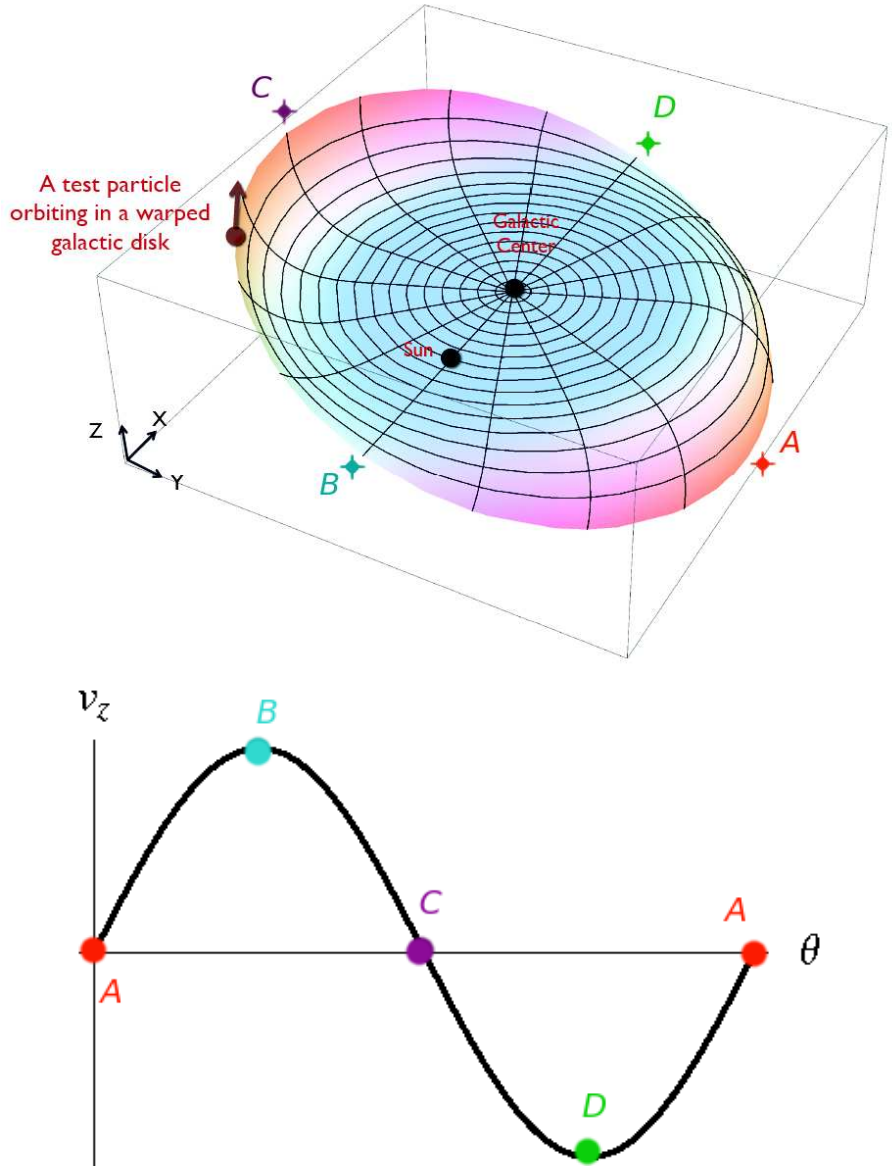

Figure 5.1: *Top*: A schematic plot of a particle in circular orbit within a warped disc formed by tilted flat rings. The positions of the galactic center and the Sun are indicated with black dots. Four particular positions along the orbit (A through D) are indicated. *Bottom*: the corresponding plot of the particle vertical velocity as a function of galactocentric azimuth. The corresponding points to those in the top panel are indicated. Notice that the vertical velocity reaches its extrema at the azimuths that correspond to the line of nodes, and become zero along the line orthogonal to it.

are the standard error of the median which are calculated for a 95% confidence level which is given by the $\frac{N}{2} - \frac{1.96\sqrt{N}}{2}$ and $1 + \frac{N}{2} + \frac{1.96\sqrt{N}}{2}$ ranked values of the ordered set of N data.

5.3 LonKin2

Since one of the aims of this thesis is to check how Gaia will observe the warp kinematic signature, we should look for this signature in the space of Gaia observables, that is proper motions for this case. We already know that the Galactic warp is a galactocentric feature and studying its kinematic signature in the space of Gaia observables, we better look into the galactocentric components of the proper motion, namely $\mu_l\, cos(b)$ and μ_b. Comparing two samples of stars being integrated in A&S potentials with a flat and a warped disc, we see that the warp does not significantly affect the trend of median values of $\mu_l\, cos(b)$ proper motion as a function of Galactic longitude at any radii. This was expected because $\mu_l\, cos(b)$ proper motion only depends on the U and V velocity components which lie on the plane and are not significantly affected by the warp.

The *LonKin2* method is defined to be the trend of median values of μ_b as a function of Galactic longitude for different galactocentric radius bins. It is important to note that Solar motion can bias the observed μ_b trend as it did affect the observed W velocity component. In order to illustrate this fact, in Fig. 5.4 top panel, we plot the μ_b vs. Galactic longitude trend of stars orbiting in a A&S potential with a *flat* disc. Here we would expect to get an almost constant trend around zero, but the vertical motion of the Sun gives a convex shape to it and this trend vanishes as moving to larger radii. These are due to the fact that that the artificial proper motion produced by the Solar motion, $\mu_{b\odot}$, not only depends on the Solar motion but also it is a function of heliocentric distance to each star ($\rho_\star$):

$$k\,\rho_\star\,\mu_{b\odot} = -sin(b_\star)cos(l_\star)\,U_\odot - sin(b_\star)sin(l_\star)\,V_\odot + cos(b_\star)\,W_\odot \tag{5.3}$$

In Fig. 5.4 Bottom panel, we correct for this motion and we obtain a constant, zero trend. In Fig. 5.5, we show the results for the Perfect sample of warped RC stars. In the top panel the results of the observed μ_b are presented and the bottom panel corresponds to the same, but after correcting for the Solar motion. Here again, the growth of the amplitude of the trend with radius is clear. The reason for such a trend is a bit more complex than the one for the W velocity vector since μ_b comes from two sources; one is the W velocity, which certainly increases with the galactocentric distances, but the other is the distance, which enters dividing, and so, the farther away, the smaller the proper motion you see. So whether you see a larger effect in μ_b as you move further out depends on the relative effects of the larger W produced by the warp, vs. the inverse dependence on distance. For this case the W effect seems to dominate, therefore the peak in μ_b grows with distance. Again, in both Figs 5.4 and 5.5 the error bars are the standard error of the median which are calculated for a 95% confidence level.

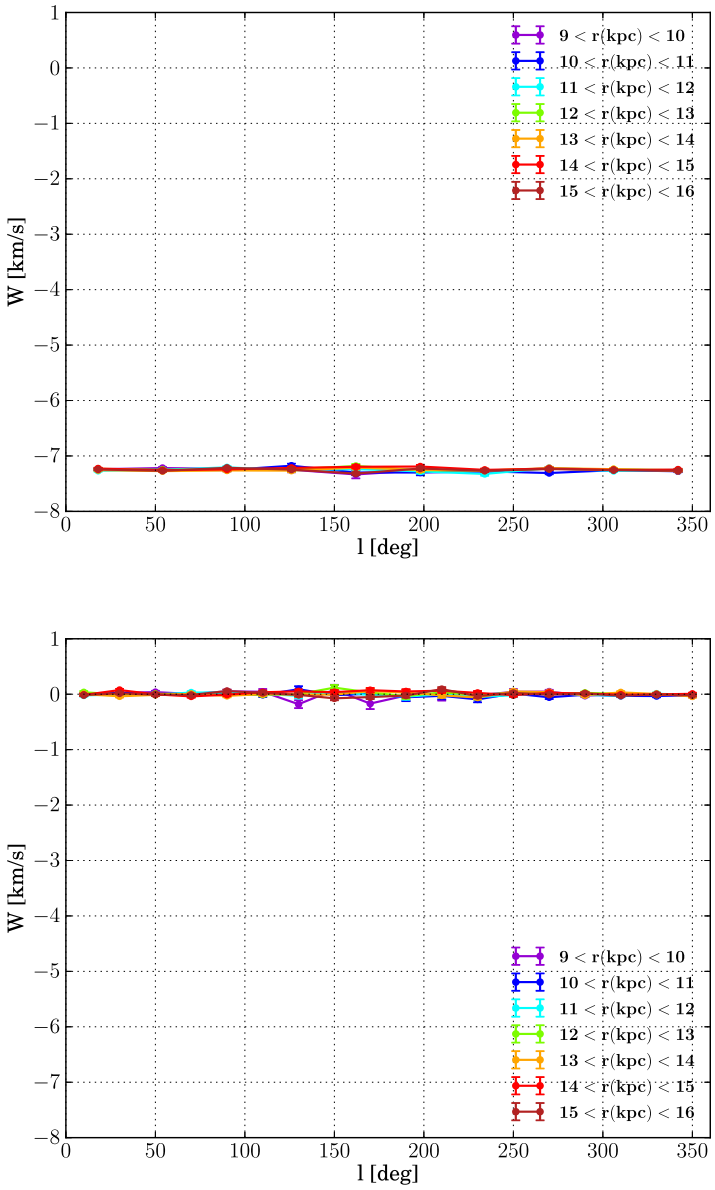

Figure 5.2: Top: The median values W velocity component as a function of Galactic longitude for different galactocentric radius bins for the full sample of RC stars relaxed in the flat, axisymmetric A&S potential. Bottom: Same as top panel but corrected for the vertical velocity of the Sun. The error bars show the standard error of the median which are calculated for a 95% confidence level.

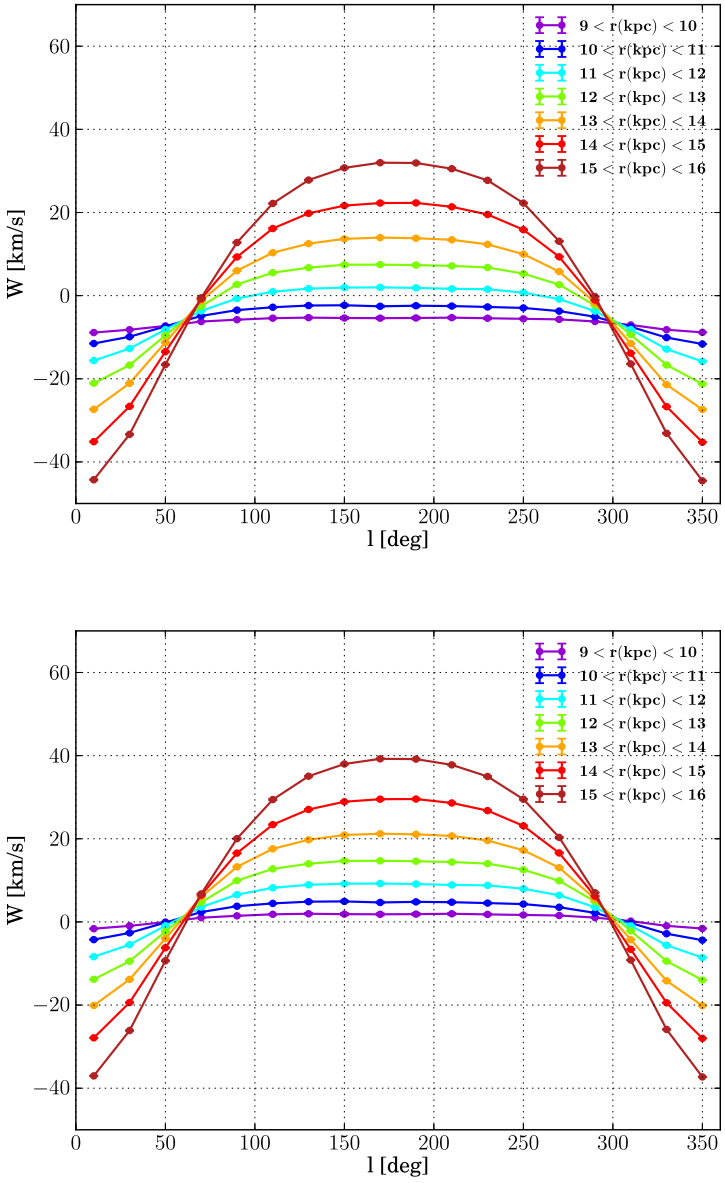

Figure 5.3: Top: The median values W velocity component as a function of Galactic longitude for different galactocentric radius bins for the Perfect sample of warped RC stars (see Sec. 4.3). Bottom: Same as top panel but corrected for the vertical velocity of the Sun. The error bars show the standard error of the median which are calculated for a 95% confidence level. The computed errors of the median are typically < 0.3 km s^{-1}.

Hereafter, the results using LonKin1 and LonKin2 methods will always be presented after removing Solar vertical motion. Also, note that the reason why we use medians instead of means is that when applying these methods to the real data, medians help us to remove the effect of outliers and decrease the influence of contaminations (see Sec. **??** and 8.3 for more detailed discussion). However, for the Perfect samples that we used here, since they are simulated samples and we know for sure that they do not suffer from contaminations, the proper motions and vertical velocities have normal distributions and therefore means and medians of these parameters are equal.

In order to be get a more realistic idea about the W and μ_b trends of MW, we also studied how spiral arms can change the expected trends seen in Fig. 5.5 and 5.3 bottom panels. For this, we perform a test particle simulation using the A&S axisymmetric potential and the 3D PERLAS model for the spiral arms (Pichardo et al. 2003). We have not found any significant trend in vertical motion caused by spiral arms. More details on this study can be found in Appendix C.

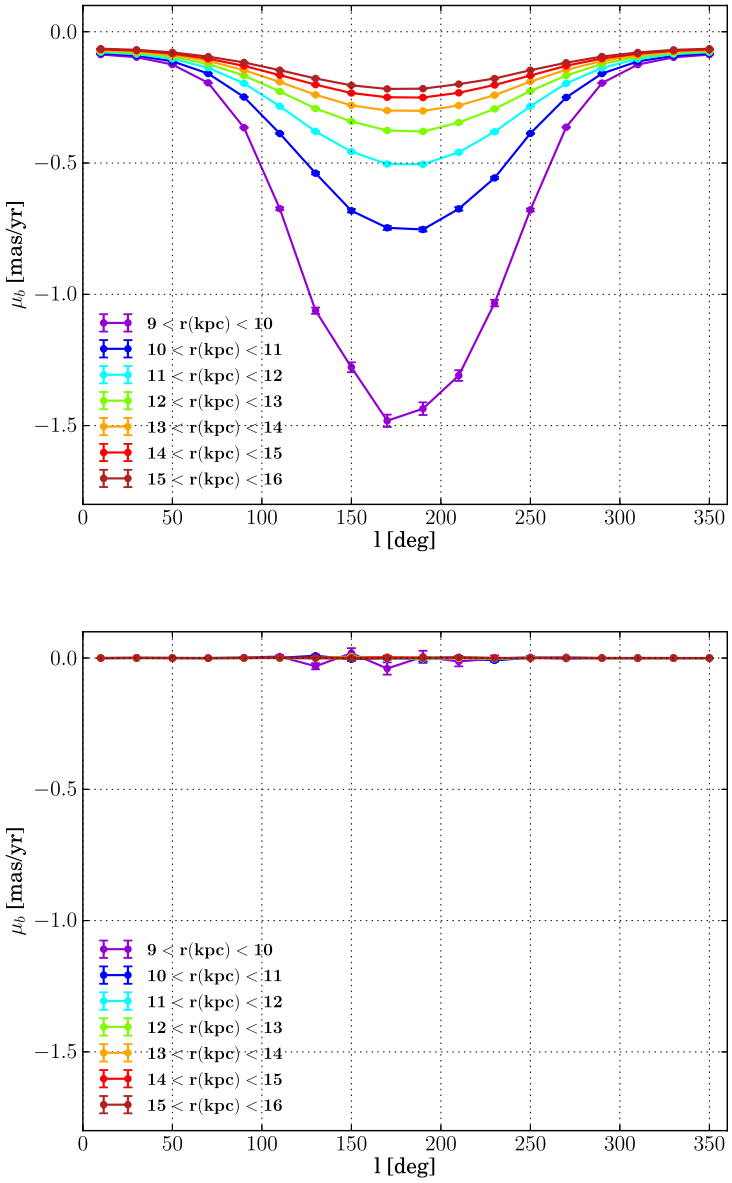

Figure 5.4: Top: The median values of μ_b proper motion as a function of Galactic longitude for different galactocentric radius bins for the full sample of RC stars relaxed in the flat, axisymmetric A&S potential. Bottom: Same as top panel but corrected for the vertical motion of the Sun. The error bars show the standard error of the median which are calculated for a 95% confidence level.

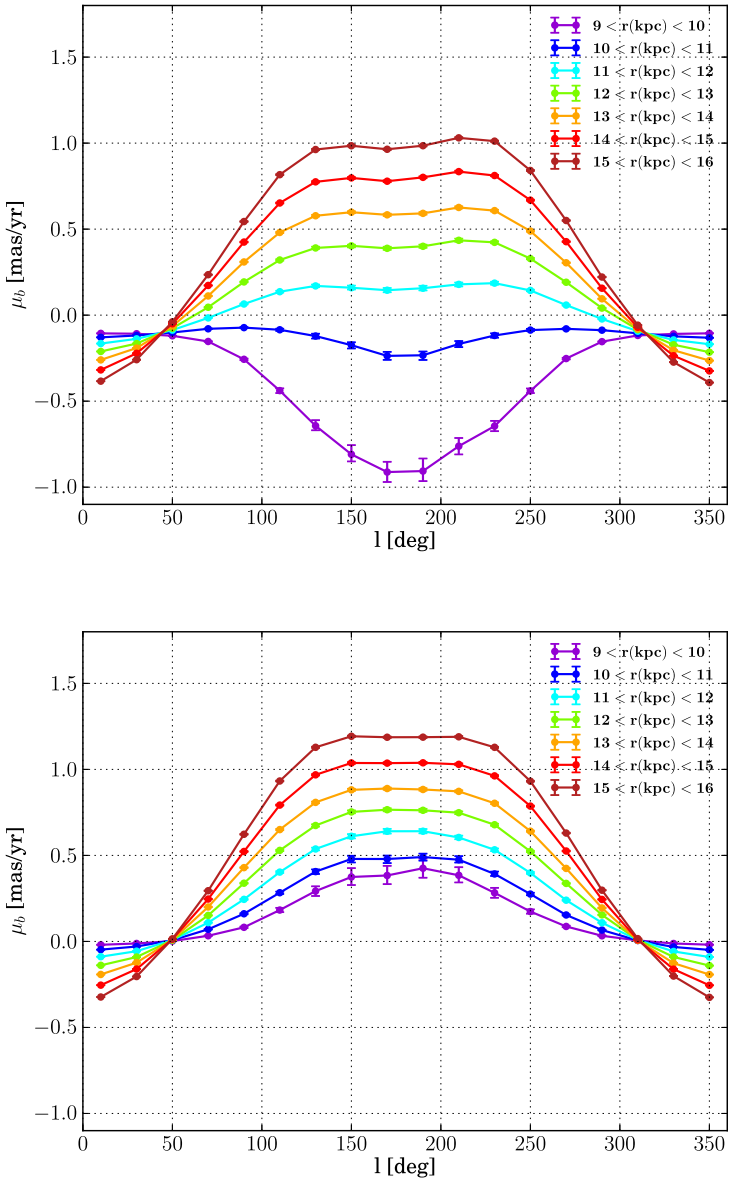

Figure 5.5: Top: The median values μ_b proper motion as a function of Galactic longitude for different galactocentric radius bins for the Perfect sample of warped RC stars. Bottom: Same as top panel but corrected for the vertical motion of the Sun. The error bars show the standard error of the median which are calculated for a 95% confidence level.

6

Great Circle Cell Counts methods

6.1 The mGC3 method

The modified Great Circle Cell Counts method (mGC3) was introduced by Mateu et al. (2011) as a technique for the detection of tidal streams in the Galactic Halo, based on the original GC3 method proposed by Johnston, Hernquist & Bolte (1996) for the same purpose. The mGC3 method is based on the fact that, in a spherical potential, the tidal stream produced by the disruption of a satellite in the Galactic Halo will conserve its total angular momentum and its orbit will be confined to a plane, which will be an exactly constant plane if the potential is perfectly spherical, or will precess if it is axisymmetric. Therefore, as seen from the Galactic centre, the stars in the stream are confined to a great circle band, the projection of the orbital plane. This means that *both* the Galactocentric position and velocity vectors of stream stars are perpendicular, within a certain tolerance, to the normal vector or *pole* $\hat{\mathbf{L}}$ which defines this particular great circle.

The mGC3 method thus consist in producing a *pole count map*[1], i.e. a map of the number of stars associated to each possible pole (and therefore great circle cell) in a grid in spherical coordinate angles (directions), computed as the number of stars which, for each pole, fulfil the following criteria

[1]The Python package PyMGC3 containing code to run the mGC3/nGC3/GC3 family of methods is publicly available at the github repository https://github.com/cmateu/PyMGC3

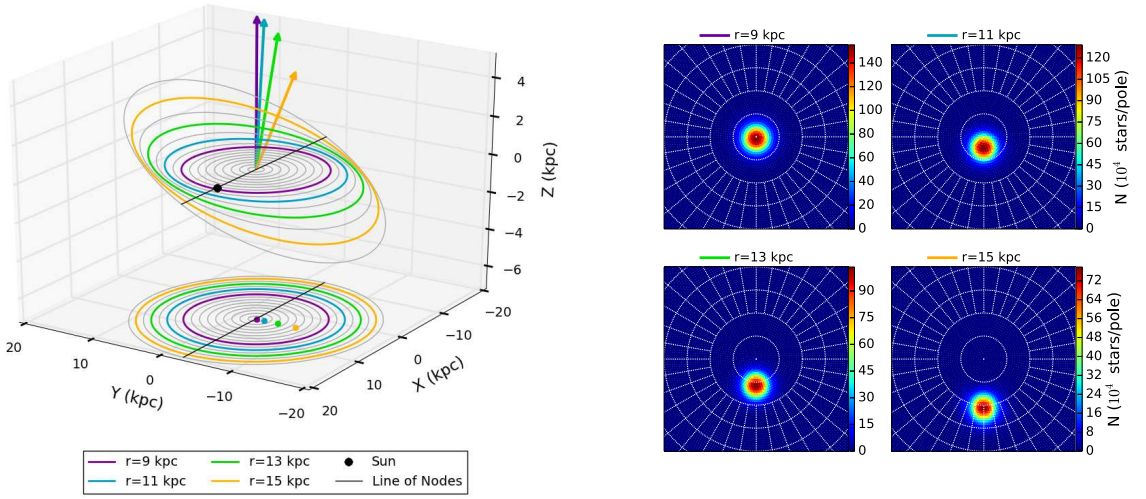

Figure 6.1: *Left:* Schematic plot of a warped disc (UWF model). The solid black line and black dot indicate respectively the line of nodes and the Sun's position. Concentric circles shown in gray increase in Galactocentric radius by 1 kpc, with colours showing four selected rings at 9 (purple), 11 (blue), 13 (green) and 15 kpc (orange). The arrows represent the normal vectors corresponding to each of these rings, in the same colour. The projection in the X-Y plane shows the tips of the normal vectors, aligned along the direction perpendicular to the line of nodes, which in this case is a straight line. *Right:* The 2×2 mosaic shows the pole count maps which correspond to stars in spherical shells with the same radii as the coloured rings indicated in the left panel. The simulated A stars are used to generate these plots. The maps are shown in an a north-polar azimuthal equidistant projection, showing the north pole at the centre, $\varphi = 90^\circ - 270^\circ$ in the vertical direction at the centre of the plot, the concentric circles have a separation of 5°, and meridians are drawn at 10° intervals in longitude. The colour scale shows the number of stars associated to each pole according to the mGC3 criteria of Equation 6.2. Each of the pole vectors indicated by the arrows in the left panel correspond to the pole with maximum counts in the pole count map for the respective radius. The sequence of plots clearly shows how the position of the pole with the maximum star counts shifts in latitude when the radius r increases, in the same way that is shown by the arrows shown in the left panel, as a consequence of the increase in the tilt angle $\psi(r)$. The azimuthal angle φ of the maximum counts pole (and the corresponding arrows) remains constant as expected for a straight line of nodes.

$$|\hat{\mathbf{L}}_i \cdot \hat{\mathbf{r}}_{\rm gal}| \leq \delta_r \quad \text{and} \quad |\hat{\mathbf{L}}_i \cdot \hat{\mathbf{v}}_{\rm gal}| \leq \delta_v \tag{6.1}$$

where $\hat{\mathbf{r}}_{\rm gal}$ and $\hat{\mathbf{v}}_{\rm gal}$ are unit vectors in the direction of the star's (Galactocentric) position and velocity vectors respectively, δ_r and δ_v are the tolerances and $\hat{\mathbf{L}}_i$ is the i-th vector on the grid of all poles considered. The modification mGC3 introduces to the original GC3 method is the use of the velocity criterion in Equation 6.1, which as shown in Mateu et al. (2011), increases the efficiency of the method by reducing substantially the background contamination. Also, in order to avoid the distance bias introduced by the reciprocal of the parallax (Brown et al. 2005), Mateu et al. (2011) use the criteria of Equation 6.1 expressed in the following equivalent manner

$$|\hat{\mathbf{L}}_i \cdot \mathbf{r'}_{\rm gal}| \leq \|\mathbf{r'}_{\rm gal}\|\delta_r \quad \text{and} \quad |\hat{\mathbf{L}}_i \cdot \mathbf{v'}_{\rm gal}| \leq \|\mathbf{v'}_{\rm gal}\|\delta_v \tag{6.2}$$

where $\mathbf{r'}_{\rm gal}$ and $\mathbf{v'}_{\rm gal}$ are simply the position and velocity vectors $\mathbf{r}_{\rm gal}$ and $\mathbf{v}_{\rm gal}$, multiplied by the parallax, which in terms of the heliocentric observable quantities $(l, b, \varpi, v_r, \mu_l, \mu_b)$ are given by

$$\begin{aligned} \mathbf{r'}_{\rm gal} &= \varpi \mathbf{r}_\odot + A_p\big((\cos l \cos b)\hat{\mathbf{x}} + (\sin l \cos b)\hat{\mathbf{y}} + (\sin b)\hat{\mathbf{z}}\big) \\ \mathbf{v'}_{\rm gal} &= \varpi \mathbf{v}_\odot + \varpi v_r \hat{\mathbf{r}} + (A_v \mu_l \cos b)\hat{\mathbf{l}} + (A_v \mu_b)\hat{\mathbf{b}} \end{aligned} \tag{6.3}$$

where $A_p = 10^3$ mas pc, $A_v = 4.74047$ yr kms^{-1}, $\{\hat{\mathbf{x}}, \hat{\mathbf{y}}, \hat{\mathbf{z}}\}$ are Cartesian unit vectors and $\{\hat{\mathbf{r}}, \hat{\mathbf{l}}, \hat{\mathbf{b}}\}$ are the unit vectors in heliocentric Galactic coordinates (for full details see Mateu et al. 2011).

The mGC3 method is ideally suited to study and characterize a warp with a fixed tilt angle for each Galactocentric ring, similar to our untwisted warp models. For a flat disc, pole count maps made for stars in bins with increasing (Galactocentric) distance r will show a maximum located always at the North Galactic Pole. For a tilted ring model of a warped disc (see Sec. 3.4), each of the rings has a tilt angle $\psi(r)$ which will yield maximum counts at a pole located at a latitude $\theta = \pi/2 - \psi(r)$.

Figure 6.1 illustrates the pole count maps obtained when applying the mGC3 method to the sample of A stars, warped with the UWF. The left panel shows a 3D schematic plot of the warp model. Concentric rings in gray show the mid-plane of the warped disc, with radii increasing in steps of 1 kpc. The line of nodes is shown as a black solid line and the position of the Sun indicated with a filled black dot. Four particular rings (at 9, 11, 13 and 15 kpc) and their respective pole vectors are emphasised in colours (see figure caption and legend). The tips of the pole vectors are indicated as filled circles in the X-Y plane projection, with the same colours. The plot shows how the pole vectors deviate from the Z-axis with an angle equal to the tilt angle of the respective ring, which increases with Galactocentric r. Since there is no twisting, the pole vectors have a constant azimuthal angle φ and their tips are distributed along a straight line in the X-Y plane projection. The right part of the plot shows a 2×2 mosaic, with the pole count

maps corresponding to each of the four coloured rings shown on the 3D plot (left). To generate these pole count maps we use the full sample of A stars, warped with the UWF. The top left panel shows the map for the innermost ring, at a radius of 9 kpc, which has a very small tilt angle ($\psi = 0.2°$) and the maximum pole counts located almost exactly at $\theta = 90°$, at the very centre of the map. As the radius increases, the maximum counts signature moves towards lower latitudes as $\theta = \pi/2 - \psi(r)$, exhibiting the dependence of the tilt angle with distance. Note also the maximum pole counts displace only in latitude, as expected for a warp with no twisting, remaining at a constant azimuthal angle which defines the direction perpendicular to the line of nodes.

A warped model *with* twisting is illustrated in Figure 6.2, with the same layout and colour scheme as in Figure 6.1. The warp model shown is the TW2 (see Sec. 3.5). The left plot shows how the line of nodes is twisted for radii larger than 8 kpc, as seen also in the X-Y projection where the tips of the pole vectors are shown to deviate from the straight line these followed in Figure 6.1. The array of pole count maps illustrates how in this case, in addition to the displacement in the latitudinal direction, now the maximum counts pole also shifts in the azimuthal direction with an angle that increases with distance as the twist angle does. Here the RC stars sample that is warped with TW2 is used for generating the pole count maps.

It is worth emphasizing that mGC3 maps provide a means for empirically measuring the tilt and twist angles of the warp as a function of distance, in a completely non-parametric way, without making any assumptions on the functional form of this dependence. The only assumption that is implicitly being made is that the warp is symmetric, in the sense of the tilt angle being the same on either side of the line of nodes, which will produce a single peak in the pole count maps.

6.2 The new nGC3 method

Since the use of mGC3 requires all six-dimensional phase-space information, it is also worth while exploring the performance of the method when introducing a couple of variations, when less information is available. The largest restriction when using all positional and kinematical information comes from the magnitude limit set for the measurement of radial velocities by Gaia, which restricts the sample to $G_{RVS} < 17$ (see Sec. 7.2.1). Therefore, we also explore the performance of mGC3 omitting the radial velocity term, $\varpi v_r \hat{\mathbf{r}}$, in Equation 6.3 and using only proper motion information. In this way we trade less kinematical information for a larger sample. In the following analyses we will refer to this new variation as *nGC3* (no-radial velocity mGC3). Additionally we produce pole count maps using only the positional criterion in Equation 6.2, i.e. using the GC3 method[2].

[2]The original GC3 method as devised by Johnston et al. (1996) uses heliocentric coordinates (l, b) rather than Galactocentric. Here we use a Galactocentric GC3 method

It is clear that the lack of radial velocity information will introduce limitations. The use of proper motions in nGC3 helps in reducing the contamination in comparison to GC3, which uses only positional information, though lacking the information provided by the radial velocity necessarily implies that there will still be some contamination left over. The contamination will have a larger effect in different directions, depending on whether or not the radial velocity component of stars in the feature we're interested in (in this case the disc) has a large contribution to the full velocity vector or not. For instance, for disc stars in the direction towards the Galactic centre or anti-centre ($l = 0°, 180°$), the radial velocity component is negligible and so the full velocity vector is well approximated by its tangent velocity. The position and velocity vectors of stars in these directions give a good handle on the definition of a preferential plane of motion. On the other hand, in the perpendicular direction ($l = 90°, 270°$), the projection of the velocity vector of disc stars in the radial direction is not negligible at all, which means stars in these directions are more prone to contamination and thus the identification of a preferential plane is more uncertain. In spite of this, we deem this effect to be negligible since our interest lies on disc stars which by far dominate star counts in all directions. Contamination from Halo stars is expected to be at most $\sim 1\%$ (Carney et al. 1990), based on solar neighbourhood star counts, but it would even vanish when using a tracer such as OB stars, present only in very young populations; or even MS A-type stars, more massive than the Halo F turn-off.

We expect the use of kinematical information to yield a cleaner peak signature in the mGC3 and the nGC3 pole count maps. This is illustrated in Figure 6.3, where we show mGC3, nGC3 and GC3 pole count maps, from left to right, for the 13 kpc ring in the warp model illustrated in Figure 6.1 using the A stars sample. The colour bar shows the number of stars associated with each pole for each of the maps. As expected, the number of star counts is much larger for the GC3 and nGC3 methods, which allow the use of all stars up to the Gaia limiting magnitude $G = 20$. It is clear that nGC3 and mGC3 maps provide a much narrower and well-defined peak with nearly zero background counts, providing a clear example of the great benefit of having proper motions; whereas the peak in the GC3 pole count map is more extended, in particular in the latitude direction, and is embedded in a higher and noisier background. In the following analysis we will evaluate the performance of these three methods in the recovery of the tilt and twist angles for different warp models and tracer populations.

6.3 The peak finder procedure

In order to identify the position (φ_o, θ_o) of the peak in a pole count map, we have used a Bayesian framework which provides a straightforward way to compute also the associated uncertainties.

First, we switch to a Cartesian north-polar azimuthal equidistant (NPAE) projection of the pole count maps (such as those of Figures 6.1-6.3), rather than using an Aitoff projection of the spherical coordinates, in which the peak finding analysis is more difficult due to the curvature inherent to the coordinate system. Since we are only interested in finding the position of the

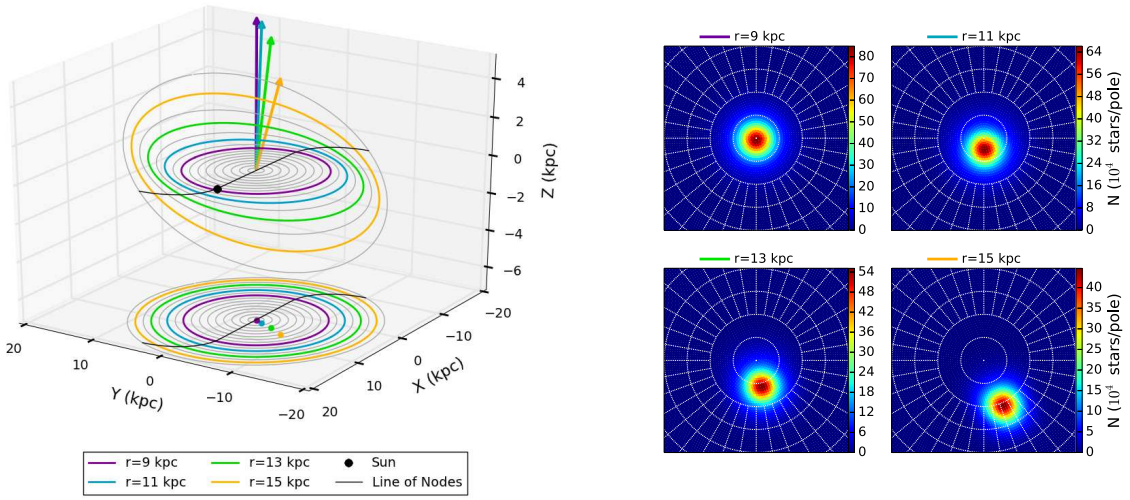

Figure 6.2: Same as Figure 6.1 for a warp model with a twist. *Left:* Schematic plot of a warped disc of TW2. The projection in the X-Y plane shows the tips of the normal vectors, which now deviate from the Y=0 axis with an angle that increases proportionally with radius due to the twisting of the line of nodes. *Right:* The sequence of pole count maps shows how, in addition to the shift in latitude caused by the tilting of the rings, the position of the pole with the maximum star counts now also shifts in the azimuthal direction with φ increasing as r does, illustrating the twisting of the line of nodes as a function of radius depicted in the left panel.

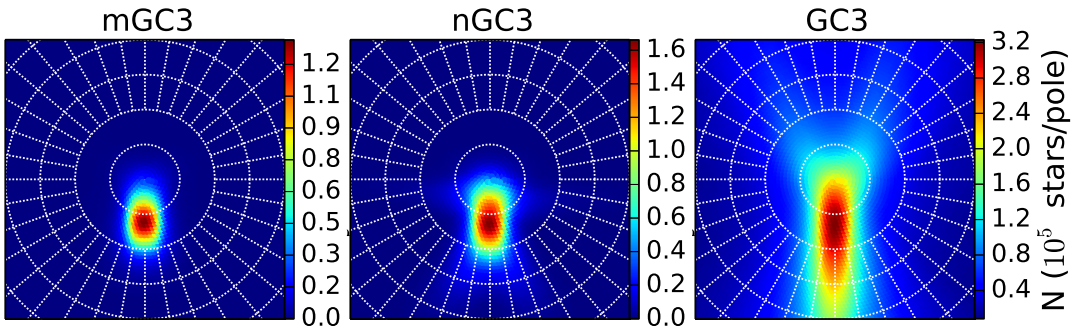

Figure 6.3: Pole count maps produced with the mGC3 (*left*), nGC3 (*centre*) and GC3 (*right*) methods, for the 13 kpc ring shown in the warp model of Figure 6.1. The colour scale indicates the number of stars associated to each pole. Note that the warped A stars sample with UWF, is used for generating these pole count maps.

peak and not in modelling its entire shape accurately, we assume it can be described by a simple two-dimensional Gaussian in the Cartesian projection, which we express as

$$N_M(x,y) = Ae^{-\frac{(x-x_o)^2}{2\sigma_x^2}} e^{-\frac{(y-y_o)^2}{2\sigma_y^2}} \tag{6.4}$$

where we have assumed independence in x and y by omitting the crossed terms σ_{xy} of the covariance matrix. Also, we restrict the sample to grid points with pole counts higher than 60% of the maximum counts, since we only intend to use the Gaussian model in the area right around the peak. For the observed pole counts N_i we assign typical Poisson counting errors $\sigma_i = \sqrt{N_i}$. We assume these errors to follow a Gaussian distribution [3], and thus we express the logarithm of our likelihood function $L = p(\{N\}|x_o, y_o, \sigma_x, \sigma_y, A)$ as

$$\ln L = \sum_{i=1}^{n} -\frac{(N(x_i,y_i) - N_M(x_i,y_i))^2}{2\sigma_i^2} \tag{6.5}$$

which gives the probability of having observed a set $\{N\}$ of pole count measurements, for a given set of model parameters $\{x_o, y_o, \sigma_x, \sigma_y, A\}$.

We assume uniform prior probability distributions for all our model parameters, in the following allowed ranges: A between the minimum and ten percent plus the maximum observed counts; x and y, between the minimum and maximum values given by the Cartesian pole grid; σ_x and σ_y, between zero and half the range spanned by the Cartesian pole grid. Our posterior probability $p(x_o, y_o, \sigma_x, \sigma_y, A|\{N\})$ is then simply proportional to the likelihood in Equation 6.5.

Samples from the posterior distribution were obtained by using the Markov Chain Monte Carlo (MCMC) sampler *emcee* from Foreman-Mackey et al. (2013), which provides a Python implementation of an affine-invariant MCMC sampler (Goodman & Weare 2010). The *emcee* sampler has the advantage of providing an MCMC algorithm with very few free parameters (see Foreman-Mackey et al. 2013, for full details): the number of 'walkers' (the number of simultaneous chains to be used), the number of burn-in steps and the total number of final chain steps. The sampler parameters were set to 300 walkers with 150 and 200 burn-in and total steps respectively, which resulted in acceptance fractions in the range $\sim 0.25 - 0.4$ and auto-correlation times ~ 15 times smaller than the total duration of the chain, well within the ranges suggested by Foreman-Mackey et al. (2013).

Finally, the MCMC (x, y) values are transformed back to spherical coordinates (φ, θ). For this distribution of (φ, θ), which corresponds to a sampling of the marginalized posterior probability $p(\varphi_o, \theta_o|\{N\})$, we compute the median, 15.8th and 84.2th percentiles which we take respectively as the best estimate and the asymmetric 1σ confidence intervals for (φ_o, θ_o) (Hogg et al. 2010).

[3] This is a reasonable assumption since typically N is very large ($> 10^4$).

In the following chapter we describe the results obtained when applying our peak finding algorithm to the pole count maps obtained using the different GC3 methods. To generate the pole count maps in all of the cases, we used a tolerance of $\delta_r = \delta_v = 2^\circ$ and a pole grid spacing of 0.5°. We checked that using smaller values for the tolerance ($\delta_r = \delta_v = 1^\circ$, 0.5°) and the pole grid spacing (0.25°), does not change the results significantly.

Part IV

The kinematic signature of the MW warp

7

Evaluating Gaia capabilities to characterise the Galactic warp

7.1 Introduction

Up to now we have been dealing with test particle ensembles which have been integrated in a way that they contain an imprint of the warped model we want to characterise. Some information about the stellar population they represent has been used in setting their initial kinematical properties (e.g. velocity dispersions), but that has been all.

To use our ensemble of particles to build Gaia mock catalogues and see to what extent it is that we can recover the characteristics of our warp models from them, it is now necessary to assign stellar properties that allow us to compute what their Gaia photometric parameters would be, and from them assign errors to the Gaia observables according to a Gaia error model. We also have to apply a galactic extinction model and filter out our initial perfect ensembles to generate the samples that Gaia would presumably observe, including the biases and random errors in their observables. This is what we do in this chapter. At the end, we present the results obtained with the GC3 family of methods as well as LonKin methods when applied to our Gaia mock catalogues.

7.2 The Gaia "observed samples"

7.2.1 The Gaia selection function

Measuring the unfiltered (white) light in the range of 350–1000 nm, Gaia yields G magnitudes. Stars brighter than $G = 20$ can be observed. The Radial Velocity Spectrometer (RVS) implemented inside Gaia, provides radial velocities through Doppler-shift measurements. This instrument will integrate the flux of the spectrum in the range of 847–874 nm (region of the CaII triplet) which can be seen as measured with a photometric narrow band yielding G_{RVS} magnitudes. These measurements are collected for all stars up to $G_{RVS} = 17$. These two passbands are illustrated in Fig. 7.1. For the sample whose kinematics mimics RC stars, we assign

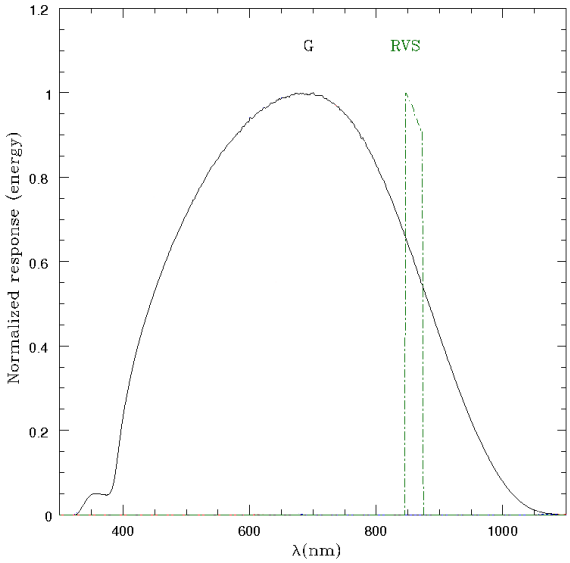

Figure 7.1: Gaia G (solid line) and G_{RVS} (dot-dashed line) normalised passbands as presented in Jordi et al. (2010).

an absolute magnitude of $M_k = -1.62$ (Alves 2000) and an intrinsic colours of $(J-K)_o = 0.55$ (Straižys & Lazauskaitė 2009), $(V-I)_o = 1.0$ and $(V-K)_o = 2.34$ (Alves 2000) to each star. We calculate the visual absorption, A_V, using the 3D extinction map of Drimmel et al. (2003) using rescaling factors. The rescaling factors are used to correct the dust column density of the smooth model to account for small scale structure not described explicitly in the parametric dust distribution model. Using the extinction laws from Cardelli, Clayton & Mathis (1989), $A_K = 0.114\,A_V$ and $A_J = 0.282\,A_V$, we calculate the apparent K magnitude and observed

colour for every individual star:

$$K = m_K + 5\log(r_h) - 5 + 0.14\,A_V \tag{7.1}$$

$$(J-K) = 0.168\,A_V + (J-K)_0 \tag{7.2}$$

Note that r_h is the heliocentric distance of the star in parsec. The G magnitude is then calculated as a function of K apparent magnitude and $(J-K)$ observed colour as follows (J.M. Carrasco, private communication):

$$\begin{aligned} G = K &- 0.286 + 4.023(J-K) - 0.35(J-K)^2 \\ &+ 0.021(J-K)^3 \end{aligned} \tag{7.3}$$

$$\begin{aligned} G_{RVS} = K &- 0.299 + 2.257(J-K) + 0.042(J-K)^2 \\ &- 0.002(J-K)^3 \end{aligned} \tag{7.4}$$

For A stars, the visual absolute magnitudes are assigned using the luminosity function interpolated from Murray et al. (1997) to generate stars in the range of $[A0, A9]$:

$$\phi_A(m_V) = 0.77\,m_V - 0.967 \tag{7.5}$$

Which is in units of stars per 1000 pc^{-3}. The $(V-I_C)$ colours are obtained from the absolute magnitude and colour relation presented in Kenyon & Hartmann (1995). For OB stars, the visual absolute magnitudes are obtained using the luminosity function from Mottram et al. (2011) in units of $\mathrm{stars\,kpc^{-3}\,mag^{-1}}$:

$$log(\phi_{OB}(m_V)) = (0.6 \pm 0.06)\,m_V + (4.12 \pm 0.13) \tag{7.6}$$

The corresponding $(V-I_C)$ colours are calculated using the absolute magnitude, effective temperature and colour relations interpolated from the corresponding tables of Mottram et al. (2011) and Jordi et al. (2010). The G and G_{RVS} magnitudes for the two latter mentioned tracers are calculated using the third order polynomial fit of V apparent magnitudes and $(V-I_C)$ observed colours of Jordi et al. (2010):

$$\begin{aligned} G = V &- 0.0257 - 0.0924(V-I_C) - 0.1623(V-I_C)^2 \\ &+ 0.0090(V-I_C)^3 \end{aligned} \tag{7.7}$$

$$\begin{aligned} G_{RVS} = G &+ 0.0138 - 1.1168(V-I_C) + 0.1811(V-I_C)^2 \\ &- 0.0085(V-I_C)^3 \end{aligned} \tag{7.8}$$

Considering stars with $G < 20$, in Fig. 7.2 we plot the surface density of stars in X-Y and Y-Z cartesian projections for the three tracers. This is a similar plot as Fig. where we plot the

surface density for the perfect samples. Note that the colour scale is different in these two cases so that the observed features are enhanced. Looking at the Y-Z projection, the warped shape of the disc is clearly seen even after applying the Gaia selection function. From the X-Y projections it is clear that A stars are less visible to Gaia in the first and fourth quadrants compared to RC and OB stars since they are not as bright as OB stars, or as red as RC stars. As expected, the RC population has a larger scale height as seen in Y-Z projection.

7.2.2 The Gaia error model

The Gaia web-page[1] provides science performance estimates and models for nominal errors in astrometric, photometric and spectroscopic data. The end-of-mission parallax errors depend on G magnitudes and $(V-I_C)$ colours. Fig. 7.3 right hand panel, shows the mean parallax accuracy horizons for stars with different spectral types that represent our three tracers. We also take into account the variation of errors as a function of ecliptic coordinates, due to the variation in the number of transits at the end of the mission. The Galactic coordinates and proper motion errors are described as a function of the error in parallax. The end-of-mission radial velocity errors depend on the V magnitudes and the spectral type of the stars. The redder they are, the smaller error in their radial velocity measurements. Applying the 3D extinction map, Gaia observational constrains and these error models to our perfect sample, we generate the Gaia "observed catalogues" for the three tracers. Note that all the Gaia errors applied in this thesis are according to the nominal models which are slightly underestimated compared to the ones obtained at the time of the In-Orbit Commissioning Review (July 2014). This is presented in Fig. 7.3 left hand panel, where we present the mean parallax accuracy horizons estimated after commissioning phase considering the unexpected effect of stay light of the Gaia.

7.2.3 Characteristics of the observed samples with and without velocity information

It is essential for our study to know how many stars will be observed by Gaia as a function of Galactocentric radius for each tracer population. We also have to know for how many of them Gaia provides radial velocity information and also how many with good parallax measurements. Figure 7.4 shows the histograms in logarithmic scale of the number of stars in (spherical) Galactocentric radius bins of 1 kpc, starting from 9 kpc up to 16 kpc for the three tracers. It is worth noting that for the samples with error in parallax less than 20% ($\Delta\varpi/\varpi < 0.2$) the number of A stars drops down by three orders of magnitude at large radii while this reduction is only one order of magnitude and less than one for RC and OB stars respectively. This is because RC and OB stars are intrinsically brighter than A stars.

In Fig. 7.5 we plot the surface densities of each stellar population *after* applying the Gaia

[1] http://www.cosmos.esa.int/web/gaia/science-performance

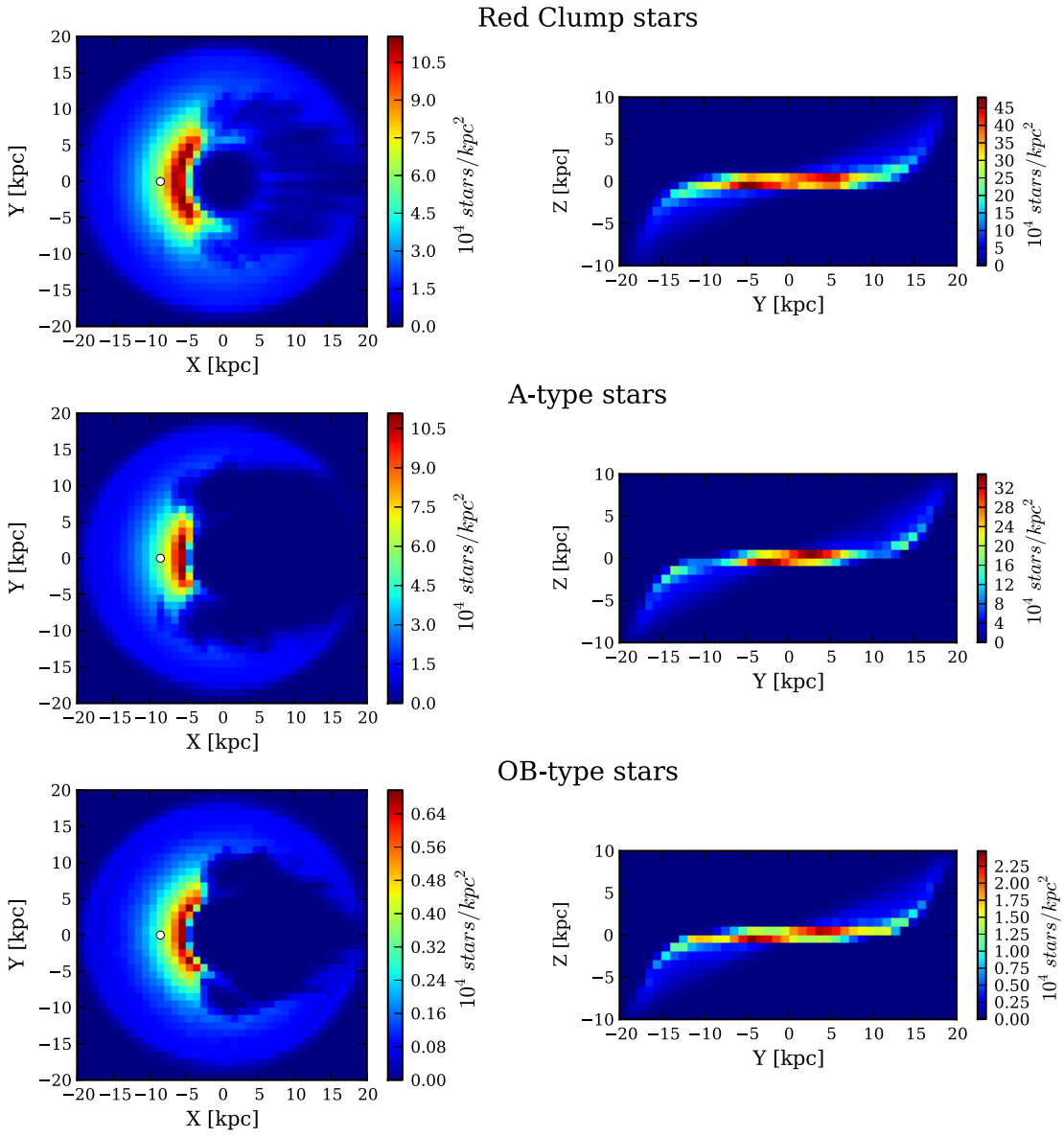

Figure 7.2: The distribution of stars of each warped tracers (warped with UWF model) in X-Y (left panels) and Y-Z (right panels) planes. These are the stars observable with Gaia (i.e. with apparent magnitudes $G < 20$). The distribution of RC, A and OB stars are shown in the top, middle and bottom panels respectively. The colour scale indicates the surface density (10^4 stars / kpc^2). This scale is different for each tracer population to better illustrate the surface density. The 3D extinction map of Drimmel et al. (2003) is used for calculating the apparent magnitudes. Note that the Sun is located at $(x, y, z) = (-8.5, 0, 0)$ kpc as labelled with a white filled circle in the left panels. Therefore, in the Y-Z projection, the Sun is projected on top of the Galactic centre at Y=0. It is worth mentioning that the distances used in this plot are true distances.

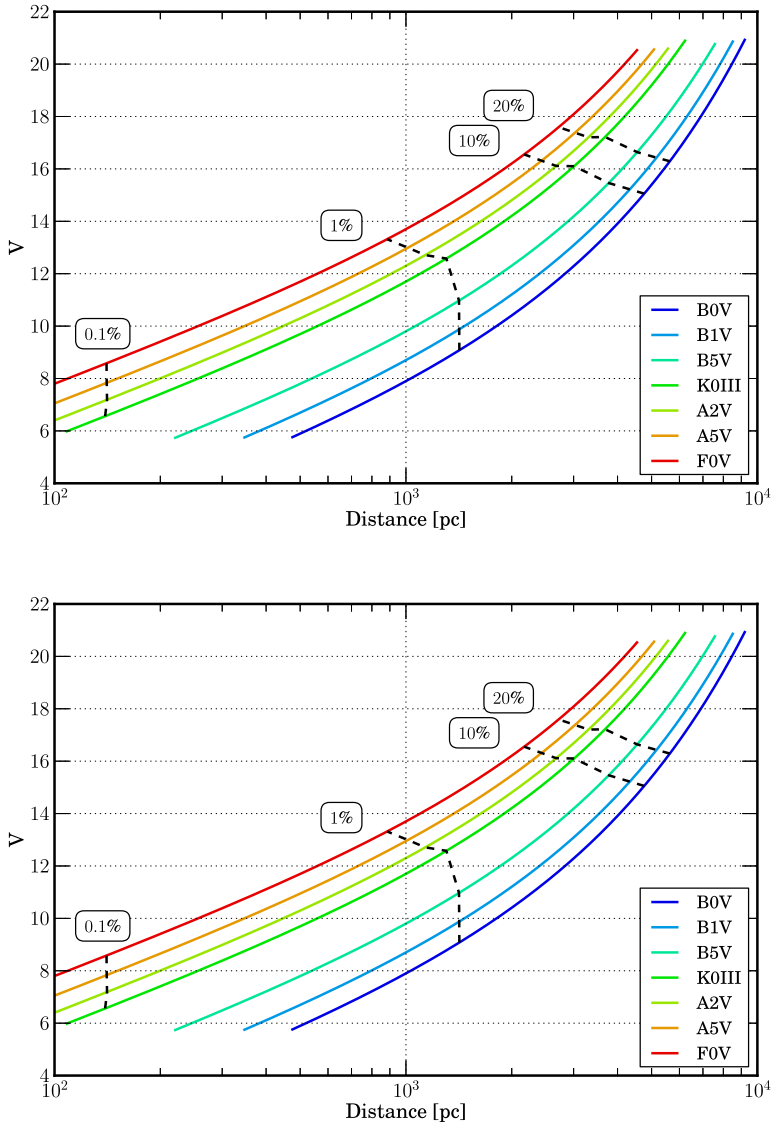

Figure 7.3: The mean parallax accuracy horizons for stars of different spectral types which include our three tracer populations. In the right hand panel we present the pre-launch error estimates and in the left panel we show the performance after commissioning phase where the unexpected effect of stay light of the Gaia is taken in to account. The plot of visual apparent magnitude versus heliocentric distance is done assuming an extinction of 1 magnitude per 1 kpc. Dashed lines represents the constant line of mean relative parallax accuracy. Note that the lines of fixed relative error for stars brighter than $V \sim 12$ are almost vertical due to the Gaia observing strategy (gates are introduced to avoid saturation).

errors and only considering stars with relative error in parallax smaller than 20% ($\Delta\varpi/\varpi < 0.2$). Here we can again see that with A stars we get the least sky coverage and we can catch just the beginning of the warp. With RC stars we can go deeper and reach to $\sim$ 15 kpc towards anti-centre. OB stars although being less numerous, are bright enough to be observed with this high quality parallaxes at larger distances and the warped shape of the disc can easily be seen in the Y-Z projection. More discussion on detecting the warp with samples affected by Gaia errors will later be presented in the next sections.

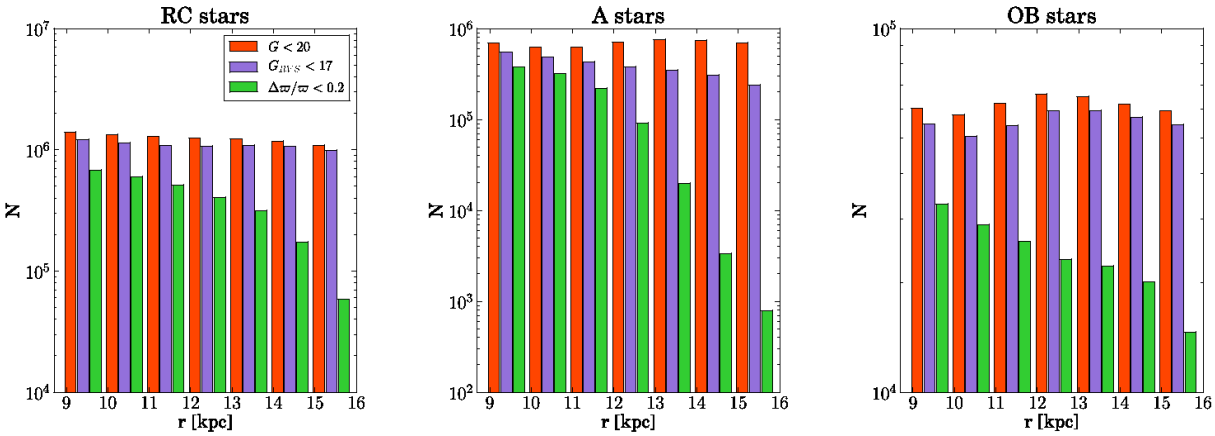

Figure 7.4: Histograms of the number of stars in Galactocentric radius bins of 1 kpc. The samples with $G < 20$, $G_{RVS} < 17$ and $\Delta\varpi/\varpi < 0.2$ are shown respectively in red, purple and green. The histograms are plotted for RC stars (left panel), A stars (middle) and OB stars (right). Notice the change in vertical scale.

7.3 Results from GC3 methods

The methods proposed in Chap. 6 have been applied to three type of simulated samples: 1) *The Perfect samples*, which contain every single generated star in our simulated and relaxed warp model, as described in Chap. 4, that is without any observational constrain; 2) *The Magnitude Limited samples*, including the effect of observational errors and interstellar extinction. Considering all stars up to the Gaia limiting magnitude of $G = 20$ for the GC3 and nGC3 methods, which only require positional information and proper motions respectively, and up to magnitude $G_{RVS} = 17$ for mGC3, which requires the use of radial velocity information (see Sec. 6.2); and 3) *The Clean samples*, including only stars with relative error in parallax smaller than 20% in addition to the previous observational constrains. We apply the GC3, mGC3 and nGC3 methods to the RC, A and OB star samples. We split the samples in Galactocentric radial bins from 9 to 16 kpc, with a width of 1 kpc, and compute the position of the peak in the resulting

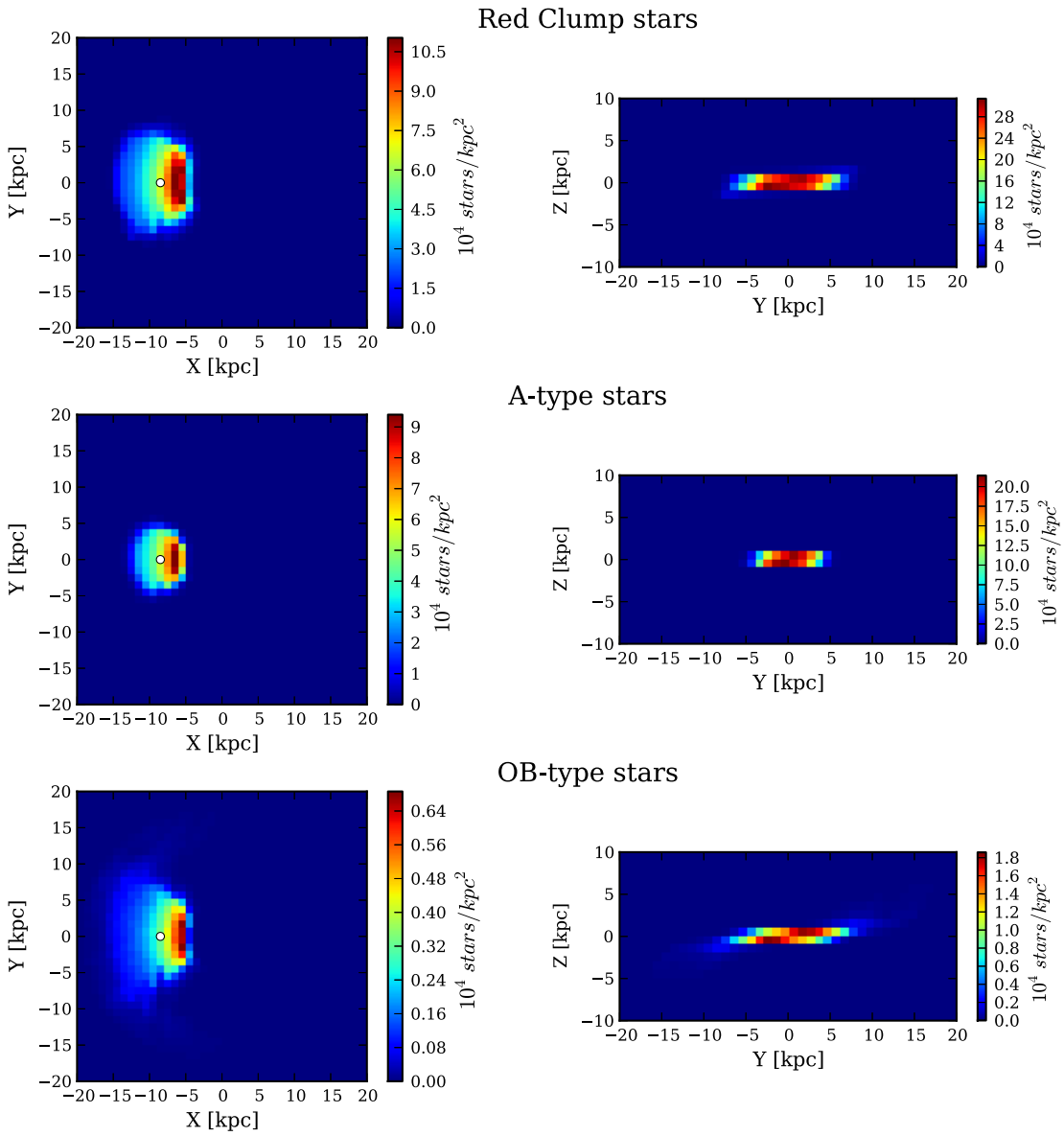

Figure 7.5: Same as Fig. 7.2, but only stars with $\Delta\varpi/\varpi < 0.2$ are considered.

pole counts maps using the procedure described in Sec. 6.3. The values obtained for the tilt and twist angle are compared to the model predictions, discussing, in all cases, the accuracy we can reach and the systematic trends present in the analysis. Note that for the case of Perfect sample we use true distances for splitting stars into radial bins whereas for the Magnitude Limited and Clean samples we use the observed distances for that. In Sec. 7.3.1 we show the results for the samples warped with the UWF model, that we consider our *fiducial model*, together with the results using the UWH model. Results for the twisted warp models (TW1 and TW2) where we used only the OB Clean sample are presented in Sec. 7.3.2.

7.3.1 Results for the untwisted warp model

The Perfect samples

The bottom and top panels in Figure 7.6 show respectively the tilt ψ and twist ϕ angles as a function of Galactocentric (spherical) radius r, for the Perfect sample of RC (*left*), A (*centre*) and OB stars (*right*). The results are shown in comparison with the model prediction (solid black line). The filled red, blue and yellow points show the results obtained for the position of the peak obtained respectively from mGC3, nGC3 and GC3 pole count maps. As the plots show, the recovery of both the tilt and twist angles for these Perfect samples is flawless, with all three methods. This results were to be expected since these samples are error-free and are not affected by a selection function. Nevertheless this is not a trivial test, since we are comparing the recovered distribution of relaxed particles with the tilt and twist angles used to warp the potential. These results verify that the resulting distribution of relaxed particles follows a warp with the same $\psi(r)$ and $\phi(r)$, as those used to warp the potential.

The Magnitude Limited samples

We now apply the same procedure to the Magnitude Limited samples that includes the effects of the Gaia selection function, errors and interstellar extinction (see Sections 7.2.1-7.2.2). Figure 7.7 top panels, show that the null twist angle is recovered for all tracers, using all three methods. We observe very small deviations of typically less than $\sim 1^\circ$, except for the 10.5 kpc bin for which the difference with the model is slightly higher (smaller than $\sim 2^\circ$), yet less significant as we are close to the pole. The recovery of the tilt angle (Figure 7.7 bottom panels) shows a more complex behaviour which, as expected, depends both on the tracer and the method selected. Two important factors come into play producing the observed behaviour: the effect of sample biases introduced by parallax errors when the samples are binned in the observed galactocentric radii and the intrinsic velocity dispersion of the tracer population.

The effect of the intrinsic velocity dispersion is readily observed when comparing results from different tracer populations. Figure 7.7 shows that the recovery of the tilt angle is best for OB stars and less good for A and RC stars. This behaviour is natural since OB stars, although few,

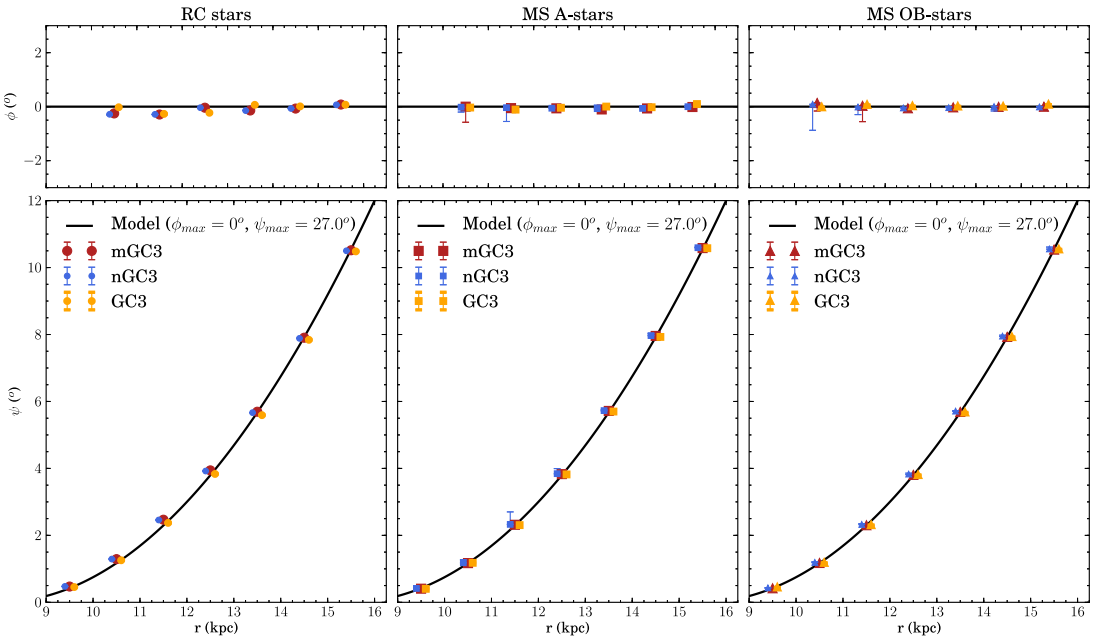

Figure 7.6: Tilt ψ and twist ϕ angles versus Galactocentric (spherical) radius r for the Perfect sample (i.e. without errors or selection function). The black solid line shows the warp model values and coloured points indicate the results obtained from the mGC3 (*red*), nGC3 (*blue*) and GC3 (*yellow*) pole count maps. In this plot, the points corresponding to nGC3 and GC3 have been shifted slightly in the horizontal direction to keep them from fully overlapping. Error bars are plotted, however for most cases, these are smaller than the plotting symbols. In the top panels, the point corresponding to the nearest bin (centred at $r = 9.5$ kpc) has been omitted since for such a small expected tilt angle, the maximum counts signature is expected to lie almost exactly on the pole ($\theta = 90°$), where the azimuth (twist angle) is meaningless.

are a very kinematically cold sample and therefore, have a much smaller scale height, and so, a smaller dispersion around the mid-plane of the warped disc. The A and RC star samples are more numerous, but have increasingly higher velocity dispersions and are, therefore, scattered farther from the mid-plane of the warped disc. It is the combination of this different scale height of each population with the errors in distances in the line of sight direction that produce the observed biases.

To better understand these effects, we will now concentrate on a single tracer. Let us focus on A stars, which being the least luminous on average, have higher parallax errors (see Figure 7.3). We can see that all three methods follow a common trend in which the tilt angle is overestimated up to a certain distance ($r \sim 14$ kpc for A stars) and then it is underestimated for larger distances. This trend is caused by two different sample biases, which act in opposite ways and dominate at different distance ranges. Figure 7.8 illustrates this for A stars with *observed* Galactocentric distances in the ranges $11 < r_{obs} < 12$ kpc (left panel) and $15 < r_{obs} < 16$ kpc (right panel). The plots show the *true* spatial distribution of these stars in the X-Y plane, i.e. as seen pole-on from the North Galactic Pole, with a colour scale proportional to the logarithm of the number density. Note that, due to the small errors at short heliocentric distances, we do not have any stars with true distances close to the Sun reaching the mentioned observed rings.

In the left panel it is clearly seen that the majority of the contamination comes from outside the selected r_{obs}, i.e. from *larger distances* with *higher* tilt angles, thus biasing the mean observed tilt angle towards *higher* values. This is a well known bias caused by the combination of two effects. On one hand, the decrease of radial surface density as a function of Galactocentric distances causes having more stars in the inner than in the outer rings. On the other hand, moving to larger Galactocentric rings, larger volumes are covered. It is the combination of these two effects that makes the number of stars outside our distance bin much larger than the number of stars inside. These effects make it more likely for contaminants at larger distances to be scattered into the r_{obs} bin (See red histogram in Figure 7.4). In the right panel the opposite effect is observed. The majority of the contamination now comes from *smaller distances* where the tilt angle is *smaller*, which in turns biases the mean observed tilt angle towards *lower* values. This effect is observed for bins at distances large enough that there are few more distant stars left due to the survey's magnitude limit, and so it is more likely that stars from inner regions are scattered out to the r_{obs} bin, as a consequence of the skewed distribution in distances that results from the computation from the reciprocal of the parallax (see Brown et al. 2005, for a detailed discussion).

The combination of these effects is what gives rise to the systematic trends observed in Figure 7.7, which affects GC3 results more dramatically causing it to systematically overestimate the tilt angle by $\sim 2^\circ$ for most distances in the RC and A star samples. Although the mGC3 and nGC3 results are affected as well, Figure 7.7 shows the key role played by the use of kinematical information for the recovery of the tilt angle using these methods is far less biased than with the purely position GC3. This comes from the fact that, although stars at different (true) distances

are scattered into a particular observed distance bin, their kinematics are not consistent with the one corresponding to the position where they are observed. The mGC3 and nGC3 velocity criteria naturally prevent these contaminant stars from contributing to a biased tilt angle.

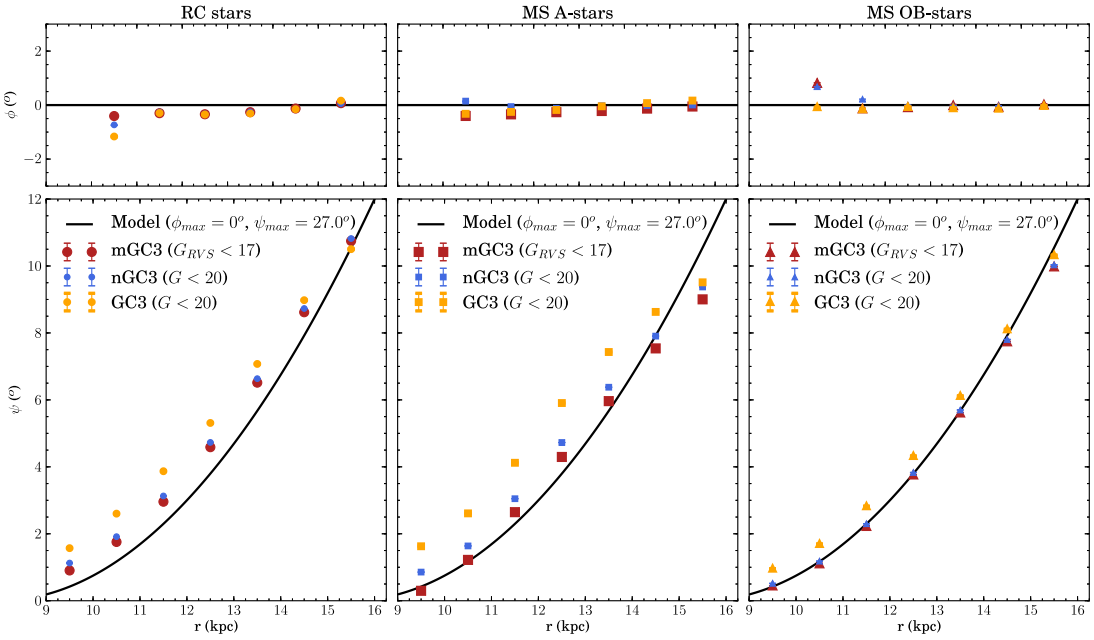

Figure 7.7: Tilt ψ and twist ϕ angles versus Galactocentric (spherical) radius r for the Magnitude Limited samples ($G < 20$ for GC3 and nGC3, and $G_{RVS} < 17$ for mGC3, see Sec. 6.2).

We also explored the recovery of the parameters of the warp model for a case where the warp amplitude is significantly reduced ($\psi_{max} = 13.5°$, UWH warp model) using a Magnitude Limited OB star sample. Results are presented in Figure 7.9. The twist angle recovery is again very good and for the tilt angle, the behaviour is similar as that observed for this sample using our fiducial model (Figure 7.7, right panels). The best results for recovering the tilt angle are again obtained with mGC3.

The Clean samples

We now consider the *Clean sample* that include only stars with parallax errors smaller than 20%. Results are presented in Figure 7.10. We see that the recovery of the tilt angle is again excellent when using OB stars. Results for RC and A stars are accurate for distances up to $\sim$ 15 kpc and $\sim$ 13 kpc, respectively. The kinematical methods mGC3 and nGC3 again give the better results at all distances. The trends and biases explained before are still present, but their effect for the RC stars is reduced because the magnitude of the errors is now smaller and with these being so numerous, sample size is not significantly compromised by the parallax error cut. This is not

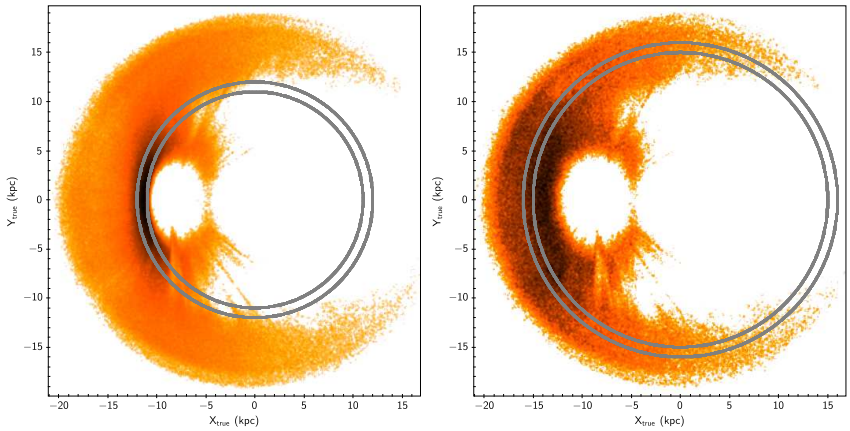

Figure 7.8: Plot of the *true* spatial distribution in the X-Y plane, for the Magnitude Limited sample of A stars in the *observed* (Galactocentric) distance ranges $11 < r_{obs} < 12$ kpc (*left*) and $15 < r_{obs} < 16$ kpc (*right*). The solid gray lines indicate the higher and lower limits of the observed distance range. The Sun is located at (-8.5 kpc,0.) and the Galactic Center is in the origin. The colour scale is proportional to the logarithm of the number density, with dark colours indicating higher densities and light-orange shades indicating lower densities.

the case, however, for the A star sample which is significantly reduced by the parallax cut (see green histograms in Figure 7.4), for which the skewed distance bias starts dominating at shorter distances around $r \sim 13$ kpc.

Ideally one would like to have a criterion that would allow us to identify at which distance the results from the Clean sample start being significantly affected by this bias. For mGC3 and nGC3 we propose that this criterion can be defined empirically, looking at the number of stars in each observed distance bin for the Clean samples shown in Figure 7.11 . This Figure shows that the distance for which the number of stars has decreased down to $\lesssim 10\%$ of the total stars in the innermost bin ($9 < r_{obs} < 10$ kpc), roughly coincides with the distance at which the bias in the tilt angle starts to dominate. *Therefore, we can use this criterion as a rule of thumb to identify the distance up to which results from nGC3 and mGC3 methods can be trusted.* Applying it to the Clean sample results shown in Figure 7.10, we can see that A stars at $r_{obs} > 13$ kpc and RC stars at $r_{obs} > 15$ kpc should be discarded.

7.3.2 Results for a "twisted warp" sample

In this section we apply the same procedure to the Clean sample of OB stars, but now using two warp models *including* twisting and with the same warp amplitude as our fiducial model (see Sec. 3.5). Figure 7.12 shows the results for two different models: TW1 ($\phi_{max} = 20°$) (*left* panels) and TW2 ($\phi_{max} = 60°$) (*right* panels). The performance of all three methods is very

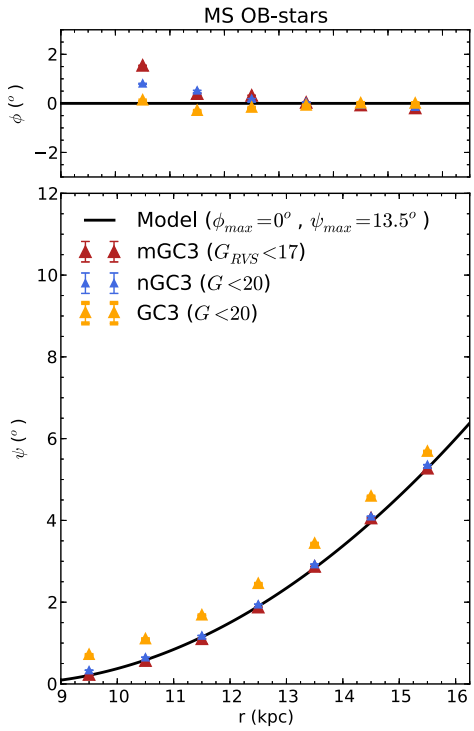

Figure 7.9: Tilt ψ and twist ϕ angles versus r for the Magnitude Limited sample of OB stars warped with UWH model.

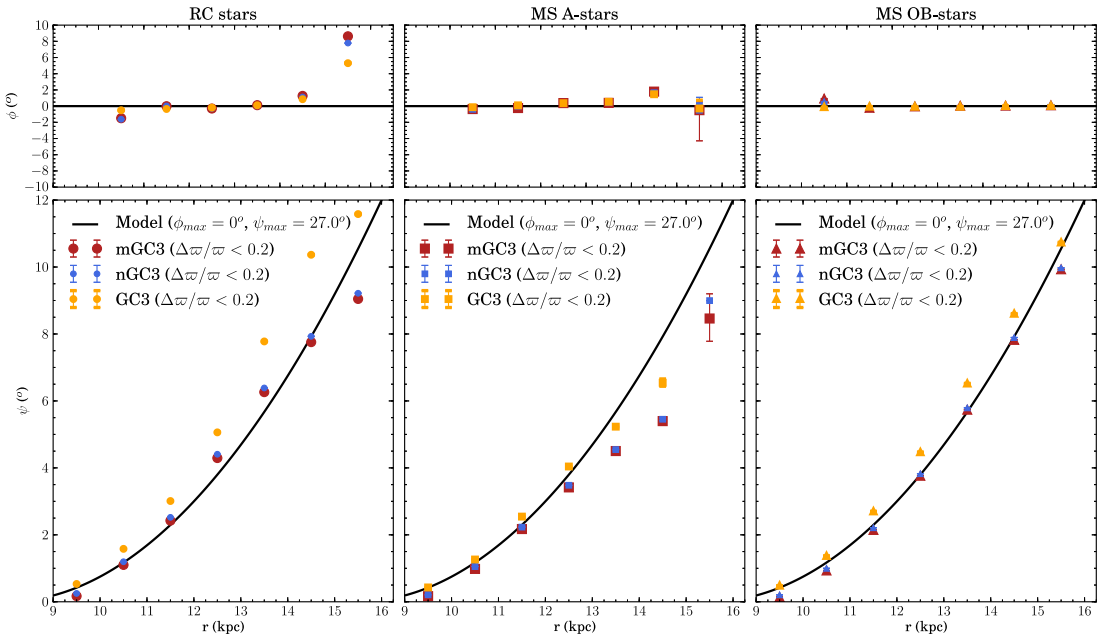

Figure 7.10: Tilt ψ and twist ϕ angles versus Galactocentric (spherical) radius r for the Clean sample ($\Delta\varpi/\varpi < 0.2$).

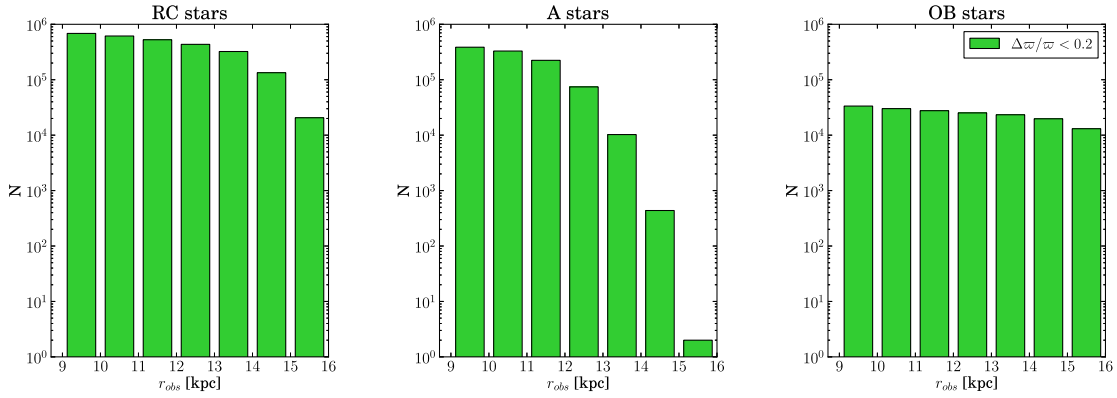

Figure 7.11: Histograms of the number of stars in *observed* Galactocentric (spherical) radius bins of 1 kpc for the Clean samples ($\Delta\varpi/\varpi < 0.2$) of RC stars (*left*) A stars (*middle*) and OB stars (*right*).

good. The twist angle is recovered to within $< 2°$, for nearly all distances, with the largest deviation still being no more than $\sim 3°$.

For the twist angle, we must consider that a given deviation becomes less significative as the tilt angle diminishes: Since meridian lines in a polar grid converge toward the poles, close to them (in our case, small tilt angles), a given difference in twist angle translates into ever smaller angular deviations in the pole count maps (inversely proportional to the sine of the tilt angle). This is shown in the upper right panel of Figure 7.12, where the shaded band represents a $\pm 0.1°$ variation in angular deviation with respect to the model. Note that this is not the same as a $\pm 0.1°$ variation in twist angle. Thus, the error in the recovered twist angle seen for the RC sample in the outermost bin in Figure 7.10, is more significative than any of those seen in Figure 7.12, which turns out to be very small in terms of actual angular deviation.

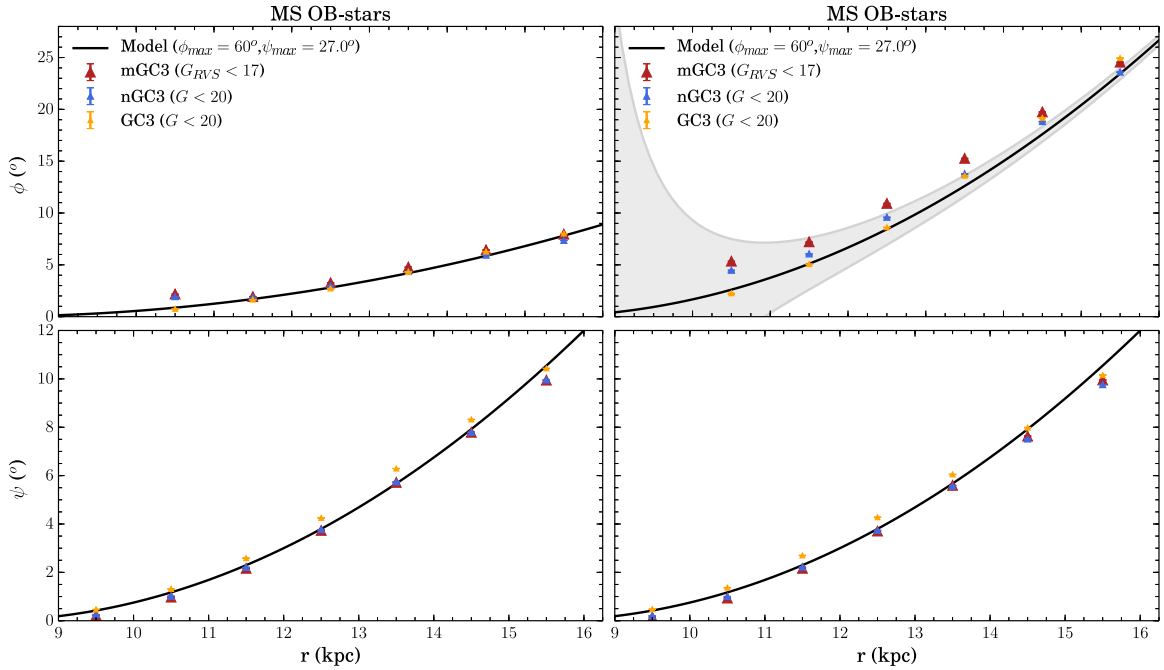

Figure 7.12: Tilt ψ and twist ϕ angles versus r for the Clean sample of OB stars, for two different twist models: TW1 (*left*) and TW2 (*right*). The shaded region in the upper right panel represents a difference in twist angle (azimuthal coordinate) corresponding to an angular discrepancy of $\pm 0.1°$ with the model (see text).

7.4 Results from LonKin method

In figure 7.13 we present the results of LonKin1 and LonKin2 methods for RC stars after applying the Gaia selection function and Gaia errors. As described in Sec. 5.2 and 5.3, these methods are basically the trend of W velocity component and the μ_b proper motion as a function of galactic longitude. Here we see a similar trend to the one using the data for the whole Galaxy without errors in Fig. 5.3 and 5.5 bottom panels. Considering the galactocentric radial bins, we cover the far side of the Galaxy as well which corresponds to the longitudes towards the galactic centre. Due to the high dust extinction in the Galactic centre, Gaia can not observe many RC stars at the far side of the Galaxy towards the direction of $l < 50^\circ$ and $l > 350^\circ$. Therefore the obtained trend towards the mentioned directions can not be trusted. However, for $50^\circ < l < 350^\circ$, the difference between real and observed W velocity component is always less than 5 km/s for RC stars.

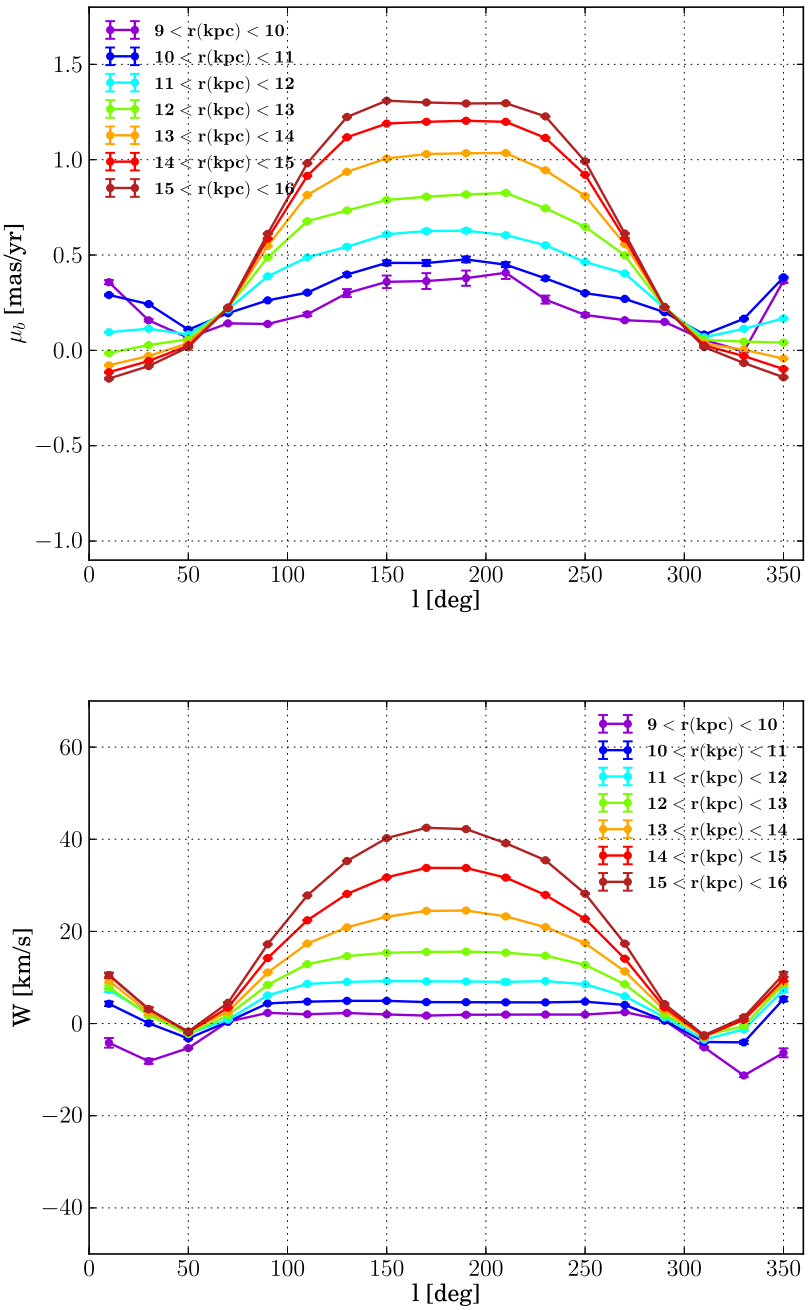

Figure 7.13: Results for the warped RC stars sample affected by Gaia selection function and Gaia errors. The median μ_b vs. Galactic longitude is shown in the top panel and the W velocity component vs. longitude is presented in the bottom panel. The error bars show the standard error of the median. Note that the proper motions are corrected for the vertical velocity of the Sun.

8

Can UCAC4 proper motions help us to detect/characterize the galactic warp?

In this chapter we present our study on looking for the kinematic signature of the warp using the UCAC4 proper motion catalogue (Zacharias et al. 2013). Using the provided 2MASS photometric magnitudes, we choose red clump stars and we compare their trend in the galactic proper motion, μ_b, vs. galactic longitude plane with the one from our warp simulations (obtained in part II of this thesis). Important discrepancies between the two trends can be seen. We discuss the possible sources causing this discrepancy in terms of residual spin of the reference frame with respect to the extra-galactic inertial one.

8.1 UCAC4

The fourth United States Naval Observatory (USNO) CCD Astrograph Catalogue, UCAC4, was released in August 2012 (Zacharias et al. 2013). It is an all-sky astrometric catalogue that contains over 113 million objects which is complete to about magnitude $\sim$ 16 in the Johnson R magnitude. More than 105 million of them have proper motions. The positions and proper motions are measured on the International Celestial Reference System at a mean epoch 2000 (J2000.0). It is also cross-matched with the Two Micron All-Sky Survey (2MASS) and contains J, H and K magnitudes for about 110 million stars. Moreover, it is supplemented by the AAVSO Photometric All-Sky Survey (APASS), which contains five-band photometry (B, V, g, r, i) for over 51 million stars. Most stars have formal position errors of about 15-100 mas per coordinate

at the mean epoch, depending on magnitude, while the formal errors in proper motions range from about 1 to 10 mas yr^{-1} depending on magnitude and observing history. Systematic errors in the proper motions are estimated to be about 1-4 mas yr^{-1} (Zacharias et al. 2013).

8.2 The kinematic tracer: the red clump stars

8.2.1 Selection criteria

We select the red clump (RC) stars using the K versus $J-K$ colour-magnitude diagrams. Near-infrared colour-magnitude diagrams are very suitable for selecting the RC stars because they have a clear separation from the dwarf population up to magnitude $K \lesssim 13$ (López-Corredoira et al. 2002). We followed the method proposed by López-Corredoira et al. (2002) to choose the RC stars in the UCAC4 catalogue. Here we provide a summary of this method. The position of a star on an observed color-magnitude diagram is determined from its absolute magnitude, intrinsic color, distance and extinction. Assuming that we know precisely the intrinsic color of a star, any shift in color is caused by extinction. Whereas a shift in absolute magnitude can be due to both distance and extinction. Assuming the RC stars has low intrinsic dispersion in both intrinsic color and absolute magnitude (see e.g. Bovy et al. 2014), they populate a narrow line (or stripe) in the color-magnitude diagram for a given line-of-sight direction. Using the Drimmel extinction map which provides the extinction in different lines of sight as a function of heliocentric distances, we determine this line for different regions in the Galaxy (using a code provided by S. Ribas, private communication). In order to illustrate this better, in Fig. 8.1 we plot the color-magnitude diagram of the UCAC4 stars in a randomly selected region, the mentioned line is plotted in blue.

We divide the sky into 3072 regions according to the galactic longitude and latitude (proposed by S. Ribas, private communication) as follows:

- For $|b| < 0.5^\circ$, regions of $1^\circ \times 1^\circ$ are considered.
- For $0.5^\circ < |b| < 2^\circ$, regions of $1.5^\circ \times 1.5^\circ$ are considered.
- For $2^\circ < |b| < 10^\circ$, regions of $2^\circ \times 2^\circ$ are considered.
- For $10^\circ < |b| < 20^\circ$, regions of $5^\circ \times 5^\circ$ are considered.
- For $|b| > 20^\circ$, regions of $10^\circ \times 10^\circ$ are considered.

Since the stellar density drops as moving to higher latitudes, the bin size is increased both in longitude and latitude as moving away from the galactic disc so that we can capture a reasonable amount of stars in each bin. The RC trace in the K vs $(J-K)$ plane is calculated in each region using the Drimmel extinction model, and the UCAC4 stars which lie on this trace with

a tolerance of $\Delta|J-K| < 0.1$ (as proposed by Cabrera-Lavers et al. 2007) are selected as the RC sample. The absolute magnitude and intrinsic colour of this population are assumed to be: $M_K = -1.62$, $(J-K)_0 = 0.61$ (Alves 2000). The Drimmel extinction map provides the visual extinction (A_V), in order to obtain the extinction in the K band, we use the extinction law from Cardelli, Clayton & Mathis (1989) which gives us: $A_K = 0.114\,A_V$. Knowing the extinction, A_K, and the apparent and absolute magnitude, the IR photometric distances can be easily calculated (in parsecs):

$$r = 10^{\frac{K - M_K + 5 - A_K}{5}} \tag{8.1}$$

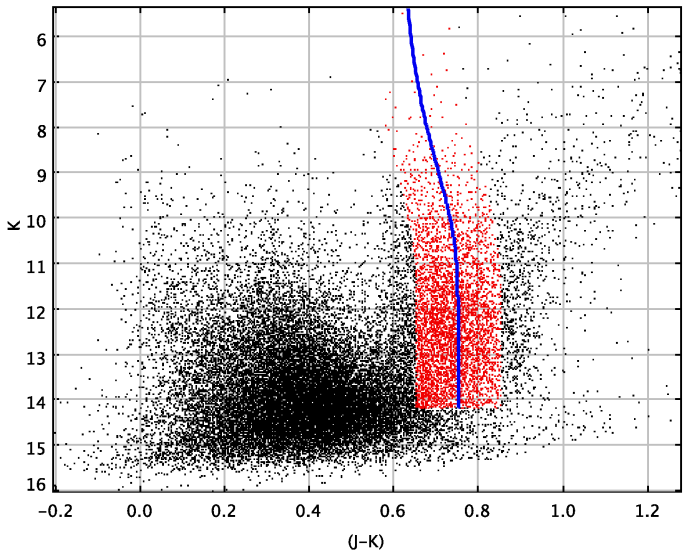

Figure 8.1: The color-magnitude diagram of all UCAC4 stars in the direction of $(l, b) = (229°, 3°)$ in black, in blue we plot the trace of the RCs and in red are the selected RCs.

Using this method, we obtain about 22 million RCs in the UCAC4 catalogue. Considering the limiting magnitude of this catalogue, this number suggests a high contamination of non-RCs. The distribution of this RC sample in galactic longitude is shown in Fig. 8.3 in red.

8.2.2 Contamination

Ribas (private communication) estimated the contamination of dwarfs as a function of galactic latitude. Following the RC selection strategy described in Sec.8.2.1, the contamination was estimated by simulating the main sequence and giant stars of spectral types G, K and M using the Besançon Galaxy Model (Robin et al. 2003). The main conclusion was that the dwarf contamination increases with latitude (as seen in Fig. 8.2), and the limiting K magnitude for

which the dwarf contamination is less than 10% as a function of galactic latitude, follows this polynomial fit:

$$K_{lim} = 13.2 - 0.18633b + 0.0018793\ b^2 + 4.0633 \times 10^{-6}\ b^3 - 9.3798 \times 10^{-8}\ b^4 \qquad (8.2)$$

where b is the galactic latitude in degrees. For stars fainter than K_{lim}, the dwarf contamination exceed 10%, while it should be lower for brighter stars. Hence to reduce the dwarf contamination of our sample, we perform a magnitude cut for stars fainter than K_{lim} following Eq. 8.2. The increase of dwarf contamination as a function of latitude was also seen using the data of RAdial Velocity Experiment (RAVE) (see Fig. 6 of Zasowski et al. 2013). Note that when selecting the RC stars, we can have contamination not only from dwarfs but also from other types of giant stars such as M giants, asymptotic giant branch and the red giant branch bump (RGBB). As discussed by López-Corredoira (2014), the RGBBs in particular can contaminate the selected RC stars the most. He derived a contamination of RGBBs of $\lesssim 10\%$. Considering these two sources (dwarfs and RGBBs), we consider that, in the worst case, we have a non-RC contamination of $\sim 20\%$ in this sample. As we will see in next sections, this contamination has an important influence on our kinematic analysis. However, this contamination is unavoidable when using selecting RC stars photometrically.

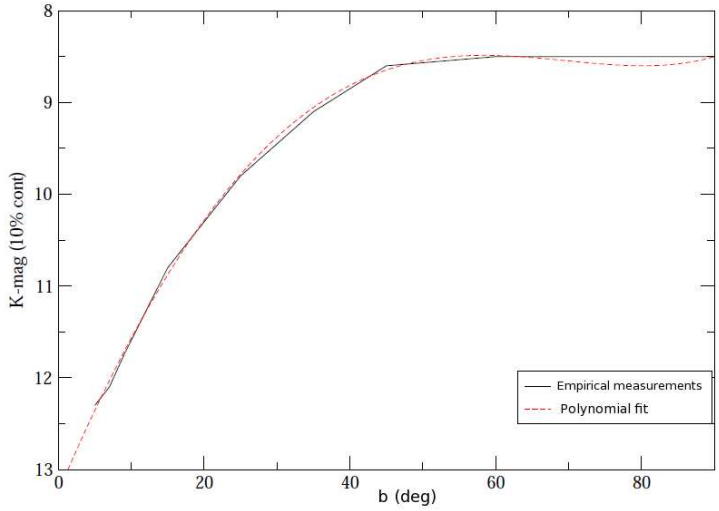

Figure 8.2: The limiting K magnitude for which the dwarf contamination is less than 10% as a function of galactic latitude (S. Ribas, private communication). This plot was obtained using the Besançon Galaxy Model (Robin et al. 2003).

After applying the K_{lim} magnitude cut, we also discard all of the stars with $|z| > 1.5$ kpc in order to avoid halo stars. Moreover, we remove stars with object type flag (a flag introduced in UCAC4 catalogue) unequal to zero indicating that there were problems observing the star.

After applying these cuts, we reduce the number of our RC sample to about 10 million, which we will refer to as the *UCAC4-RC-ref* sample. The distribution of this sample in galactic longitude is presented in Fig. 8.3 in blue. From this sample we are only interested in stars with spherical galactocentric radius $\in [9, 15]$ kpc which are the ones that are partaking in the galactic warp. We will call this sample hereafter as *UCAC4-RC-ref-*r_{limit}. In Fig. 8.3 its distribution in longitude is presented with green histograms.

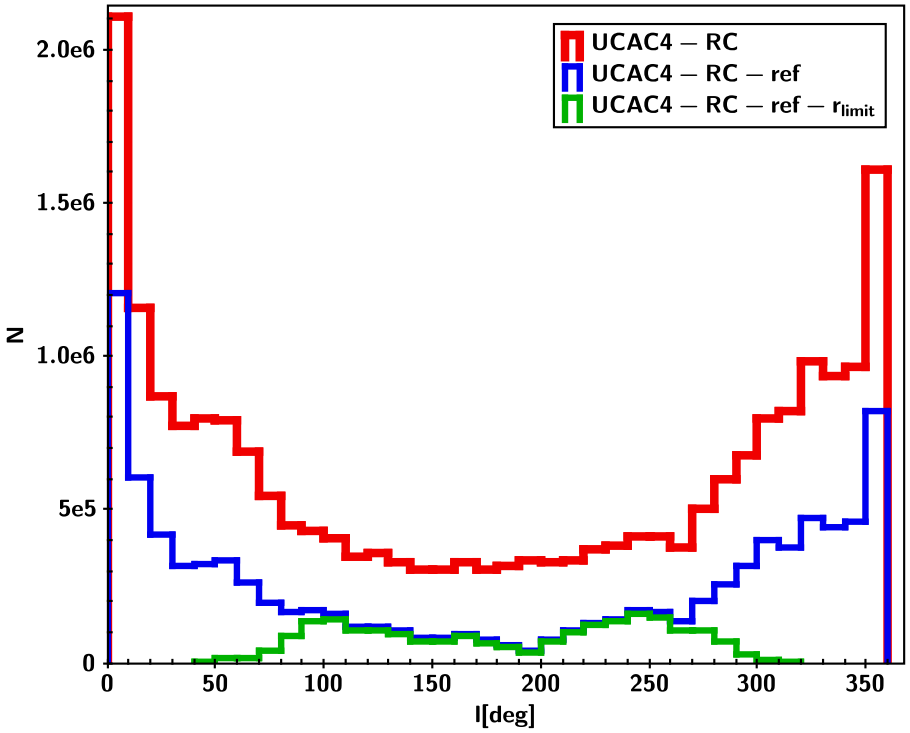

Figure 8.3: Histograms of the number of the red clump stars as a function of galactic longitude for three samples: UCAC4-RC (in red) which consists of all 22 million selected RCs as described in Sec.8.2.1; UCAC4-RC-ref (in blue) which is the refined sample (with lower non-RC contamination) of about 10 million RC stars as discussed in Sec. 8.2.2; and UCAC4-RC-ref-r_{limit} (in green) which is similar to UCAC4-RC-ref but only stars partaking in the warp are considered (stars with spherical galactocentric radius $\in [9, 15]$ kpc).

8.3 Results from the LonKin2 method

As mentioned in Sec. 5.3, the kinematic signature of the warp in the space of observables, can be obtained by looking at the μ_b proper motion trend in different directions in the galactic plane. We generate a sample of RC stars warped with our UWF model (as explained in part II of this thesis), where the warp is generated adiabatically and has a straight line of nodes, and only consider stars with G magnitude brighter than 16, which approximately resembles the magnitude limit of UCAC4. We do not convolve this sample by any kind of observational errors. We call this sample hereafter *simul-RC-G16*. In Fig. 8.4 we plot the median μ_b proper motions of this sample in bins of 20 degrees in galactic longitude. As discussed before in Sec. 5.3, the μ_b proper motions are referred to the LSR that are corrected for the here imposed motion of the Sun. Stars within galactocentric spherical radius $\in [9, 15]$ kpc, where the warp takes place, are divided into bins of 1 kpc. The error bars are the standard error of the median which are calculated for a 95% confidence level (as described in Sec. 5.2). We can see a positive maximum peak towards the galactic anti-centre whose amplitude increases as we move to larger galactocentric radii. Note that the magnitude limit of G$\leqslant$ 16, prevents us cover the range of longitudes towards the galactic centre, for these large galactocentric radii. This can be seen in the distribution of this sample in galactic longitude in Fig. 8.3 in the green, where we do not have any stars towards $l < 40^\circ$ and $l > 320^\circ$.

Now, for the UCAC4-RC-ref-r_{limit} sample, we calculate the μ_b from the μ_α and μ_δ provided in the UCAC4 catalogue. Moreover, the μ_b proper motions are corrected for the motion of the Sun and therefore they are referred to the LSR. And we have the IR distances as described in Sec 8.2.1, following the Eq. 8.1. In order to perform the same analysis using the LonKin2 method on this sample, we should bear in mind that the use of medians instead of means of proper motions are very important here. The dwarf contamination could play an important role if looking at the average proper motions. Because they are closer than the RCs and attributing an incorrect distance to them, would considerably bias the average proper motions. This can be improved by using the median of the proper motions instead of the average (López-Corredoira 2014).

In Fig. 8.5, we plot the results for the UCAC4-RC-ref-r_{limit} sample using medians and surprisingly we see a negative minimum peak towards anti-centre which is in a complete contradiction with what is expected using simul-RC-G16 sample. In this plot, the errorbars show the quadratic summation of the statistical error of median (the 95% confidence level) and the systematic error due to the contamination, following López-Corredoira (2014). As mentioned before, we consider a maximum of 20% contamination in this sample and therefore the limits of the corresponding error bars are given by the $0.5N \pm 0.1N$ ranked values of the ordered set of N data.

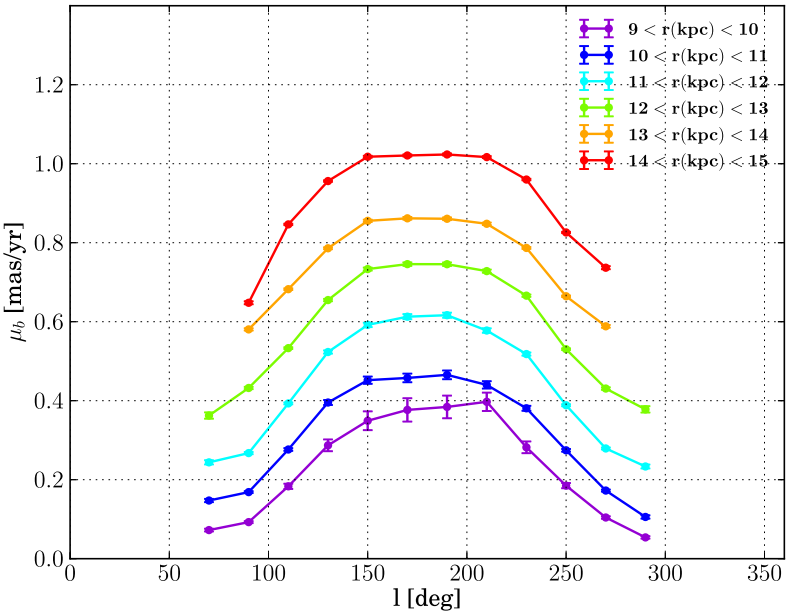

Figure 8.4: The median μ_b (referred to the LSR) as a function of galactic longitude for a sample of *simulated* (with model UWF) RC stars with G $\leqslant$ 16 (the simul-RC-G16 sample). Different colors correspond to different radial bins (in kpc) as indicated in the figure. The error bars show the standard error of the median (the 95% confidence level). Note that in this plot we do not consider any observational errors.

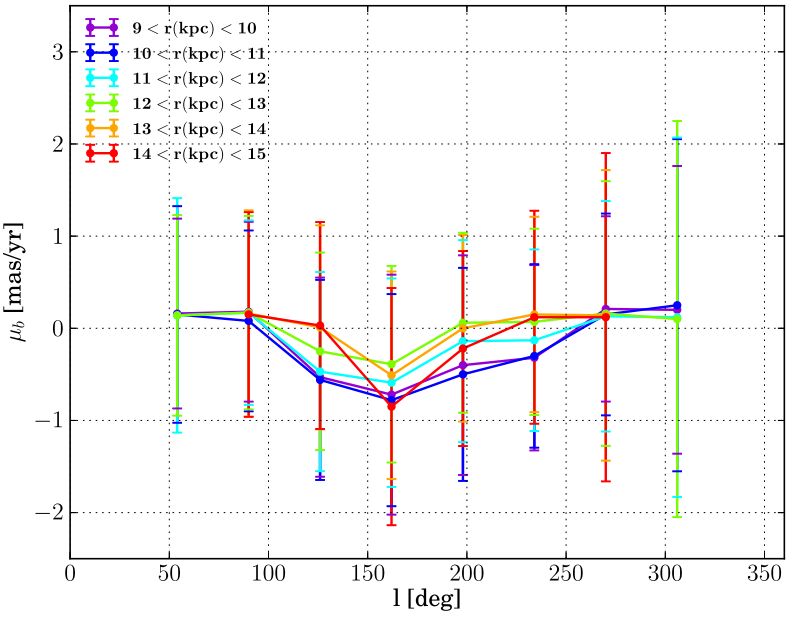

Figure 8.5: The μ_b (referred to the LSR) galactic proper motion as a function of galactic longitude for the UCAC4-RC-ref-r_{limit} sample. Different colors correspond to different radial bins (in kpc) as indicated in the figure. The circles show the median of μ_b in longitude bins of 36°. The errorbars show the statistical error of median (95% confidence level) together with the error due to the contamination with non-RCs.

8.4 Model vs data

We suspect that one of the sources causing this large discrepancy between the μ_b trend in the data and in our model, comes from some systematic errors in the UCAC4 proper motions. Here we propose two possible explanation for this discrepancy. As mentioned in López-Corredoira (2014), such a systematic bias in proper motion catalogues could be partially (or significantly) removed using quasars and external galaxies in the catalogue. Since these objects are supposed to have zero proper motions due to their very large distances, any significant deviation from zero, shows a systematic error in the catalogue. But the UCAC4 catalogue is magnitude limited down to R$\sim$ 16 and only few hundreds of quasars can be observed down to this magnitude which is not enough for obtaining the systematic trend in the whole sky. Nevertheless, in Sec. 8.4.2, we exploit these quasars and try to solve for the systematics.

Another point that we should consider when exploring the source of this discrepancy, is that our warp model may not perfectly mimic the one of the MW. Our UWF warp model is constructed following observational constraints, such as the position of the line of nodes, the approximate amplitude and the shape of the actual MW warp. One of the uncertainties about the MW warp is how adiabatic it has been formed, in other words, was it generated slowly enough so that stars had time to move along with it? or, alternatively has it happened so abruptly that the disc is experiencing a transient phase? In this chapter, we compare the observations with the simul-RC-G16 sample which is generated considering an adiabatic warp growth (see Sec. 4.2). As mentioned in Sec. 4.2, studying an impulsive generated warp will require information on the origin of the warp which is not the aim of our study at this moment.

In order to see how this discrepancy changes with galactocentric radius and galactic longitude, we divide the simul-RC-G16 sample in bins of 10 degrees in galactic longitude and 0.5 kpc in galactocentric radius and calculate the mean μ_b for each sub-sample. Then, we calculate the difference between all UCAC4-RC-ref-r_{limit} stars and the binned model:

$$Y_{ij} = \mu_{b\,UCAC4}(l_{ij}, r_{ij}) - \mu_{b\ model}(l_{bin\,j}, r_{bin\,j}) \tag{8.3}$$

where i refers to each RC star and j refers to the bin in which the ith star locate in terms of galactocentric radius and longitude. We plot Y as a function of radius and longitude as shown in Fig. 8.6. In order to better see the trend, we compute the median and show them in the right hand panels. We can see a clear trend in Y both as a function of radius and longitude. As a function of radius, the median of μ_b of the model is always over-estimated compared to the one of UCAC4 and this difference increases for larger radii. For the dependence in longitude, the model over-estimates the μ_b compared to UCAC4 increasingly with longitude up to the direction of the anti-centre, and for larger longitudes, this difference drops. Note that as seen in bottom left panel, towards $180^\circ < l < 200^\circ$ the numbers of stars drops significantly. This is due to the fact that we removed stars with object type flag unequal to zero (as explained in Sec. 8.2.2) and this cause to loose more stars in this specific region, which can be seen in both blue and green

histograms in Fig. 8.3.

The discrepancy between model and data can be due to one or both of these possibilities: 1) the warp model is not realistic enough and it systematically overestimates / underestimates the real galactic warp as a function of galactocentric radius and galactic longitude, 2) The uncertainties in the values used for the peculiar velocity of the Sun (when correcting for the Solar motion), especially the $W_{\odot}$, 3) The discrepancy may reflect different systematics present in the UCAC4 proper motions. In order to study the later case, in the following section we look into the definition of the reference frame used in UCAC4 and see if there are some uncertainties in specifying that.

8.4.1 The reference frame

The International Astronomical Union (IAU) decided that, from 1998 onwards, the IAU celestial reference system shall be the International Celestial Reference System (ICRS), thus replacing the FK5 system (Fricke et al. 1988). This new reference frame was introduced with the goal of placing positions and proper motions of celestial objects directly on an extra-galactic inertial reference frame. Its origin is located at the barycentre of the solar system. Since it is not associated with the Earth's equator, it does not depend on its nutation and precessional motion. Its practical materialization is called the International Celestial Reference Frame (ICRF) that is realized in the radio frequency bands. The realisation of the ICRS in the optical which is based on the Hipparcos space mission, is named the Hipparcos Celestial Reference Frame (HCRF). The UCAC4 catalogue strictly used the Hipparcos and Tycho-2 reference stars as reference frame and therefore follows the HCRF.

Kovalevsky et al. (1997) explored different observations and methods to link the Hipparcos Catalogue to the extragalactic reference frame. The different approaches were used by several groups to estimate the orientation and spin components of the Hipparcos reference frame with respect to the extragalactic one. The different techniques generally agreed to within 10 mas in the orientation and 1 mas yr^{-1} in the spin components. Finally, the coordinate axes defined by the Hipparcos Catalogue at the epoch 1991.25, were believed to be aligned with the ICRF to within 0.6 mas in the three components of the orientation vector and to within 0.25 mas yr^{-1} in the three components of the spin vector, ω (Kovalevsky et al. 1997). Ten years later, van Leeuwen (2007) studied the new reduction of the Hipparcos catalogue and concluded that the reference frame defined by the new catalogue is identical to the 1997 one.

The spin vector components have been defined as follows: ω_1 towards $\alpha = 0^h$, $\delta = 0°$, ω_2 towards $\alpha = 6^h$, $\delta = 0°$ and ω_3 towards $\delta = 90°$. Some studies reported higher values for the ω_3 component compared to the one of Kovalevsky et al. (1997). Bobylev (2010) presented the results of inertiality of the HCRF by different groups using various catalogues and methods such as NPM1 (Klemola et al. 1994), SPM2 (Zhu 2001), PUL2 (Bobylev et al. 2004), KIEV (Kislyuk et al. 1997), POSTDAM (Hirte et al. 1997), BONN (Geffert et al. 1997), EOP (Vondrak et al.

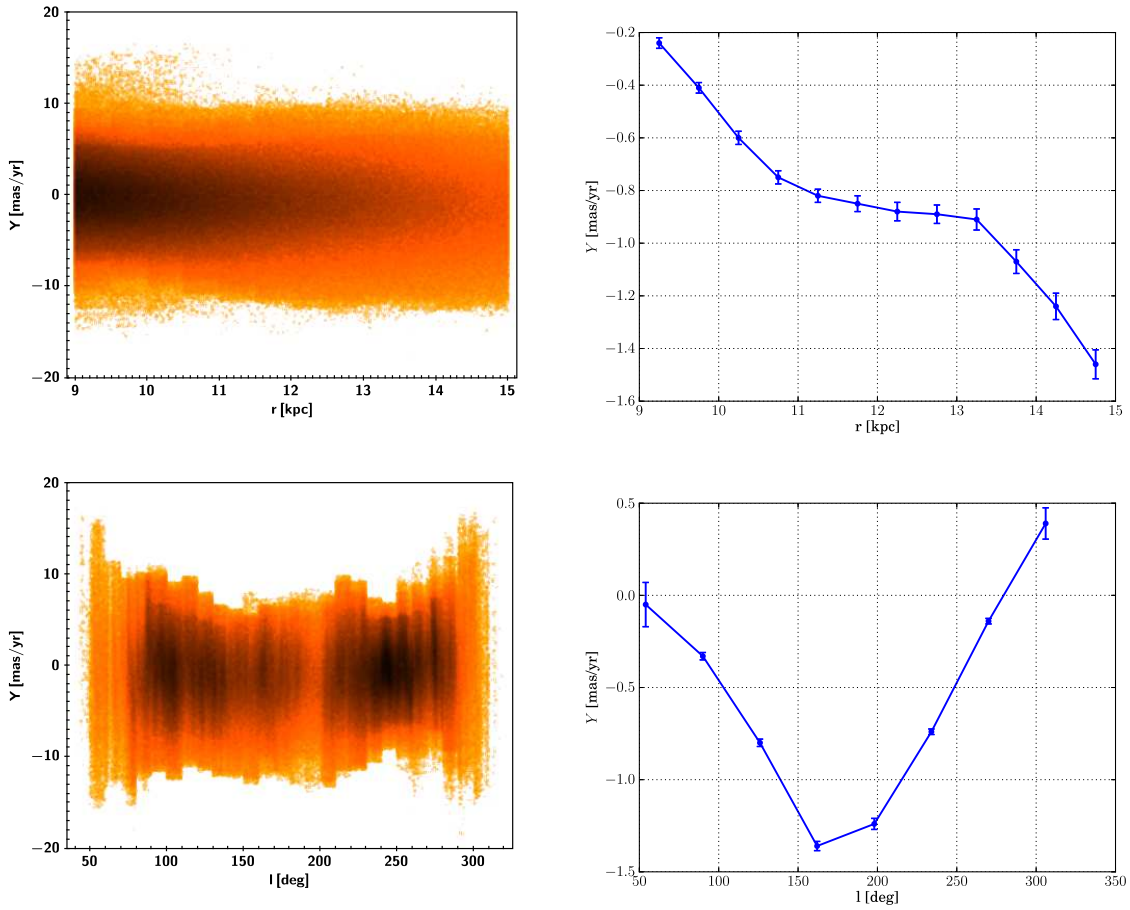

Figure 8.6: The difference between observed and binned model μ_b, $Y_{ij} = \mu_{b\,UCAC4}(l_{ij}, r_{ij}) - \mu_{b\,model}(l_{bin\,j}, r_{bin\,j})$, as a function of galactocentric radius (top panels) and galactic longitude (bottom panels). In order to better see the trend, the medians are computed and shown in the right hand panels. The statistical error bars of the median are calculated for the 95% confidence level. Note that in left panels the colour scale is proportional to the logarithm of the number density, with dark colours showing the high density regions and light-orange shades indicating lower densities. This shows a significant systematic difference between the μ_b of the model and the one of UCAC4 as a function of galactocentric radius and galactic longitude.

1997), XPM (Bobylev et al. 2010), VLBI-07 (Boboltz et al. 2007), among others. In order to estimate the residual spin vector components of the HRCF relative to the extragalactic, inertial reference frame, he considered the weighted mean of the reported spin components from the mentioned solutions and obtained $(\omega_1, \omega_2, \omega_3) = (-0.11, 0.24, -0.52) \pm (0.14, 0.10, 0.16)$ mas yr^{-1}. Fedorov et al. (2011) used the XPM catalogue (Fedorov et al. 2009) to show that the HRCF represented by the Tycho-2, PPMXL, UCAC3 and XC1 catalogues has a significant residual spin vector component of $\omega_3 = -1.8 \pm 0.16$ mas yr^{-1} and negligible values for ω_1 and ω_2.

In order to check how this residual spin of the reference frame can affect the results of the LonKin2 method (as seen in Fig. 8.5), we correct the UCAC4 proper motions according to the spin proposed by Bobylev (2010) and Fedorov et al. (2011). In order to apply the residual spin vector to the UCAC4 proper motions, we use the following equations from Lindegren & Kovalevsky (1995) in equatorial coordinates:

$$\Delta\mu_\alpha \cos\delta = -\omega_1 \cos\alpha \sin\delta - \omega_2 \sin\alpha \sin\delta + \omega_3 \cos\delta \tag{8.4}$$

$$\Delta\mu_\delta = \omega_1 \sin\alpha - \omega_2 \cos\alpha \tag{8.5}$$

The new, transformed proper motions are calculated from the original UCAC4 ones as follows:

$$(\mu_\alpha \cos\delta)_{new} = (\mu_\alpha \cos\delta)_{UCAC4} + \Delta\mu_\alpha \cos\delta \tag{8.6}$$

$$\mu_{\delta\,new} = \mu_{\delta\,UCAC4} + \Delta\mu_\delta \tag{8.7}$$

The top and bottom panels of Fig. 8.7, show the results after applying the residual spin respectively proposed by Bobylev (2010) and Fedorov et al. (2011) to the UCAC4 data presented in Fig. 8.5. In the top panel, we observe an almost flat behaviour and in the bottom we even see a positive maximum trend close to the galactic anti-centre. From the results of LonKin2 method on our warp simulations (see Fig. 8.4), we know that the amplitude of the warp signature should be of the order of 1-2 mas yr^{-1}. Since the reported values for the spin axis components are approximately of the same order, applying each of them, cause the μ_b trend to change significantly. Therefore, it is essential for this study to know a very precise value of the residual spin components. Mignard (2001) showed that the observations of quasars or point-like galactic nuclei by Gaia will allow them to determine the residual spin and put Gaia astrometric solution into the inertial frame. He estimated that with Gaia data we could measure the ω with an accuracy of 0.2 μas yr^{-1}. Considering the new values for the Gaia science performance after the the commissioning phase (ended July 2014), Gaia is expected to determine this residual spin with a precision of 0.4 μas yr^{-1}. Therefore, the uncertainty in the reference frame determination seen here, will be solved by Gaia. Until then, we decide to follow a different approach where we try to infer the residual spin vector with a least square fit as described in the following section.

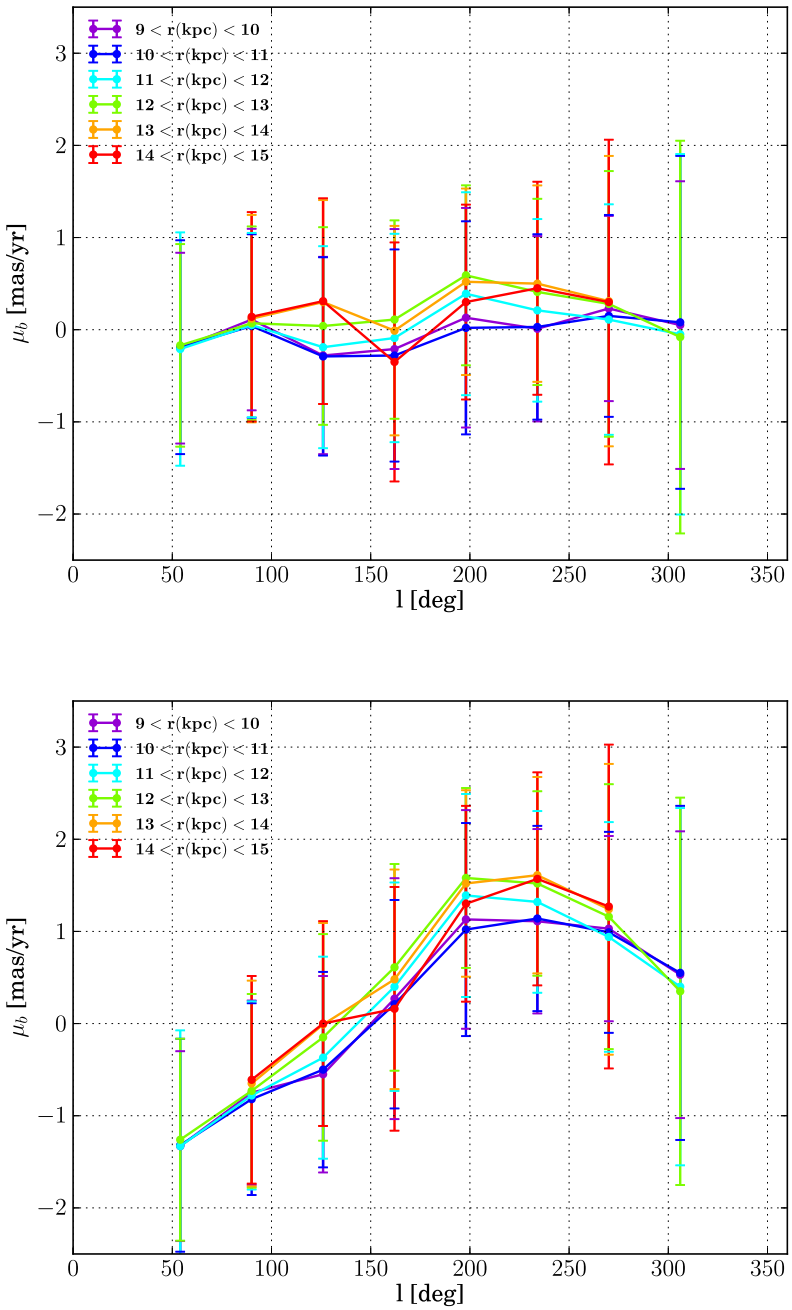

Figure 8.7: Same as Fig. 8.5, after applying correcting for the residual spin vector. Different colors correspond to different radial bins (in kpc) as indicated in the figure. *Top* : using a residual spin vector of $(\omega_1, \omega_2, \omega_3) = (-0.11, 0.24, -0.52)$ mas yr^{-1} following Bobylev (2010). *Bottom*: after applying a residual spin of $(\omega_1, \omega_2, \omega_3) = (0, 0, -1.8)$ mas yr^{-1} following Fedorov et al. (2011).

8.4.2 Inferring the residual spin

Let's assume for now that our warp model is very similar to the real one of the MW. We want to see what should be the values of the residual spin vector components so that the UCAC4-RC-ref-r_{limit} sample give us a same trend as the one of our simulation seen in Fig. 8.4. For this, we use a least squares method. Since the warp amplitude changes with azimuth and galactocentric radius, the μ_b trend also depends on these two parameters. We bin our simulated simul-RC-G16 sample in every 10 degrees in galactic longitude and 0.5 kpc in galactocentric radius and calculate the mean μ_b for each 2D bin. We know that the warp signature can be best observed in galactic proper motion μ_b, therefore, in order to relate the model and UCAC4 proper motions, we should use an equation similar to eq. 8.4 and 8.5, but in galactic coordinates. For that, we have followed equations 2 and 3 from Perryman et al. (2014):

$$\Delta\mu_l \cos(b) = -\omega_{1g}\ \cos(l)\sin(b) - \omega_{2g}\ \sin(l)\sin(b) + \omega_{3g}\ \cos(b) \tag{8.8}$$

$$\Delta\mu_b = \omega_{1g}\ \sin(l) - \omega_{2g}\ \cos(l) \tag{8.9}$$

Where l and b are respectively galactic longitude and latitude and $(\omega_{1g}, \omega_{2g}, \omega_{3g})$ is the spin vector in galactic coordinate where ω_{1g} is towards galactic centre, ω_{2g} is in the direction of galactic rotation and ω_{3g} is towards the North galactic Pole. Note that although the warp depends on the galactocentric azimuth, we binned the simul-RC-G16 sample in longitudes and not in azimuth, this is only because, as seen in the above equations the spin vector components depend on longitudes (not on azimuth). We determine the residual spin components via least squares fit from the following equation:

$$\mu_{b\,UCAC4}(l_i, r_i) - \mu_{b\ model}(l_{bin}, r_{bin}) = \omega_{1g}\ \sin(l_i) - \omega_{2g}\ \cos(l_i) \tag{8.10}$$

where the (l_i, r_i) position of star i is located inside the (l_{bin}, r_{bin}) bin. Note that here we do not consider the Eq. 8.8 in the least squares fit. Because for this equation, we need to consider the motions within the galactic plane and that will be too uncertain. The motion inside the plane is affected by the galactic rotation and the spiral arms and the galactic bar. This will introduce too many free parameters to our model (e.g. the pitch angle and the density of the spiral arms, etc.). In order to avoid this complexity, we only consider Eq. 8.9 which only depends on the vertical motions. As shown in Appendix B , spiral arms could not significantly modify the systematic effect of the galactic warp on the vertical motions. Using an iterative scheme we obtain: $(\omega_1 g, \omega_2 g) = (-0.129, -1.92) \pm (0.009, 0.012)$ mas yr^{-1}. In order to check how this residual spin vector change the results of the LonKin2 method, in Fig. 8.8 top panel, we show the μ_b trend after applying this spin to the UCAC4-RC-ref-r_{limit} sample. We can see that a maximum peak is obtained, but its direction is not towards the anti-centre.

The distribution of the μ_b in UCAC4-RC-ref-r_{limit} sample has very long narrow tails that can reach up to ± 100 mas yr^{-1}. This can be due to the existence of high velocity stars, and/or

Table 8.1: Components of the residual spin vector in equatorial, (ω_1, ω_2, ω_3), and galactic coordinates, (ω_{1g}, ω_{2g}, ω_{3g}), in units of $\mathrm{mas\,yr^{-1}}$. The reported values from the literature are also presented. The LSF refers to the results from our least squares fit. We also present the results from the same method after removing the outliers. σ is the root mean square the least squares fit residuals in $\mathrm{mas\,yr^{-1}}$.

Method/Solution	ω_1	ω_2	ω_3	ω_{1g}	ω_{2g}	ω_{3g}	σ
Bobylev (2010)	-0.11 ± 0.14	0.24 ± 0.10	-0.52 ± 0.16	0.05	-0.55	-0.19	-
Fedorov et al. (2011)	~ 0	~ 0	-1.8 ± 0.16	0.87	-1.34	-0.82	-
LSF	-	-	-	-0.129 ± 0.009	-1.92 ± 0.012	-	10.6
LSF, outliers removed	-	-	-	-0.09 ± 0.003	-1.55 ± 0.005	-	3.96

stars with unknown large observational errors. These outliers can bias the results and therefore should be removed from the UCAC4-RC-ref-r_{limit} sample. we restrict the sample to the stars in the higher 80th percentile of the μ_b distribution in each of the 2D bins and then apply the least squares fit. This way, we obtain $(\omega_1 g, \omega_2 g) = (-0.09, 1.55) \pm (0.003, 0.005)$ $\mathrm{mas\,yr^{-1}}$. In figure 8.8 bottom panel, we apply this spin to the UCAC4-RC-ref-r_{limit} sample, and this time, we can see that the trend is very much similar to the model. It is worth noting that a small change in $\omega_1 g$ and/or $\omega_2 g$ make an important influence in the azimuthal position

In order to be able to compare our result with the reported residual spin vector in the literature, we should convert the reported values into the galactic coordinates. This is done following the equation:

$$\begin{pmatrix} \omega_1 g \\ \omega_2 g \\ \omega_3 g \end{pmatrix} = R_3(180^\circ - l_q).\ R_2(90^\circ - \delta_G).\ R_3(\alpha_G) \begin{pmatrix} \omega_1 \\ \omega_2 \\ \omega_3 \end{pmatrix}$$

$$= \begin{pmatrix} -0.067 & -0.873 & -0.484 \\ 0.493 & -0.450 & 0.745 \\ -0.868 & -0.188 & 0.460 \end{pmatrix} \begin{pmatrix} \omega_1 \\ \omega_2 \\ \omega_3 \end{pmatrix} \tag{8.11}$$

Where $(\alpha_G, \delta_G) = (192.85^\circ, 27.13^\circ)$ and $l_q = 122.93^\circ$. R_1 and R_2 are rotation matrices along respectively the axis towards $\alpha = 0^h$, $\delta = 0^\circ$, and the one towards $\alpha = 6^h$, $\delta = 0^\circ$,. In table 8.1 we summarize our results together with the ones of literature in both equatorial and galactic coordinate system. Note that we can not convert our results to the equatorial coordinate system because of the missing ω_{3g} that could not be computed with our method. We also presented the root mean square of the fit residuals , σ, in the table. Looking at this table, we can see that the values for the ω_{2g} are always a negative and for most of the case it is larger than 1 $\mathrm{mas\,yr^{-1}}$. This is the component towards the galactic rotation.

In order to understand why the result of our least squares method seen in bottom panel of

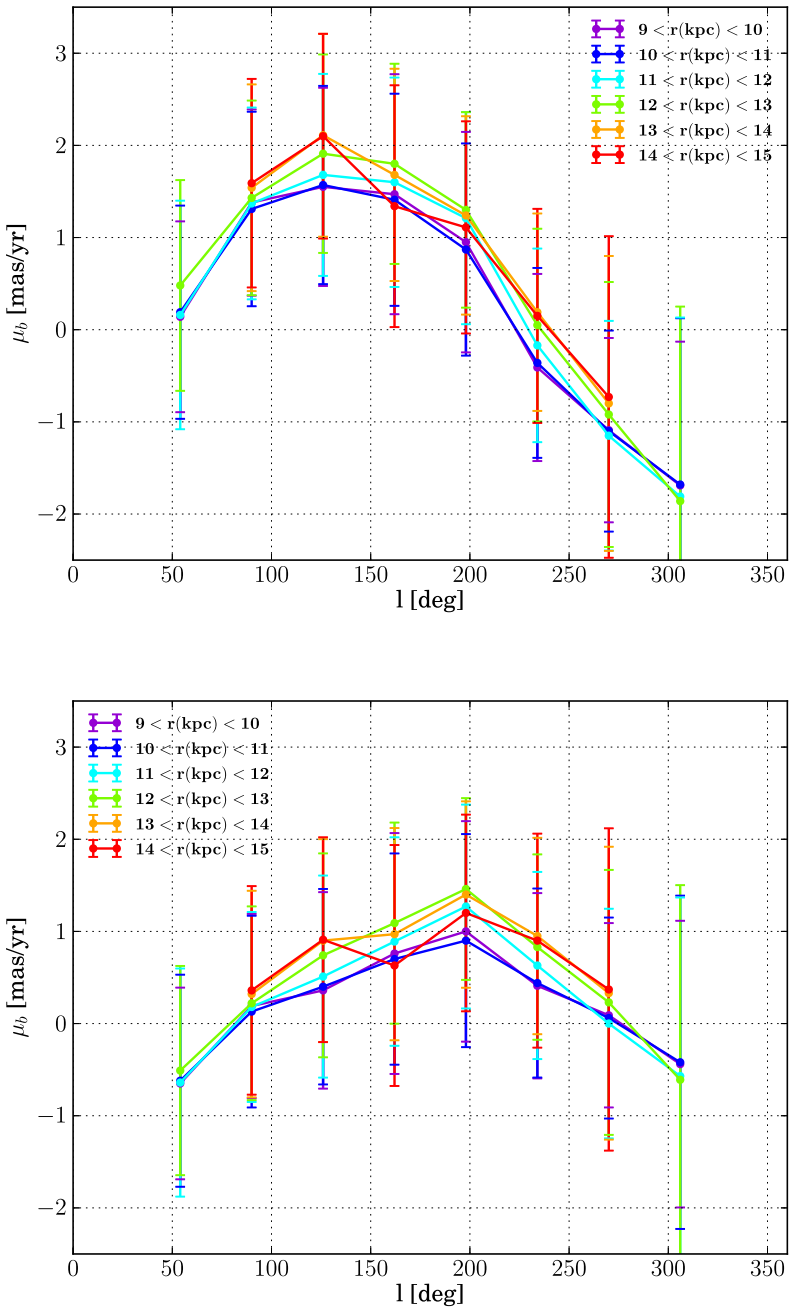

Figure 8.8: The μ_b (referred to the LSR) vs. galactic longitude for UCAC4-RC-ref-r_{limit} sample after their proper motions rotated with a residual spin vector of $(\omega_1 g, \omega_2 g) = (-0.129, -1.92)$ mas yr^{-1} obtained from our least squares fit (top panel), and a spin vector of $(\omega_1 g, \omega_2 g) = (-0.09, -1.55)$ mas yr^{-1} resulted from the least squares fit after removing the outliers (bottom panel).

Fig. 8.8 does not completely match the model seen in Fig. 8.4, we check the residuals of the least squares fit. Looking at the residuals as a function of galactic longitude in the bottom panel of Fig. 8.9, we can see a comparable trend to the one of Y (seen in Fig. 8.6 and over plotted here as well) but with smaller amplitude. The residuals as a function of galactocentric radius (Fig. 8.9 top panel) also have a similar behaviour to the one of Y but in the opposite sense and again with smaller amplitude. Comparing the trend of Y and the residuals in this figure, we can conclude that introducing the obtained residual spin vector, can make the UCAC4 proper motion trend much closer to the expected ones of the model (since the red line is close to zero), but even then, there exists a small systematic trend seen in Fig 8.9 red lines, that may be due to the fact that our warp model does not completely agree with the one of the MW. However, the trend seen in residuals does not exceed ± 0.5 mas yr^{-1} .

The residual spin vector estimated from UCAC4 Quasars

As mentioned before, a non-zero proper motion of quasars reflects the systematics present in a proper motion catalogue. Due to its magnitude limit, UCAC4 contains very few quasars. We wonder if these can be used to help us determine the residual spin vector of the HCRS reference frame. This alternative way, could help us confirm the values we obtain in previous section using the warp model.

We use the 13th edition catalogue of known quasars (Véron-Cetty & Véron 2010, hereafter VV13). The VV13 catalogue contains 133 336 quasars which is the total number known quasars when this catalogue was made. In order to find the quasars in UCAC4, we cross-identify the common objects between VV13 and UCAC4 using both positions and V magnitudes. First, we assume a tolerance of 2 arcsec for cross-matching α and δ positions. Then, we compare the V magnitude provided by both catalogues as shown in Fig. 8.10 and only keep the stars that lie within 1 mag of the identity line. This way, we obtain 568 quasars in the whole sky which we hereafter call *2arcsec-1mag-qso* catalogue. In Fig. 8.11 we show the distribution of this catalogue in galactic longitude and latitude. We also perform the cross-identification considering the same 2 arcsec tolerance for positions, but a 0.5 mag tolerance for V magnitudes and we obtain 452 stars. we will call this catalogue hereafter *2arcsec-0.5mag-qso*.

Considering both components of $\mu_l\, cosb$ and μ_b of the UCAC4 proper motions and a least squares fit, we can evaluate the values of $(\omega_{1g}, \omega_{2g}, \omega_{3g})$. This is done as follows:

$$(\mu_l\, \cos(b)\,)(i)_{UCAC4} - (\mu_l\, \cos(b)\,)_{model} = -\omega_{1g}\, \cos(l_i) \sin(b_i) - \omega_{2g}\, \sin(l_i) \sin(b_i) + \omega_{3g}\, \cos(b_i) \tag{8.12}$$

$$\mu_b(i)_{UCAC4} - \mu_{b\ model} = \omega_{1g}\, \sin(l_i) - \omega_{2g}\, \cos(l_i) \tag{8.13}$$

where (l_i, b_i) is the direction of the UCAC4 object i. As mentioned before, the proper motion of quasars should be zero, therefore in above equations: $(\mu_l\, cos(b)\,)_{model} = \mu_{b\ model} = 0$. In

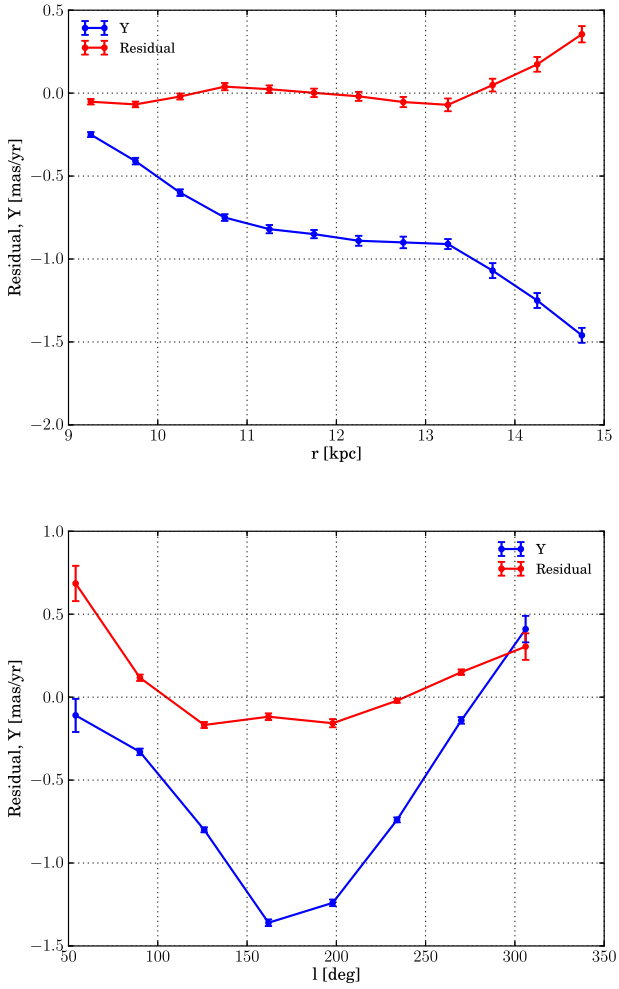

Figure 8.9: The residuals of the least squares fit (in red) and the $Y = \mu_{bUCAC4}(l_i, r_i) - \mu_{b\ model}(l_{bin}, r_{bin})$ (in blue), as a function of galactocentric radius (top panel) and galactic longitude (bottom panel). The circles show the medians in each bin. The statistical error bars of the median are calculated for 95% confidence level.

Table 8.2 we summarised the results of this least squares fit for both 2arcsec-1mag-qso and 2arcsec-0.5mag-qso catalogues. For these catalogues, the proper motions distribution has a long tail that reach to -90 and 70 mas yr^{-1}. This can be due to the unknown large observational errors for faint objects. In order to avoid the outliers, we also consider a case where we cut the tail of 90th percentile in the distribution of $\mu_l cos(b)$ and μ_b which approximately locate at $\pm$17 mas/yr. Note that for all cases a negative ω_3 is obtained. We have seen that a significant negative value for the ω_3, is responsible for the unexpected, negative trend obtained in Fig. 8.5. looking at the galactic coordinates of the residual spin vector, we can see can see here, similar to Tab. 8.1, that all the ω_{2g} values have a negative value. However, it is worth noting that the obtained values for ω components have very large errors and they are compatible with zero at 2σ level.

In order to check the stability of our results, we perform several least squares fits; considering either $\mu_l cos(b)$ or μ_b, i.e. using either eq. 8.12 or eq. 8.13. Also, we use equatorial version of these equations so that we can estimate equatorial $(\omega_1, \omega_2, \omega_3)$ using $\mu_\alpha\, cos(\delta)$ and μ_δ:

$$(\mu_\alpha\, cos(\delta)\,)(i)_{UCAC4} - (\mu_\alpha\, cos(\delta)\,)_{model} = -\omega_1\, \cos(\alpha_i)\sin(\delta_i) - \omega_2\, \sin(\alpha_i)\sin(\delta_i) + \omega_3\, \cos(\delta_i) \tag{8.14}$$

$$\mu_\delta(i)_{UCAC4} - \mu_{\delta\ model} = \omega_1\, \sin(\alpha_i) - \omega_2\, \cos(\alpha_i) \tag{8.15}$$

Here, again note that: $(\mu_\alpha\, cos(\delta)\,)_{model} = \mu_{\delta\ model} = 0$. For this case, we again solve the equations considering either $\mu_\alpha cos(\delta)$ or μ_δ, i.e. using either eq. 8.14 or eq. 8.15. This study could be done using any of the presented quasars catalogues in Table 8.2. Here we show the results for 2arcsec-0.5mag-qso catalogue in Table 8.3. Here we can see that the results of the least squares fit using different equations, agree with each other within their error bars. It is worth noting that the components of residual spin presented in each row of Tab. 8.2 are not exactly the same because they are obtained using the proper motions projected in different directions. We can conclude that the components of the ω obtained with different equations are stable. Similar to results presented at Table 8.2, the spin components are compatible with zero at 2σ level.

8.5 Conclusions

In this chapter we try to look for the kinematic signature of the galactic warp using UCAC4 proper motion catalogue. As shown in Chap. 5, this kinematic signature could be observed in the galactic proper motion, μ_b trend as a function of galactic longitude. The red clump stars of UCAC4 are selected using the provided 2MASS IR magnitudes. Comparing the μ_b trend of these stars with the one expected from our warp simulations we detect a large discrepancy.

We explore a possible source of this discrepancy in terms of a residual spin of the Hipparcos Celestial Reference Frame (on which the UCAC4 reference frame was built) with respect to the extra-galactic inertial one. However, we should bear in mind that other sources of this discrepancy can be systematic mismatch between our warp model and the real Milky Way warp and/or uncertainties in the peculiar velocities of the Sun that we use for correcting the μ_b for the Solar motion.

We turn the problem around and using a least squares fit, we determine under the assumption that our warp model is similar to the one of the MW, what the residual spin components should be to match the observations. The obtained values for the spin vector component in galactic coordinates, ω_{2g}, show a reasonable agreement with ones reported in the literature (Bobylev 2010; Fedorov et al. 2011). Moreover, we use a different approach for estimating this residual spin vector. Identifying few hundreds of quasars in this catalogue and considering the fact that quasars should have a zero proper motion, we perform a least squares fit and check what should be the residual spin vector for which we obtain a zero proper motion for the identified quasars. Due to the small number of quasars in UCAC4, the results have large error bars and they agree to zero in 2σ level. In the following chapter we perform a study on the vertical velocities of the RC stars using PPMXL survey with which we can reach up to fainter magnitudes.

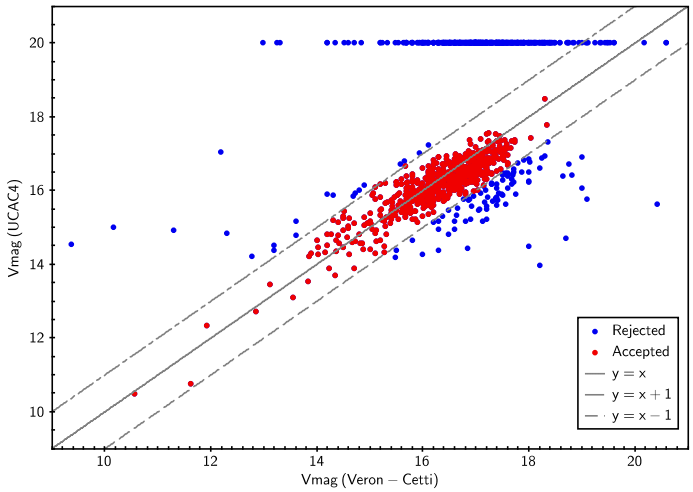

Figure 8.10: V magnitude of UCAC4 vs. the V magnitude provided by Veron-Cetty for our 2arcsec-1mag-qso catalogue. Stars that lay within 1 mag of the identity line are accepted.

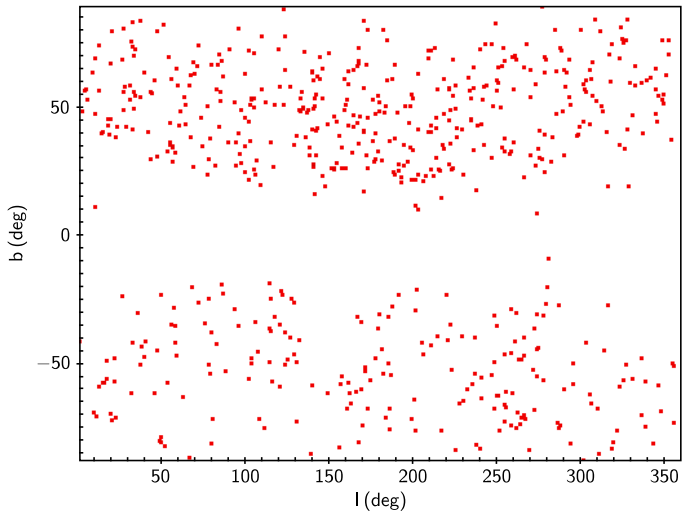

Figure 8.11: The distribution of the 2arcsec-1mag-qso catalogue in galactic longitude and latitude.

Table 8.2: Components of the residual spin vector in equatorial, $(\omega_1, \omega_2, \omega_3)$, and galactic coordinates $(\omega_{1g}, \omega_{2g}, \omega_{3g})$, in units of $\mathrm{mas\,yr^{-1}}$, the root mean square the least squares fit residuals in $\mathrm{mas\,yr^{-1}}$, σ, and the total number of quasars in each catalogue, N. '90' refers to the cases where the tail of 90th percentile in the distribution of $\mu_l cos(b)$ and μ_b have been cut.

Catalog	ω_1	ω_2	ω_3	ω_{1g}	ω_{2g}	ω_{3g}	σ	N
2arcsec-0.5mag-qso	0.73	0.91	-1.05	-0.34 ± 0.51	-0.83 ± 0.52	-1.29 ± 0.72	9.8	452
2arcsec-0.5mag-qso-90	0.35	0.35	-0.33	-0.17 ± 0.36	-0.23 ± 0.37	-0.52 ± 0.51	6.3	370
2arcsec-1mag-qso	0.87	0.88	-0.53	-0.56 ± 0.48	-0.3 ± 0.49	-1.16 ± 0.68	10.3	568
2arcsec-1mag-qso-90	0.66	0.05	-0.232	0.025 ± 0.34	0.13 ± 0.34	-0.69 ± 0.48	6.6	471

Table 8.3: Components of the residual spin vector in equatorial, $(\omega_1, \omega_2, \omega_3)$, and galactic coordinates, $(\omega_{1g}, \omega_{2g}, \omega_{3g})$, in units of $\mathrm{mas\,yr^{-1}}$, and the root mean square the least squares fit residuals in $\mathrm{mas\,yr^{-1}}$, σ,. Results are shown using 2arcsec-0.5mag-qso catalogue.

Data	ω_1	ω_2	ω_3	ω_{1g}	ω_{2g}	ω_{3g}	σ
$\mu_l cos(b)$ & μ_b	0.73	0.91	-1.05	-0.34 ± 0.51	-0.83 ± 0.52	-1.29 ± 0.72	9.8
$\mu_l cos(b)$	0.27	1.51	-1.66	-0.53 ± 0.88	-1.78 ± 0.87	-1.29 ± 0.74	10.1
μ_b	-	-	-	-0.17 ± 0.63	-0.24 ± 0.64	-	9.5
$\mu_\alpha cos(\delta)$ & μ_δ	0.73 ± 0.67	0.92 ± 0.52	-1.04 ± 0.57	-0.35	-0.83	-1.28	9.8
$\mu_\alpha cos(\delta)$	1.09 ± 1.17	-0.16 ± 1.24	-1.06 ± 0.58	0.58	-0.184	-1.41	9.07
μ_δ	0.1 ± 0.61	2.06 ± 0.85	-	-	-	-	10.5

9

Vertical velocities from the PPMXL catalogue

9.1 Introduction

In this chapter we present the work we did in collaboration with Martin López-Corredoira and Francisco Garzón from the IAC. My contribution to this work is presented in Sec. 9.5.1 and partly in Sec. 9.6.1. Here, we follow the same goal that is to derive the vertical motions of disk stars and look for the warp signature in them. PPMXL proper motion catalogue is used which contains the USNO-B1 proper motions cross-correlated with the astrometry and near-infrared photometry of 2MASS catalogue. Having the advantage of reaching up to V$\sim$ 20 in this catalogue, about a hundred thousand quasars can be found. The systematic shifts from zero are calculated using the average proper motions of quasars present in this catalogue, and the corresponding correction are applied to the proper motions of the whole catalogue which reduces the systematic error. As discussed in Chap. 8, being able to reduce the systematics from a proper motion catalogue is a very important step specially when looking for the kinematic signature of the warp.

In this work, the red clump stars are selected from PPMXL catalogue. The vertical velocities of the disc RC stars are calculated in the range of galactocentric radii of $R = 5 - 16$ kpc within 2 kpc in height from the galactic plane. Note that unlike Chap. 8 where we study μ_b proper motions, here we only look into the vertical velocities. The vertical velocity trends are estimated as a function of galactocentric azimuth. A simple analytical model for warp kinematics is considered and its parameters are evaluated by fitting it to the vertical velocities obtained from PPMXL. My contribution to this project was to present an attempt to analyse the

obtained vertical velocities in the context of our kinematic warp model. I perform several warp simulations with different strategies for growing the warp in the disc and different parameters for the geometry. In some cases the warp is grown in an impulsive regime, i.e. very quickly in time, some other have a warp generated adiabatically. Finally, we introduce more complicated cases where we first adiabatically grow the warp and then we decrease its amplitude impulsively. We did all of these experiments in order to see which one of them give us a vertical velocity trend similar to the one of PPMXL data. This way we can get an idea about the generation of the real MW warp. In other words, the observed kinematic trend can give us information on whether the MW warp is generated impulsively or adiabatically and if it is a transient or a long-lived feature.

Something to bear in mind about this chapter is that the Sun is located at $(x, y, z) = (8, 0, 0)$ kpc which is not consistent with the rest of this thesis where we located the Sun at a negative x-axis. Also, the galactocentric azimuth is defined to be zero towards the Sun and positive in clockwise direction as seen from the North Galactic Pole.

9.2 Data from the star catalogue PPMXL: subsample of 2MASS

The star catalogue PPMXL (Roeser et al. 2010) lists positions and proper motions of about 900 million objects and is complete for the whole sky down to magnitude $V \approx 20$. It is the result of the re-reduction of the catalogue of astrometry, visible photometry and proper motions of the USNO-B1 catalogue cross–correlated with the astrometry and near-infrared photometry of the 2MASS point-source catalogue, and re-calculating the proper motions in the absolute reference frame of International Celestial Reference Frame (ICRS), with respect to the barycentre of the solar system. For linking this catalogue to the ICRS, the Hipparcos Celestial Reference Frame (HCRF) that was extended to fainter magnitudes was used. The typical statistical errors of these proper motion is 4-10 mas/yr, while the systematic errors are on average 1-2 mas/yr. From the whole PPMXL, we first selected the subsample of 2MASS sources with $K \leq 14$ and available J photometry. This yielded a total of 126 636 484 objects with proper motions, that is, an average of 3 100 sources deg^{-2}.

As mentioned in Chap. 8, UCAC4 also lists positions and proper motions of about 105 million objects, aiming to be complete for the whole sky down to magnitude $R \approx 16$. Like PPMXL, it also gives proper motion in ICRS reference frame. The UCAC is the first modern high-density, full-sky star catalogue that is not based on photographic images of the sky for most stars, but on recent CCD observations, with higher accuracy in the differential positions. However, given the shorter period of observation of stars, the accuracy of the proper motions is similar to PPMXL: the typical statistical errors of these proper motion is 1-10 mas/yr, while the systematic errors are on average 1-4 mas/yr. The main disadvantage of this catalogue is that the limiting magnitude of $R \approx 16$ does not allow estimating the systematic errors, as we do with PPMXL data in Sec. 9.3.2 because there are very few quasars up to that limiting magnitude.

9.3 Selected red clump stars and contamination

We used the selected red clump (RC) sample from PPMXL by López-Corredoira (2014), where he chose them using the K versus $J-K$ color-magnitude diagrams. The selected sources (almost 20 million) are mostly RCs, but there is also a fraction of contamination. López-Corredoira (2014, Sec. 3.1) discussed this and reached the conclusion that, in the most pessimistic case and for the faintest stars ($K = 13.0$), the contamination might reach 20%, composed of main-sequence stars and giant stars different from RCs. For brighter stars the contamination should be lower.

As discussed in Sec. 8.3, this contamination can bias the average proper motions. The use of median of the proper motions instead of the averages can reduce the effect of contamination. However, we should bear in mind that there might be a systematic error due to this contamination, which we estimate, it would move the median to the position of the ordered set of proper motions in the range of 40-60% instead of 50%.

9.3.1 Proper motion of the RCs

From the mean 3D position of the bin with (ℓ, b, K_0) with a number N of RC stars, we calculate its median proper motion in galactic coordinates: μ_l, μ_b. The angular proper motion is, of course, directly converted into a linear velocity proper motion (v_ℓ, v_b) simply by multiplying $\mu_\ell \cos b$ and μ_b by its distance from the Sun. Only bins with $N > 10$ are included in the calculation. We find the use of the median instead of the average more appropriate because, as said in the previous subsection, it is a better way to exclude the outliers because of all kinds of errors. The statistical error bars of the median are calculated for 95% confidence level. Since the errors of the averages are evaluated by a χ^2 analysis, the confidence level associated with these error bars is not important at this stage; their inverse square was just used as weight in the weighted averages of multiple bins, and the error bar of these averages were quantified from the dispersion. Moreover, as said above, we calculate a systematic error due to contamination: the upper and lower limits correspond to the positions $0.5N \pm 0.1N$ of the ordered set of N data (assuming the worst cases in which the contamination of non-RCs is 20% and that the proper motions of these non-RCs are all higher or lower than the median).

9.3.2 Correction of systematic errors in the proper motions

Proper motions published by the PPMXL catalogue have both statistical and systematic errors. The transmission of the statistical errors is taken into account in the previous steps; however, the systematic errors need to be accounted for as well because they are relatively high. López-Corredoira (2014, Sec. 5) calculated these systematic errors of the proper motions ($Syst[\mu_b]$) as a function of the galactic coordinates using Quasi Stellar Objects (QSOs) as reference of null proper motions and interpolating the value of the systematic error as a function of coordinates.

Then, we subtract this systematic error from each of our proper motions of our bins:

$$(\mu_b)_{\text{corrected}} = \mu_b - Syst[\mu_b](l, b). \tag{9.1}$$

Note that the error bar of $Syst[\mu_b]$ is also a systematic error, so it cannot be reduced by increasing the number of sources. In our case, we derive that this error is still approximately 1 mas/yr in any direction, somewhat lower than the average $|Syst[\mu_b]|$ and, most importantly, $(\mu_b)_{\text{corrected}}$ have an average null deviation with respect to the true values, whereas μ_b does not.

9.4 Deriving the vertical velocity from proper motions

The 3D velocity of the combination of radial velocity (v_r) and proper motions (v_l, v_b) is related to the velocity in the heliocentric reference system by

$$v_r = U\cos l\cos b + V\sin l\cos b + W\sin b, \tag{9.2}$$

$$v_l = -U\sin l + V\cos l$$

$$v_b = -U\cos l\sin b - V\sin l\sin b + W\cos b,$$

where (U, V, W) is the heliocentric velocity of a star. The Sun velocity in this system with respect to the galactic centre is $(U_\odot, V_{g,\odot}, W_\odot)$; the second coordinate

$$V_{g,\odot} = \Theta(R_\odot, z = 0) + V_\odot, \tag{9.3}$$

where $\Theta(R_\odot, z = 0)$ is the rotation speed of the Local Standard of Rest (LSR) with respect to the galactic centre; $(U_\odot, V_\odot, W_\odot)$ is the velocity of the Sun with respect to the LSR. Here, we adopt the values $U_\odot = 14.0 \pm 1.5$ km/s, $V_\odot = 12 \pm 2$ km/s and $W_\odot = 6 \pm 2$ km/s (Schönrich 2012). We used a value of $V_{g,\odot} = 250 \pm 9$ km/s (Schönrich 2012).

We assume that the in-plane velocities of the stars are only those of circular orbits whose rotation speeds vary with the galactocentric radius R. This simplifying assumption can be adopted because we average over large samples, therefore the net velocity of each group of stars is well represented by circular motion. In addition, because we restricted the sample to low galactic latitudes ($|b| < 20°$), the contribution of these in-plane components is further diminished. Hence, we derive the coplanar velocities of the star with respect to the Sun as the projection of the circular speed, $\Theta(R, z)$ (independent of the azimuth ϕ), along each of the velocity axes,

$$U = -U_\odot + \Theta(R, z)\sin\phi, \tag{9.4}$$

$$V = -V_{g,\odot} + \Theta(R, z)\cos\phi.$$

The effect of the warp in these expressions is negligible (López-Corredoira 2014, Sect. 4).

The vertical velocity of the star in the galactocentric system is

$$v_z = W_\odot + W, \tag{9.5}$$

where ϕ is the galactocentric azimuth of the star. Hence,

$$v_z = \frac{v_b}{\cos b} + W_\odot - U_\odot \cos l \tan b - V_{g,\odot} \sin l \tan b \tag{9.6}$$
$$+\Theta(R,z) \sin(\phi + l) \tan b.$$

Eq. (9.6) allows us to determine the vertical velocity only with the determination of the proper motion in the galactic latitude projection and the rotation speed. This is what we do here. We adopt $\Theta(R, z = 0) = 238$ km/s $\forall R$. Note that, since we are at low b, the last three terms in Eq. (9.6) containing Θ, $U_\odot$ and $V_{g,\odot}$ are small and consequently v_z only weakly depends on them; therefore small variations of Θ with respect to the approximation of a flat rotation curve do not significantly change the results in v_z.

9.4.1 Results

We are interested in the region $R > 4$ kpc, $|z| < 2$ kpc, which defines the disk region. For $R < 4$ kpc we find the non axisymmetric structure with non circular orbits of the long bar (Amôres et al. 2013). For $|z| > 2$ kpc, the halo becomes important and the stellar density of the disk is a factor $\lesssim 300$ lower than at $z = 0$ (Bilir et al. 2008).

The result of the calculation of v_z according to Eq. (9.6) is plotted in Fig. 9.1, including a weighted average of all the bins with common x, y (galactocentric coordinates, with the position of the Sun at $x = 8$ kpc, $y = 0$). We plot the velocities v_z obtained from μ_b without correcting for systematic errors of the proper motions and with the corrected $(\mu_b)_{\rm corrected}$ from Eq. (9.1). It is clear that the correction is substantial and the uncorrected plot has high velocities that are not real.

The right panel of Fig. 9.1 shows a map of velocities with lower vertical motions in most of the bins after the correction (taking into account that the error bars of each plotted bin are ≤ 50 km/s). In Fig. 9.2 we show the same kind of map, but with higher resolution velocity and dividing the total sample into three subsamples of different z. The southern hemisphere map ($-2 < z$(kpc) < -0.67) shows additional deviations from zero velocity. We can also see that the negative vertical velocity on the galactic plane (middle panel) is not so significant. In Figs. 9.3 and 9.4, we show the results of v_z as a function of ϕ within $|z| < 2$ kpc or as function of z averaging over all values of ϕ for different ranges of R.

In these plots the error bars of the different bins are not entirely independent because the systematic errors are not independent. The error bars are dominated by the systematic errors because of the contamination of non-RCs (we have assumed the most pessimistic scenario of a 20% contamination and that the proper motions of these non-RCs are all higher or lower than

the median) and the systematic errors of the proper motions derived using the QSOs reference; see Fig. 9.5 for an example of decomposition or errors for $R = 10$ kpc.

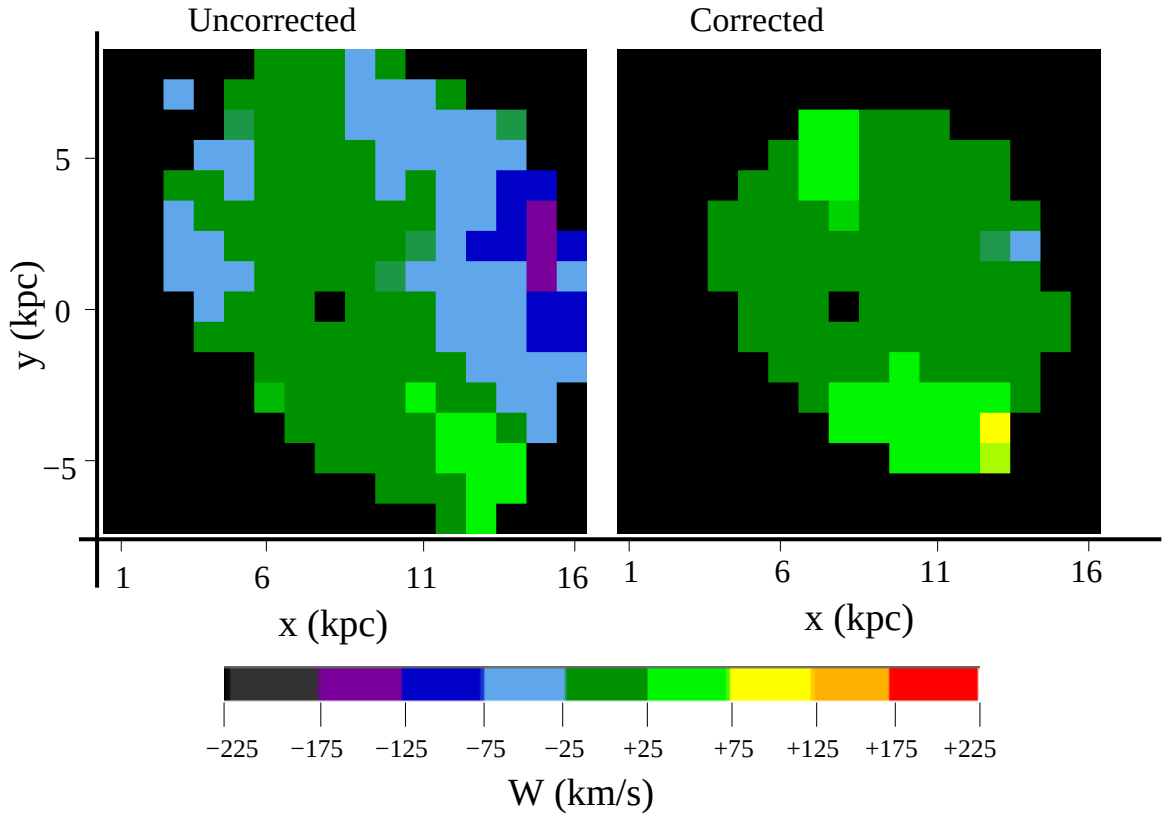

Figure 9.1: Average vertical velocity using PPMXL data as a function of galactocentric Cartesian coordinates x, y (the position of the Sun is $x = 8$ kpc, $y = 0$) for $|z| < 2$ kpc. Only bins with error bars lower than 50 km/s are plotted; black indicates larger errors or absence of data. The left panel is the weighted average of the bins without correcting for systematic errors of the proper motion. The right panel is the weighted average of the bins including the correction for systematic errors of the proper motion.

9.5 Relating the vertical motion to the warp kinematics

If we consider that this vertical motion a result of the warp, modelled as a set of circular rings that are rotated and whose orbit is in a plane with angle $i_w(R)$ with respect to the galactic plane, then

$$v_z = \Omega(R, z' = z - z_w) \sin[i_w(R)] \cos(\phi - \phi_w) + \dot{z_w}, \tag{9.7}$$

$$z_w(R, \phi) = R \tan[i_w(R)] \sin(\phi - \phi_w), \tag{9.8}$$

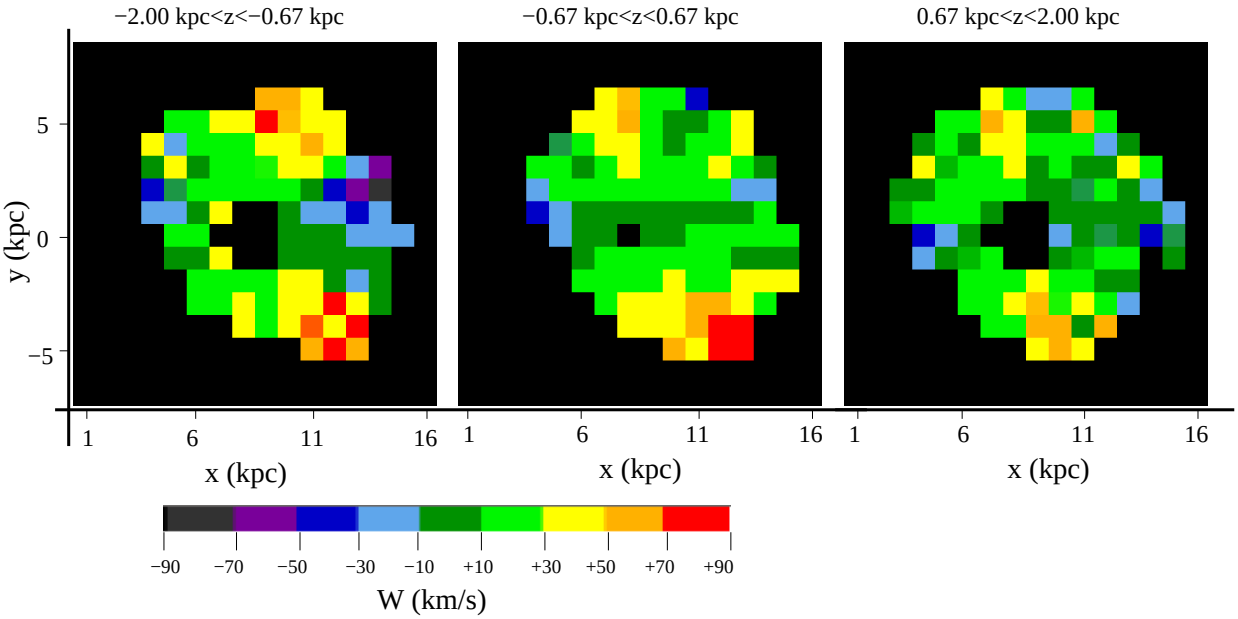

Figure 9.2: Average vertical velocity using PPMXL data, including the correction for systematic errors of the proper motion, as a function of galactocentric Cartesian coordinates x, y (the position of the Sun is $x = 8$ kpc, $y = 0$) for different ranges of z. Only bins with error bars lower than 50 km/s are plotted; black indicates larger errors or absence of data.

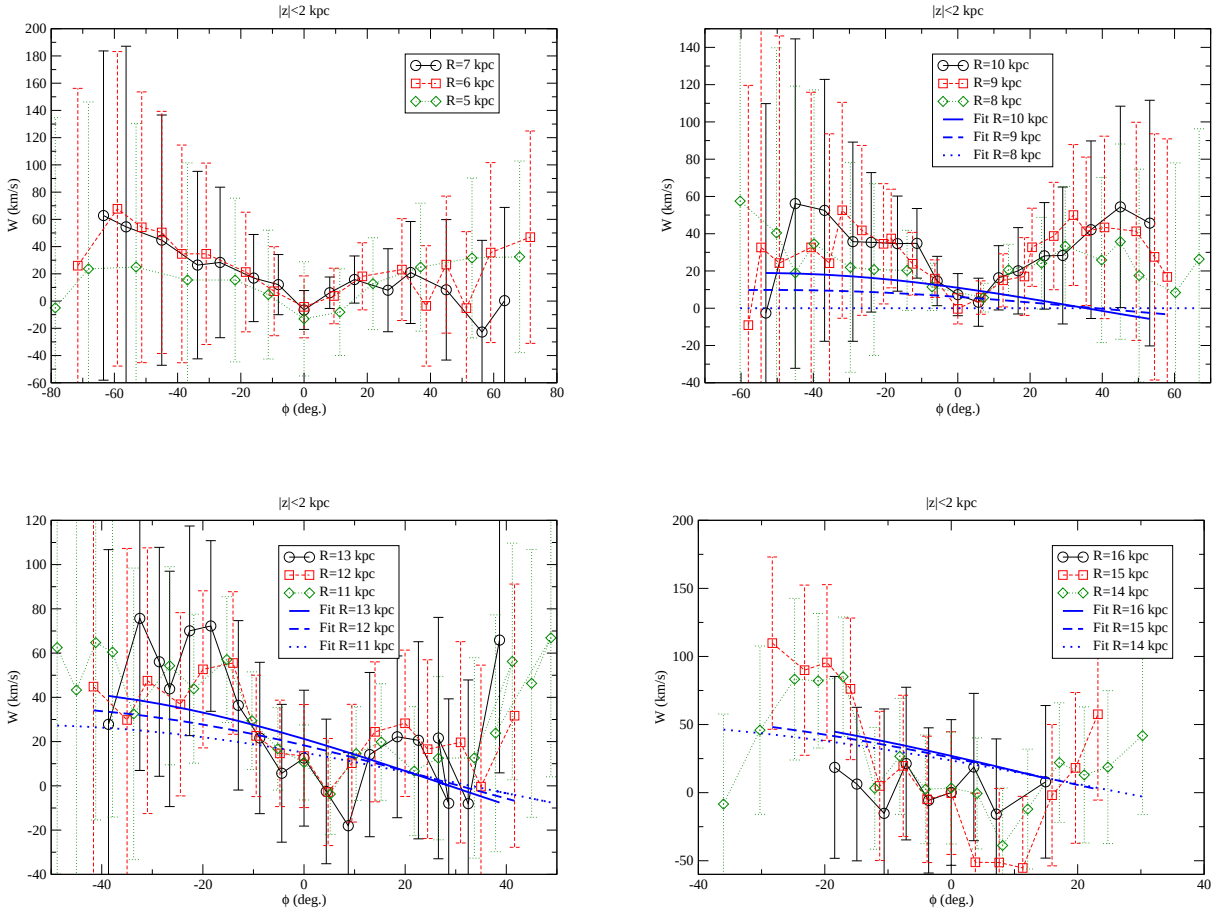

Figure 9.3: Average vertical velocity as a function of galactic cylindrical coordinates R, ϕ for $|z| < 2$ kpc. For $R \geq 8$ kpc, we also show the best fit given by Eq. (9.11).

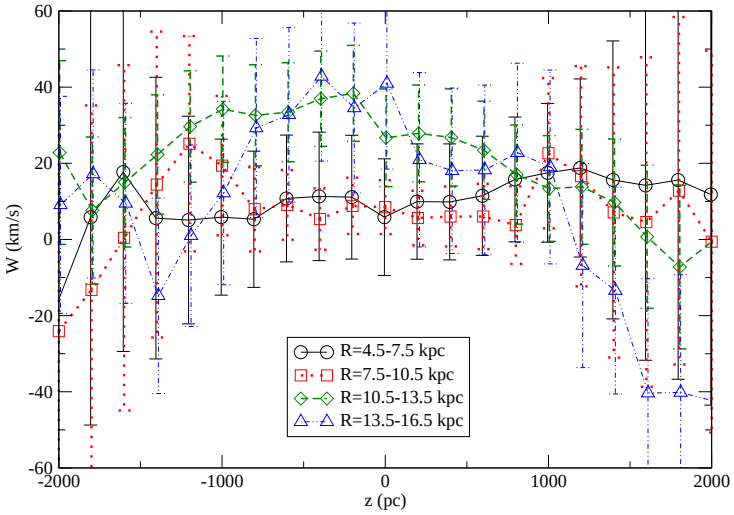

Figure 9.4: Average vertical velocity as a function of the vertical position, z, for different ranges of galactocentric distances R.

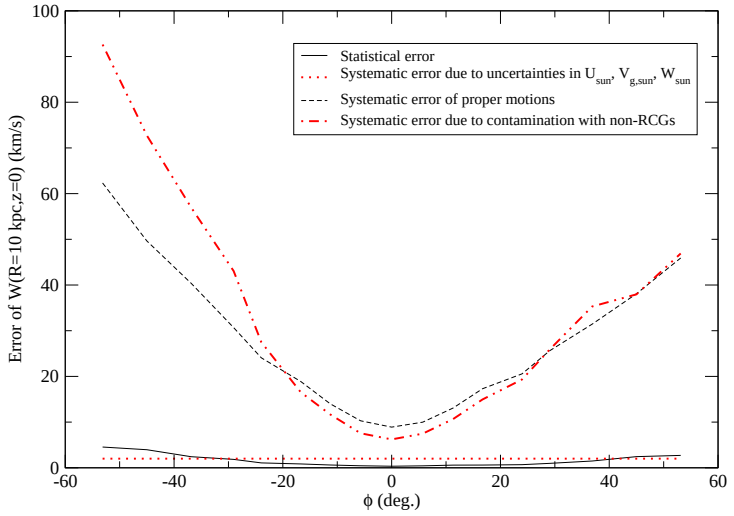

Figure 9.5: Decomposition of the four error sources, which sum quadratically to give the error bars plotted in Fig. 9.3 for $R = 10$ kpc.

where ϕ_w is the azimuth of the line of nodes, and z_w is the height of the disk over the $b = 0$ plane. We assume the greatest height of the warp to be

$$z_w(R > R_\odot, \phi = \phi_w + \pi/2) \approx \gamma(R - R_\odot)^\alpha, \tag{9.9}$$

and an invariable line of nodes (extremely slow precession, i.e. $\dot{\phi_w} \ll \dot{\gamma}$) and no change in the shape of the warp. We also assume, as above, a constant $\Omega(R, z) = \Omega_{LSR} = 238$ km/s; this may be slightly reduced for high R or high $|z|$ (López-Corredoira 2014), but the order of magnitude does not change, so v_z is only weakly affected by a change of the rotation speed. Joining these assumptions, we derive, for low angles $i_w(R)$,

$$v_z(R > R_\odot, \phi, z = 0) \approx \frac{(R - R_\odot)^\alpha}{R}[\gamma\omega_{LSR}\cos(\phi - \phi_w) + \dot{\gamma}R\sin(\phi - \phi_w)]. \tag{9.10}$$

We adopt the values $\alpha = 1$ (Reylé et al. 2009), $\phi_w = +5 \pm 10$ deg, in the middle of the range of azimuths given in the literature for the stellar warp between -5 and +15 deg. (López-Corredoira et al. 2002b; López-Corredoira 2006; Momany et al. 2006; Reylé et al. 2009), and we use our regions with $R \geq 8$ kpc to obtain the best fit:

$$v_{z,\,\mathrm{best\,fit}} = (54 \pm 38\,\mathrm{km/s})\left(1 - \frac{R_\odot}{R}\right)[\cos(\phi - \phi_w) - (0.14 \pm 0.07\,\mathrm{kpc}^{-1})R\sin(\phi - \phi_w)]. \tag{9.11}$$

$\chi^2 = 68.5$ for $N = 153$. The errors include the error derived from a χ^2 statistical analysis (for 68.3% C.L.) and the uncertainty in ϕ_w. The function is plotted in Fig. 9.3. Hence, the values of γ and $\dot{\gamma}/\gamma$ that fit our data are

$$\gamma = 0.23 \pm 0.16, \tag{9.12}$$

$$\frac{\dot{\gamma}}{\gamma} = -34 \pm 17\,\mathrm{Gyr}^{-1}. \tag{9.13}$$

If we assume an exponent $\alpha = 2$ instead of $\alpha = 1$ we get: $\gamma = 0.032 \pm 0.024$ kpc^{-1}, $\frac{\dot{\gamma}}{\gamma} = -49 \pm 29$ Gyr^{-1}, which shows the same trend of decreasing amplitude of the warp with similar frequency. The observed trend only mildly depends on the assumed shape of the warp. The lower χ^2 for $\alpha = 2$ is 84.2 ($N = 153$), higher than for $\alpha = 1$, so we assume the $\alpha = 1$ values in the rest of this paper.

These results (for $\alpha = 1$) can be interpreted as follows:

1. Our data are not good enough to trace the structure of the stellar warp. There are much better methods to derive the morphology with positions and velocities of the warp stars, for example, the GC3 family of methods (as described in Chap. 6). At least we are able to derive a range of γ that is compatible with other measurements of the stellar warp

height. For instance, from Eq. (9.9), we compute a maximum height of 0.92 ± 0.56 kpc at $R = 12$ kpc or 1.61 ± 0.98 kpc at $R = 15$ kpc, compatible with the values obtained by López-Corredoira et al. (2002b), Momany et al. (2006), or Reylé et al. (2009).

2. We can derive some information of the warp kinematics in addition to the circular motions of the stars around the galactic centre. Eq. (9.13) indicates that our warp is not stationary ($\dot{\gamma} = 0$), although only at 2σ. If we assume a sinusoidal oscillation, $\gamma(t) = \gamma_{\max} \sin(\omega t)$, we have a period

$$T = \frac{2\pi}{\omega} = 2\pi \left(\frac{\dot{\gamma}}{\gamma}\right)^{-1} \cot(\omega t), \tag{9.14}$$

and the probability of having a period T is the convolution of two probability distributions: the Gaussian probability as a result of the error bar of $\dot{\gamma}/\gamma$; and the probability proportional to the amount of time Δt in which we can observe values corresponding to $\dot{\gamma}/\gamma$ and a period between T and $T+\Delta T$, which is proportional to $\left|\frac{d(\omega t)}{dT}\right| \left(\frac{\dot{\gamma}}{\gamma} = \text{constant}\right) = \frac{1}{2\pi}\left|\frac{\dot{\gamma}}{\gamma}\right| \frac{1}{1+\left(\frac{T\dot{\gamma}}{2\pi\gamma}\right)^2}$. The normalised convolution of these two probabilities gives

$$P(T)dT = \frac{dT}{2^{1/2}\pi^{5/2}\sigma_x} \int_{-\infty}^{+\infty} dx \frac{|x|}{1+\left(\frac{Tx}{2\pi}\right)^2} e^{-\frac{(x-x_0)^2}{2\sigma_x^2}}, \tag{9.15}$$

where $x_0 \equiv \frac{\dot{\gamma}}{\gamma}$ and σ_x is its r.m.s. Fig. 9.6 shows this probability distribution.

From this distribution, the cumulative probabilities of 0.159, 0.500, and 0.841 are given for $T = 0.047$, 0.208, and 1.049 Gyr, respectively, so we can say that $T = 0.21^{+0.84}_{-0.16}$ Gyr (68.3% C.L.), or $T = 0.21^{+10.56}_{-0.20}$ Gyr (95.4% C.L.). Alternatively, we can say that $T < 0.43$ Gyr (68.3% C.L.), $T < 4.64$ Gyr (95.4% C.L.).

Our results are equivalent to a rotation of the rings around the line of nodes with an angular velocity of $\frac{\dot{z_w}(R>R_\odot, \phi=\phi_w+\pi/2)}{R} \sim -8\left(1-\frac{R_\odot}{R}\right)$ km/s/kpc, which is between -1 and -4 km/s/kpc in the range of R between 9 and 16 kpc. The negative value means a decreasing amplitude of the warp with time. This result disagrees with the result of +4 km/s/kpc given by Miyamoto et al. (1993) or Miyamoto & Zhu (1998) at short distances from the Sun, but it is more similar to the result of -4 km/s/kpc by Bobylev (2010), who also used red clump giants. Bobylev (2013) obtained with Cepheids a value of -15 km/s/kpc, which is different from our result. We do not know the reason for this last disagreement; indeed, our plot of Fig. 9.3 for $R = 8 - 10$ kpc is similar to the plot of $W(Y)$ in Fig. 3 of Bobylev (2013). If Bobylev (2013) had interpreted his term of $\frac{\partial V}{\partial z}$ in a different way, in terms of a variation of the rotation speed with z, for instance (López-Corredoira 2014), and so considering null the deformation tensor, this would lead to an angular speed of -2 km/s/kpc, compatible with what we see.

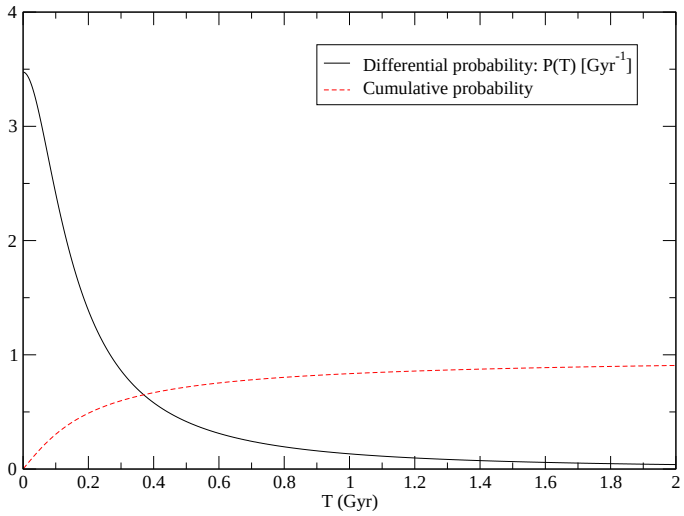

Figure 9.6: Distribution of probability of the period for the motion of $\gamma(t) = \gamma_{\max} \sin(\omega t)$ given that we have observed $\frac{\dot{\gamma}}{\gamma} = -34 \pm 17\,\mathrm{Gyr}^{-1}$.

9.5.1 Toward a more realistic warp kinematic model

In part II of this thesis, we introduce a new kinematic model for the Milky Way warp. Using a test particle simulation, a realistic galactic potential, and a geometrical model for the warp, the disk potential was warped and stars were let to evolve in it. This way, a warped sample of stars was generated that not only follow the warped disk, but their kinematical information also reflects the signature of the warp. In this model the particles evolve in an adiabatic regime, that is, the warp grows slowly enough so that the stars remain in statistical equilibrium with the potential (hereafter model A).

The PPMXL proper motions (see Sect. 9.5) suggest that the galactic warp is probably not in a steady state and its amplitude can change rapidly with time. From equations (9.12) and (9.13), we obtain a negative value for $\dot{\gamma}$, which implies that the warp amplitude decreases with time. In this section, we present a first attempt to analyse the PPMXL data in the context of a new kinematic warp model. We simulated a warped sample of RCs (see part II of this thesis). We first grow the warp in the galactic disk adiabatically during a time $t_1 = 3.5$ Gyr until it reached a tilt angle of $\psi_1 = 16^\circ$ at the galactocentric radius of 16 kpc, where $\psi \equiv \frac{z}{R}$. Then, we decreased its amplitude impulsively, following Eq. 4.1, during a time $t_2 = 100$ Myr to achieve a tilt angle of $\psi_2 = 6^\circ$ at the galactocentric radius of 16 kpc (hereafter model B), to quantitatively mimic the rapid warp evolution obtained in section 5. We set the tilt angle to be a linear function of the galactocentric radius ($\alpha = 1$ in Eq. 3.3). We performed this simulation for 56×10^6 RCs. This is the total number of RCs in the galactic disk according to the Besançon Galaxy Model Romero-Gómez et al. (2015). We defined the line of nodes to coincide with the Sun-galactic centre line ($\phi_w = 0$) in the simulations.

In Fig. 9.7 we plot the resulting v_z velocity component as a function of galactocentric azimuth for RCs at R between 13 and 14 kpc. To show the global trend, we plot the v_z for the whole range in azimuth, whereas in Fig. 9.3 we just plotted the range for which we have enough data. To facilitate the comparison, we only show this plot for one of the radius bins presented in Fig. 9.3. As expected, for a simulation where the warping occurs in an adiabatic regime, that is, stars remain in statistical equilibrium with the warped potential (model A), the highest peak of v_z is always observed in the direction of the line of nodes. Whereas for model B, this peak moves towards negative galactic azimuths and gains a larger amplitude. We checked that its amplitude and azimuthal position depends on t_2 and ψ_2; increasing them causes the amplitude to become larger and it moves toward the more positive azimuths. We also have checked that a deviation of 5° of the line of nodes from the Sun-galactic centre line will cause the strongest peak seen in Fig. 9.7 to be slightly shifted by $\sim 5^\circ$ toward the positive azimuths, which is negligible for our qualitative study. The blue-shaded regions show the error bars in v_z for model B that are standard deviations, representing the intrinsic velocity dispersion after evolution in the warped potential. The black line shows the fit to PPMXL data, the same as the fit seen in Fig. 9.3in the bottom-left panel. The simulations qualitatively follow the same trend as the

fit. We checked that by increasing t_2 by a few more hundred million years, the amplitude of the peak will decrease and it will move toward the more positive azimuths. Therefore, this very impulsive change in the amplitude of the warp ($t_2 = 100$ Myr) is a very important parameter for obtaining the same trend as we found for the PPMXL fit. With higher radii for the simulation of model B, the amplitude of the peak in v_z increases until it reaches ~ 60 km/s at $R = 16$ kpc, which is very similar to the result from the PPMXL fit for this radius (see Fig. 9.3 bottom right panel).

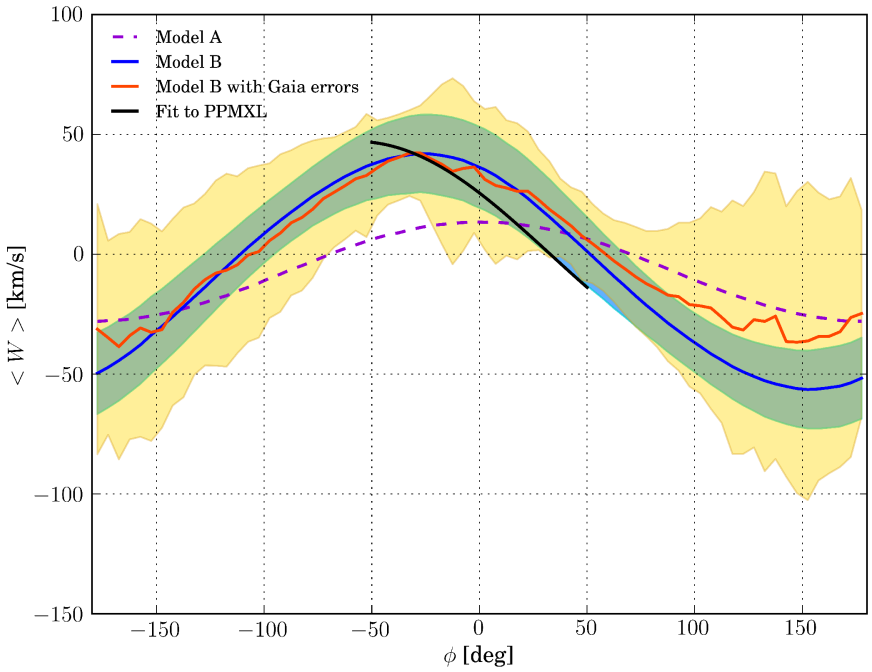

Figure 9.7: Mean v_z velocity component as a function of galactocentric azimuth for RC stars at $13 < R(\text{kpc}) < 14$. RCs simulated using models A and B are plotted as dashed purple and solid blue lines. The fit to PPMXL data is given in black, the same as the fit in Fig. 9.3 in the bottom-left panel. The Gaia 'observed' values are plotted in red. The shaded regions in blue and yellow represents the standard deviations of the v_z velocity for model B without and with Gaia errors. The line of nodes is defined to coincide with the Sun-galactic centre line ($\phi_w = 0$).

In a perturbation on the galactic disk in such a short dynamical time-scale, the stars will not remain in equilibrium with the imposed warp and will cease to show the behaviour seen in Fig. 9.7 after evolving a few more orbital periods. This clearly indicates that this perturbation must be a transient phenomenon.

9.6 Improving the accuracy of our results

The accuracy of our results is low, and we only report a tentative detection of vertical motion with low significance. One may wonder how this result might be improved. From Fig. 9.5, we understand the origin of our large error bars: the statistical errors are low (we have 20 million RCs, so this is expected), and the inaccuracy of the solar motions with respect to the LSR is also unimportant; but there are two strong error sources: 1) the systematic errors of the proper motions, even after correcting them with the quasars reference; and 2) the contamination of non-RCs. The accuracy of the systematic errors in the proper motions will be much improved in future surveys in the visible, mainly with Gaia (Perryman et al. 2001, Lindegren et al. 2008), which will also have many millions of RCs among their sources Romero-Gómez et al. (2015). Hence, we must wait for the Gaia second data release (estimated to be at 2017) to be able to significantly decrease the systematic error of proper motions. To avoid the contamination of non-RCs, APOGEE spectroscopic data (Bovy et al. 2014) or asteroseismology data (Kallinger et al. 2010) might be used. However, López-Corredoira et al. (2014) showed that using the current sample of RC stars selected spectroscopically with APOGEE data can not improve the results seen in previous section, due to the fact that it contains too few RC stars and there are not enough RC stars at $R > 14$ kpc.

9.6.1 Estimating the accuracy with future Gaia data

With future Gaia data, we will improve the precision in the vertical velocities, because the systematic errors will reduce from about 1 mas/yr in the PPMXL (after applying the correction of Sect. 9.3.2) to the quoted 70 to 80 μas/yr in Gaia (Luri et al. 2014). Thus the contribution of the systematics in Fig. 9.5, for example, will drop to a level of a few km/s. This will yield an improvement of about $\sqrt{2}$ in the final error, which will be largely dominated by the contamination caused by the poor identification of red clump sources.

If, in turn, we combine a catalogue with clearly identified sources as the spectroscopically selected red clumps in APOGEE, then the errors in the vertical velocities can be strongly decreased, even to the level of the systematic error of the Gaia measurement discussed above. In spite of the paucity of sources, the precision of the vertical velocity estimate can be restricted to a few km/s, but the effect of the lack of spatial coverage in determining the overall shape of the vertical velocity of the full warp structure still remains.

Moreover, the trigonometric parallaxes provided by Gaia, will help us improve the accuracy in distance estimation of RC stars. Using the nominal Gaia error models, we have calculated that toward the galactic anti-centre a relative error in parallax of better than 10% can be reached at a galactocentric distance of about 13 kpc. This calculation was made considering the interstellar extinction (Drimmel et al. 2003). However, for stars with larger trigonometric parallax errors, a combination of photometric distances and trigonometric parallaxes will enhance the distance

estimate. In addition, knowing more accurate distances will decrease the non-RCs contamination in the sample. For instance, dwarf contamination can easily be removed because they are located at much smaller distances than RCs.

To determine the observed trend of the warp kinematic model used in Sect. 9.5.1 when Gaia data are used, we applied the Gaia observational constraints to the simulated model B sample. Using the nominal Gaia performances, we calculated the errors in trigonometric parallax and proper motions (see Sec. 7.2 for details). The 'observed' values in Fig. 9.7 can follow the true values except for the regions toward the far side of the Galaxy where the interstellar extinction is very high and accordingly, there are fewer stars per longitude bin. The position of the peak in v_z can be clearly detected in the observed values.

9.7 Conclusions

Our analysis of the proper motions with the PPMXL survey shows a tentative detection [within $\sim 2\sigma$, according to the result of Eq. (9.13)] of the vertical oscillation produced in the southern warp, which tends to decrease its amplitude ($\dot{\gamma} < 0$, i.e., $W > 0$ for $z_w < 0$). A simple model with $z_w(R,\phi) = \gamma(R - R_\odot)\sin(\phi - \phi_w)$ is well fitted with $\gamma = 0.23 \pm 0.16$, $\frac{\dot{\gamma}}{\gamma} = -34 \pm 17\,\mathrm{Gyr}^{-1}$. There are two contributions of the warp to the vertical motion: one produced by the inclination of the orbits, another contribution from the variation of γ. We were able to detect, both analytically (Sec. 9.5 and with simulations (Sec. 9.5.1), that the second factor is necessary to fit our data. If we assume this detection of $\dot{\gamma} \neq 0$ to be real, the period of this oscillation is shorter than 0.43 Gyr at 68.3% C.L. and shorter than 4.64 Gyr at 95.4% C.L., excluding at a high confidence level the slow variations ($T > 5$ Gyr) that correspond to long-lived features. But because we observe this vertical motion only in the southern warp, this most likely indicates that the main S-shaped structure of the warp is a long-lived feature, whereas the perturbation that produces an irregularity in the southern part is most likely a transient phenomenon. Moreover, the simulations used in Sec. 9.5.1 indicate that the galactic disk potential is perturbed on a very short time scale, that is, in an impulsive regime, and therefore stars cannot remain in statistical equilibrium with the potential. This will cause the observed southern warp signature to be lost in a few orbital periods.

Higher precision data, which surely will be available in the near future, are necessary to resolve this problem. With the accuracy of the present-day data one cannot go proceed. In future analyses with upcoming surveys such as Gaia together with spectroscopic follow-up of some sources such as the present-day APOGEE or Gaia-ESO survey (Randich et al. 2013), a much higher accuracy is expected for these results. Our present measurements of v_z in the farthest part of the disk are poor, with errors of several tens of km/s, but the errors can be reduced by an order of magnitude if we use the future Gaia data plus a spectroscopic classification of red clump giants up to distances of $R = 16$ kpc. This will surely reveal the true character of the vertical motion measured here.

Part V

Conclusions

10

Summary, Conclusions and perspectives

In this thesis we test the capability of several methods to identify and characterise the warping of the stellar disc of our Galaxy in the Gaia era. We use the family of Great Circle Cell Counts (GC3) methods. These methods can work with samples for which full six-dimensional phase-space information is provided (mGC3 method, introduced by Mateu et al. 2011); samples for which radial velocity is lacking (nGC3 method, newly developed here); or samples having only positional information (GC3 method, firstly introduced by Johnston, Hernquist & Bolte 1996). Moreover, LonKin methods are introduced which are basically the trend of vertical motions of stars as a function of galactic longitude.

We developed an analytical expressions for the force field of a warped Miyamoto-Nagai potential. Starting from the Galactic axisymmetric potential model of A&S, we distort the potential according to two different warp models: 1) a model with a straight line of nodes and 2) a model with twisted line of nodes. Using a set of test particles that are relaxed in the A&S potential, we warp the disc potential adiabatically, allowing the particles to follow the bended potential and not be left behind. In some cases a twist is introduced additionally through a purely geometric transformation of the particle's phase-space coordinates.The kinematic distribution of our synthetic samples mimic three different tracer populations: OB, A and Red Clump (RC) stars.

The modified Great Circle Cell Counts method (mGC3) assume stars in a fixed galactocentric ring are confined to a great circle band, with their galactocentric position and velocity vector perpendicular to the normal vector which defines this particular great circle. The peak of the distribution in the pole count map, i.e. in the map of the number of stars associated to each great

circle cell, is then identified using a Bayesian fitting procedure, which results in the identification of the tilt and twist angles of the warp and their corresponding confidence intervals.

Considering the spatial distribution from the new Besançon Galaxy Model and using the 3D extinction map of Drimmel et al. (2003), we have generated realistic mock catalogues of OB, A and RC stars where a very complete model of Gaia observables and their expected errors are included. We have tested our methods and found their range of applicability, identifying the main sources that limit them. We found that the introduction of the kinematic information in the methods (mGC3 and nGC3) improves the recovery of the tilt angle to discrepancies less than $\sim 0.75^\circ$ for most of the cases, whereas using only positional information (GC3 method) the tilt angle recovery is systematically overestimated by $\sim 2^\circ$. Although seemingly small, for galactocentric distances $r \lesssim 12$ kpc, where the tilt angle is expected to be quite small, this 2° systematic trend represents an error of larger than 100% in the tilt angle. We have been able to recognise the biases in the results introduced both by the fact that Gaia provides non-symmetric errors in trigonometric distances and that we are working in an apparent magnitude limited sample. The OB and RC stars samples are good warp tracers, whereas the A stars sample is not quite up to the task for galactocentric distances larger than ~ 12 kpc, mainly due to their fainter intrinsic luminosity. Using data with good astrometric quality (relative parallax accuracy of 20% or better), we obtain remarkably good accuracy recovering the tilt angle for all three tracers, provided we have enough stars in the galactocentric radius bins. We propose an empirical criterion to identify at which distance the nGC3 and mGC3 results from the Clean sample (the sample with relative parallax accuracy smaller than 20%) start being significantly affected by biases. According to this rule of thumb, we should discard the galactocentric radius bins for which the number of stars has decreased down to $\lesssim 10\%$ of the total stars in the innermost bin ($9 < r_{obs} < 10$ kpc). Using the Clean sample of OB stars warped with the twisted warp model, the twist angle is recovered to within $< 3^\circ$ for all distances. It is worth noting that throughout this thesis we have used trigonometric parallaxes in the computation of pole counts with all three methods (Chap. 6). For standard-candle tracers such as RC stars, or others not explored in this work such as RR Lyrae stars or Cepheids, an even better performance could be achieved with the use of photometric parallaxes for the faintest stars with large trigonometric parallax errors ($\Delta\varpi/\varpi > 20\%$). By comparing the different variants of the methods, the power of exploiting kinematical information becomes apparent.

In this work we have developed a first and simplified kinematic model for our Galactic warp. The simplicity of the model has allowed us to evaluate the efficacy and limitations of the use of Gaia data to characterise the warp. These limitations have been fully explored and quantified. From the work done so far, we expect that the Gaia database, together with the methods presented here, will be a very powerful combination to characterise the warp of the stellar disc of our Galaxy.

Using the LonKin method we can predict the kinematic signature of the warp in Gaia observable space. We have seen that this signature can be best observed in mu_b proper motions.

Applying this method to the mock catalogue of RC stars we obtain a trend that peaks with a maximum value towards anti-centre and grows with galactocentric radius. We decide to look for this kinematic signature of the galactic warp in the available proper motion catalogues. We first present the results using the RC stars of UCAC4 catalogue (Zacharias et al. 2013). Surprisingly, using this data we obtain a mu_b trend with minimum towards anti-centre. We suspect that this trend is due to the systematic errors present in this catalogue mainly caused by a residual spin of the reference frame with respect to the extra-galactic inertial one. The reason why the mu_b trend can be significantly biased by the residual spin vector is that from our warp model, we expect the warp signature to be in the order of ~ 1 mas yr^{-1} and some of the reported values from the literature for the residual spin components (Bobylev 2010; Fedorov et al. 2011) are approximately of the same order. Using a least squares fit and under the assumption that our warp model is similar to the one of the MW, we determine the residual spin components for which the observations match the model. The obtained values for the spin vector component towards the galactic rotation, ω_{2g}, show a reasonable agreement with ones reported in the literature (Bobylev 2010; Fedorov et al. 2011). Since this catalogue is complete down to R$\sim$ 16, we only Identify few hundreds of quasars. Due to their very large distances, these objects are supposed to have zero proper motions. We perform a least squares fit and check what should be the residual spin vector for which we obtain a zero proper motion for the identified quasars. Due to the small number of quasars in UCAC4, the results have large error bars and they agree to zero in 2σ level. This study show us the necessity of correcting for this possible residual rotation of reference frame and any other systematics when looking for the kinematic signature of the warp. It is worth mentioning that Gaia is expected to determine this residual spin with a precision of 0.4 μas yr^{-1}.

In a similar study, using the proper motions of PPMXL catalogue (Roeser et al. 2010) and IR distances, we look into the vertical velocities for RC stars. Having the advantage of reaching up to V$\sim$ 20 in this catalogue, about a hundred thousand quasars can be found. The systematic shifts from zero are calculated using the average proper motions of quasars present in this catalogue, and the corresponding correction are applied to the proper motions of the whole catalogue which reduces the systematic error. A simple analytical model of vertical displacement due to the warp is fitted to the data which gives us a 2σ detection of a vertical oscillation produced in the southern warp, which tends to decrease the amplitude of the warp. Since this vertical oscillation is only observed in the southern warp, this most likely indicates that the main S-shaped structure of the warp is a long-lived feature, whereas the irregularity in the southern part is most probably a transient phenomenon. This work with PPMXL was performed by Martin López-Corredoira and Francisco Garzón from the IAC. My contribution to this work was to analyse the PPMXL vertical velocity trend in the context of our kinematic warp model. Considering different strategies for growing the warp in the disc and different parameters for the geometry, I performed several test particle simulations of the warp. In some cases the disc potential is being warped in an impulsive regime, i.e. very quickly in time, some other the

warp is generated adiabatically. Finally, we introduce more complicated cases where we first adiabatically grow the warp and then we decrease its amplitude impulsively. The later case was inspired by the results obtained by the fit to the data. We see that the impulsive decrease of the warp's amplitude can qualitatively reproduce the vertical velocity trend of PPMXL. Changing the disc potential impulsively with time, indicates that the stars can not stay in statistical equilibrium with the warped disc potential and therefore we expect that this observed southern kinematic signature to be lost in a few orbital periods.

Currently, we are developing a more complex and realistic developments that is generating lopsided warp models and calculate the corresponding force field. Having a lopsided warp we do not expect to get a single well defined peak in the pole count maps of GC3 family of methods. Depending of the imposed lopsided model, different shapes in the pole count maps are to be expected. This will require a complex polar count maps analysis.

We also would like to implement a model for the flare of the galactic disc and apply it to our warp simulation and check how this can effect the kinematic signature of the warp and also the recovery of the geometrical parameters of the warp with the GC3 family of methods.

Regarding work with UCAC4 catalogue, we plan to apply the GC3 family of methods and analyse the results before and after correcting for the obtained residual spin of the reference frame. Moreover, we would like to check out the kinematic signature of the warp using a younger population namely early A type stars and compare their μ_b trend to the one we expect from our A star mock catalogue. For doing this, we will cross-match this catalogue with IPHAS catalogue and using the method described in Drew et al. (2008) select its early A stars.

A

The generation of the Initial Conditions

The initial conditions follow the density distribution of the Miyamoto & Nagai (1975) disc, because this is the density distribution chosen in Allen & Santillan (1991) to characterise the disc of the Galaxy. The fact that the parameters of the disc defining the initial conditions are the same as the disc of the axisymmetric component used in the integration facilitates the relaxation of the particles. Particles generated using a mass distribution similar to the mass distribution imposed in the integration reach statistical equilibrium faster. The initial conditions are generated using the Hernquist method (Hernquist 1993). Here we summarize the steps:

A.1 Radial distribution

We first compute the normalized cumulative distribution function

$$\Sigma(R) = \frac{1}{\Sigma_0} \int_0^R \Sigma^*(R')dR', \tag{A.1}$$

where $\Sigma^*(R) = R\int_{-\infty}^{+\infty} \rho(R,z)dz$ is the probability distribution function in cylindrical coordinates for the radial component, Σ_0 is the normalization constant, taken as $\Sigma_0 = \int_0^{+\infty} \Sigma^*(R')dR'$, and $\rho(R,z)$ is the density of the Miyamoto-Nagai disc.

Once we have the cumulative probability distribution function for the radial coordinate, we use its inverse to transform a sample of random numbers with uniform probability into a sample that follows the probability distribution function given by Σ^* (see **??**, section 7.2). Once we

have the galactocentric distance of the star, R, we can obtain the Cartesian coordinates (x, y) by generating a random azimuth in the interval $[0, 2\pi)$ with uniform probability and then converting back to Cartesian coordinates.

A.2 Vertical distribution

The generation of the vertical coordinate z is performed in a similar way as in § A.1. The distribution function in z is derived from the integration of the vertical Jeans equation, for the particular case when $\sigma_z^2 = \sigma_z^2(R)$, i.e. the vertical velocity dispersion only depends on R. For a given radius, R, the probability distribution function for the coordinate z is

$$\nu(R, z) = e^{\Delta\Phi(z)/\sigma_z^2(R)}, \tag{A.2}$$

where $\Delta\Phi(z) = \Phi(R, 0) - \Phi(R, z)$ and $\Phi(R, z)$ is the Miyamoto- Nagai potential, and $\sigma_z^2(R)$ is the vertical velocity dispersion taken as, $\sigma_z^2(R) = \pi G z_0 \Sigma(R)$, where z_0 is the scale-length in z, considered constant here (as a first approximation of the solution) and $\Sigma(R)$ is the Miyamoto-Nagai surface density, computed numerically.

To randomly obtain the coordinate z, we use the Von Neumann Rejection Technique using this probability distribution function (Press et al. 1992).

Notice that, since we are using the vertical Jeans equation with no cross terms in R-z and with an isothermal closure relation, the density given by Eq. A.2 is not self-consistent with the density of the A&S model, but should be a reasonable approximation to an isothermal population in statistical equilibrium with it. This is enough for our purposes, as we will subsequently relax our ensemble of test particles by integrating them in the fixed, A&S potential until statistical equilibrium is achieved.

A.3 Generating the velocities

Now we need to generate the velocities associated to the positions already obtained. First we define the radial, tangential and vertical dispersions.

For the radial velocity dispersion (σ_U), we set it proportional to the square root of the local surface density and normalise it at the solar neighborhood:

$$\sigma_U(R) = \sigma_U(R_\odot) \left(\frac{\Sigma(R)}{\Sigma(R_\odot)} \right)^{1/2}. \tag{A.3}$$

Note that we are assuming that the radial scale-length is double that of the density distribution.

The tangential velocity dispersion, σ_V, is determined by assuming the epicyclic approximation, that is:

$$\frac{\sigma_V^2(R)}{\sigma_U^2(R)} = \frac{\kappa^2}{4\Omega^2}, \tag{A.4}$$

where κ is the epicyclic frequency, and Ω is the angular frequency, computed from the rotation curve of the A&S potential.

Finally, the vertical velocity dispersion, σ_W, is also set to proportional to the square root of the surface density. This expression comes from the Jeans and Poisson equations, together with the Eddington approximation (no coupling between R and z) and isothermality in the vertical direction, that is σ_W is independent of z.

$$\sigma_W(R) = \left(\pi G z_0 \Sigma(R)\right)^{1/2}, \tag{A.5}$$

where z_0 is the scale-height of the disc, here considered constant, and $\Sigma(R)$ is the surface density of the Miyamoto-Nagai disk.

We now generate the residual velocity components of each particle at position (R, z) with respect to the Regional Standard of Rest, (U, V, W), using a Gaussian with the respective velocity dispersions. However, there is one final step to consider. We need to add the circular velocity, according the A&S potential, and subtract the asymmetric drift to the tangential component. The asymmetric drift is approximated as (Binney & Tremaine 2008)

$$V_a = \frac{1}{2V_c}\left[\left(\frac{\kappa^2}{4\Omega^2} - 1 - \frac{R}{\Sigma}\frac{\partial \Sigma'}{\partial R}\right)\sigma_U^2 - R\frac{\partial \sigma_U^2}{\partial R}\right], \tag{A.6}$$

where Σ' is the Miyamoto-Nagai density cut at $z = 0$ and V_c is the circular velocity both at the given radius R.

B

Distinguishing stars orbiting in the central part of the Galaxy using Lindblad diagram

B.1 Introduction to the Lindblad diagram

Lindblad (1933) introduced the use of energy vs. angular momentum diagram in identifying the general nature of the orbits. This diagram can be constructed for any spherical time independent potential. We can have orbits with energies between zero (unbounded condition) and ϕ_0 which is the center of the potential well. At a given energy, the angular momentum of orbits can vary between zero, which is the case for radial orbits, and a maximum value given by the energy of the circular orbit with that energy. Moreover, at a given angular momentum, the minimum energy that a particle can have is the energy of a circular orbit.

In Fig. B.1, we present the Lindblad diagram for a Plummer potential. The red curve shows the location of circular orbits. Only points below this curve can represent real physical orbits. Notice that the angular momentum of circular orbits diverges as the energy goes to zero. We will then build the *characterictic parabola* that is the locus of all orbits that pass through a given radius with null radial velocity. In other words, it describes all orbits that touch, without crossing, a given radial position, R_0. This is shown with brown curve in Fig. B.1. The characterictic parabola help us better understand the shape of the orbits. Point A represents an orbit with zero angular momentum, which therefore is a radial orbit with an apocenter equal to R_0. At point B, it shows a circular orbit of radius R_0. In between these two points, there exist all the elliptical orbits with the apocenter at R_0 and pericenters between zero to R_0. As moving

further away from point B, on the brown curve, we get the elliptical orbits with the pericenter equal to R_0 and apocenters that goes beyond. As seen in the figure, the characteristic parabola divides the region of allowed orbits into three different zones. Zone I, in green, is occupied by all orbits that are entirely contained within the R_0 spherical shell. Zone II, in pink, represents orbits that cross this shell of $R = R_0$. Finally, zone III, in blue, is populated by all orbits that lie entirely outside this shell. More details on this topic can be found in Aguilar (2008).

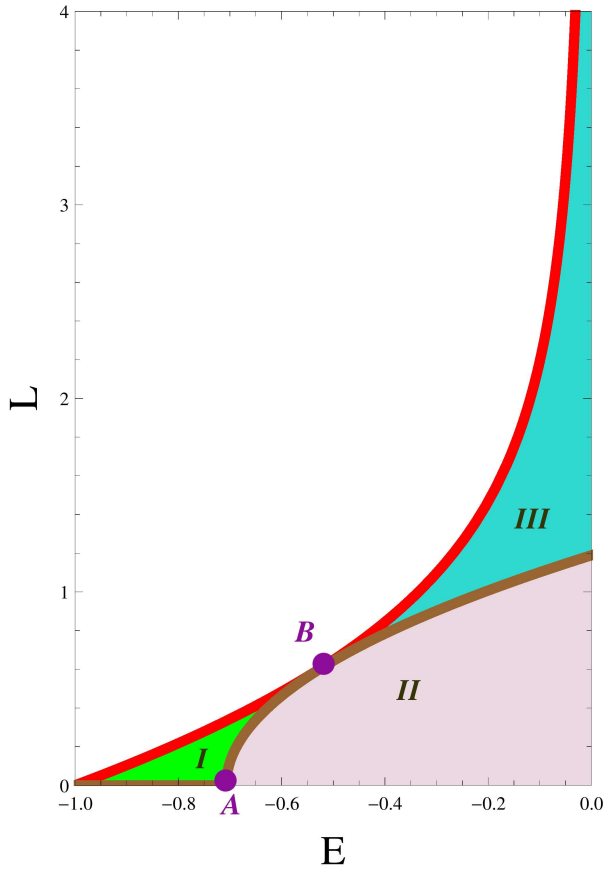

Figure B.1: Lindblad diagram for a Plummer potential. The horizontal axis is the dimensionless orbital energy and the vertical axis is the dimensionless orbital angular momentum. The red curve is the location of circular orbits. The points lie under this curve represent physical orbits. The brown curve is the characteristic parabola for R_0.

B.2 Application of Lindblad diagram to our simulations

Throughout this thesis, we have studied the Galactic warp which is a feature of the edge of the Galactic disc. We know from observations that the warp of MW starts at Galactocentric radii larger than 8 kpc (Reylé et al. 2009). Therefore, in our test particle simulations of the warp, stars that are located in $R < 8$ kpc do not interest us. In order to avoid integrating these stars and save some CPU time, we use Lindblad diagram to remove the stars whose apocentre radius is smaller than 8 kpc. As mentioned before, the Lindblad diagram can only be constructed for spherical potential. Whereas, the Galactic potential we use in this thesis is the A&S potential which is an axisymmetric potential. In this case, using the Lindblad diagram can approximately give us a rough identification of the orbits in this potential.

In order to identify stars with apocenter radius of 8 kpc and smaller, we should consider the characteristic parabola at this radius as schematically plotted in Fig. B.2 with a brown curve. As explained in the previous section, the points in brown curve between point A and B represent elliptical orbits with the apocenter equal to 8 kpc. All the area coloured in yellow correspond to orbits with apocenters smaller than 8 kpc, similar to zone I in Fig. B.1. In order to remove all the stars located in this yellow region from our test particle sample, we simply discard stars whose angular momentum is larger than the one described by the characteristic parabola at $R = 8$ kpc. The latter angular momentum is calculated as follows:

$$L_p(E) = \sqrt{2R_0^2\,(E - \phi(R_0))} \tag{B.1}$$

Where E is the total energy of each orbit and $\phi(R_0)$ is the potential energy of the $A\&S$ potential at the Galactocentric radius of R_0 which consists of: $\phi(R_0) = \phi_{disk}(R_0) + \phi_{bulge}(R_0) + \phi_{halo}(R_0)$.

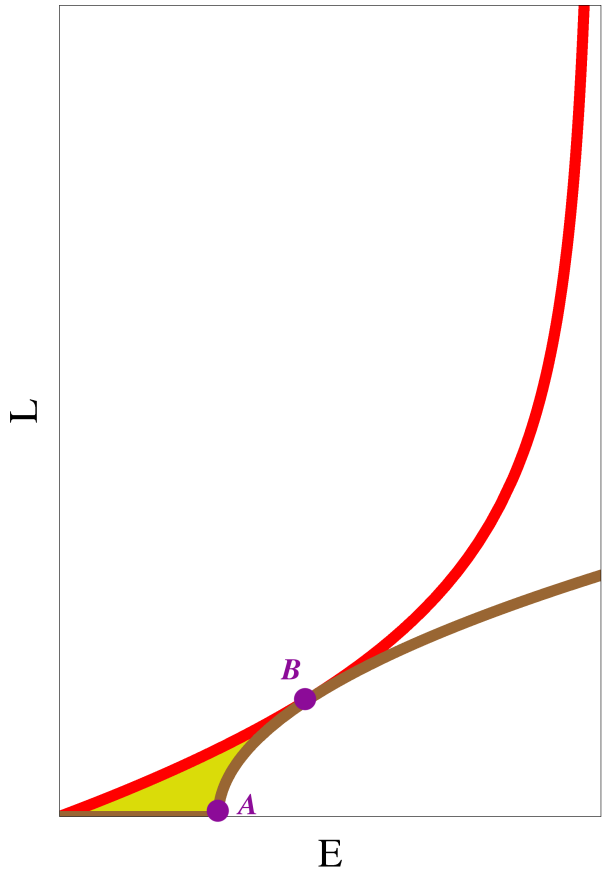

Figure B.2: Schematic plot of a Lindblad diagram. The horizontal axis is the dimensionless orbital energy and the vertical axis is the dimensionless orbital angular momentum. The red curve is the location of circular orbits at $R = 8$ kpc. The brown curve is the characteristic parabola for the same radius. The region coloured in yellow represents orbits with apocenteric radii smaller than 8 kpc.

C

The effect of Perlas 3D spiral arms on the kinematic signature of the warp

C.1 Introduction

We want to study how spiral arms can modify the kinematic signatures of the Galactic warp. This study can help us to predict what should we be expecting when studying the warp using the future Gaia data. As already mentioned before, the most significant effect of the warp can be seen in the vertical motion of stars (see Chapter 5). Therefore, its kinematic signature can be studied from W velocity component and the μ_b Galactic proper motion. In order to check how spiral arms can affect this signature, we need a three dimensional model for them. We decided to use Perlas model (Pichardo et al. 2003) where they modeled a three-dimensional Galactic spiral arms as a superposition of inhomogeneous oblate spheroids. We perform a test particle simulation with Perls spiral arms and then we study the effect of spirals on the vertical velocity component as well as the μ_b Galactic proper motions.

C.2 Perlas spiral arms

In the following we explain the initial parameters we use for simulating the spiral arms with Perlas model, most of them are obtained from Antoja et al. (2011) to mimic the real Milky Way spiral arms.

- The pitch angle of spiral arms is 12 degrees,
- Spiral arms start at Galactocentric distance of $R_s = 2.6\,kpc$,
- The superposition of spheroids begins at the distance $R_i = 3.3\,kpc$,
- The semi major axis of the oblate spheroids is $a_0 = 1\,kpc$,
- The semi minor axis of the oblate spheroids is $c_0 = 0.5\,kpc$,
- The separation of spheroid centers along the spiral locus is $a_k = 0.5\,kpc$,
- The ratio of the total mass in the spiral arms to the mass of the disk is taken to be $M_s/M_D = 0.05$ (realistic case) and 0.5 (non realistic case, adapted to exaggerate the effects),
- The distance at which the spiral arms are truncated is $R_f = 12\,kpc$,
- The pattern speed of spiral arms is taken to be $\Omega_p = 20\,km\,s^{-1}\,kpc^{-1}$.

C.3 Methodology

For this study we will consider a flat case, where we analyze the kinematic signatures of spiral arms in a flat disc. The conclusions of this analysis will be extrapolated to our warped case. Simulations with spiral arms potential will be compared to the axisymmetric case called case A here after.

C.4 Test particle simulations

In table C.1, we summarized the characteristics of the simulations we performed and used for this chapter. We simulate Perlas spiral arms for two case, one with a realistic mass, $M_s/M_D = 0.05$ (model B), and other with an exaggerated mass, $M_s/M_D = 0.5$ (model C). We introduce case C to see the most exaggerated effect of spiral arms on the parameters we are interested in. Note that in column named integration strategy, we present the integration time in terms of P which is the orbital period of a particle at 20 kpc. Integration time for case B and C are simply 2P$\sim$ 1 Gyr in the axisymmetric potential (A&S potential) and then, another 5P$\sim$ 2.5 Gyr of growing spiral arms. We use the initial conditions whose kinematics mimics the one of the red clump stars (see Sec. 4.1).

Running simulations with Perlas model requires a lot of CPU time and for the moment we perform the simulation for a small sample of about one million particles. We think even by having this few particles in simulations B and C, we can fulfill our aim to check whether 3D spiral arms produce any specific features on μ_b and W trends.

In figure C.1, we plot the X-Y and X-Z distribution of the particles after integration in case C together with the spiral arms locus. We can see that for this exaggerated case the spiral arms follow the locus. Note that in the simulations we run with spiral arms, for simplicity, we assume that the the bar (that determines the starting position of the arms) is located on the X axis and the inclination of the bar with respect to the Sun- Galactic center line is zero (Sun is located on the negative X axis). Since here we do not want to quantify the effect of spiral arms and we do not care about the central parts of the Galaxy, this assumption will not cause us any problems. Furthermore, with this geometry in the direction of anti-center we have the outer spiral arms at about 2 kpc from the Sun. This also mimics what we think is the real case for Perseus spiral arm. Also note that in bottom panel, these exaggerated spiral arms provoke the stars to get higher dispersion and therefore a higher disc scale height is induced. This is due to time dependent vertical forces of the Perlas spiral arms. This effect is more dominant in case C compared to case B, because spiral arms are more massive .

Model	**Integration strategy**	**Potential model**	**Conditions particles should satisfy**	**Number of accepted particles**
A	*2P*	*A&S*	*Lindblad cut at 8 kpc*	$\sim 10^6$
B	*2P+5P*	*A&S with Perlas spiral arms with* $M_s/M_D = 0.05$	*Lindblad cut at 8 kpc*	$\sim 10^6$
C	*2P+5P*	*A&S with Perlas spiral arms with* $M_s/M_D = 0.5$	*Lindblad cut at 8 kpc*	$\sim 10^6$

Table C.1: A summary of the simulations used

As mentioned in the table C.1, we perform a Lindblad cut for removing stars orbiting in the central part of the Galaxy before starting the integration (See Appendix B).

In the following sections we study the effect of spiral arms on W component and μ_b proper motion that are the most important parameters reflecting the kinematic signature of the warp.

C.5 Effect of Perlas spiral arms on μ_b and W

In Fig. C.2 we plot the mean values of Galactic proper motion μ_b in bins of 36 degrees in longitude. This trend is calculated for Galactocentric radial bins from 9 to 16 kpc, with a width of 1 kpc. The error bars represent the standard error of the mean. In top panel, we plot it for case B and in bottom panel we show the results for model C. Note that the the proper motions are corrected for the vertical motion of the Sun. We already know from Fig. 5.4 bottom panel,

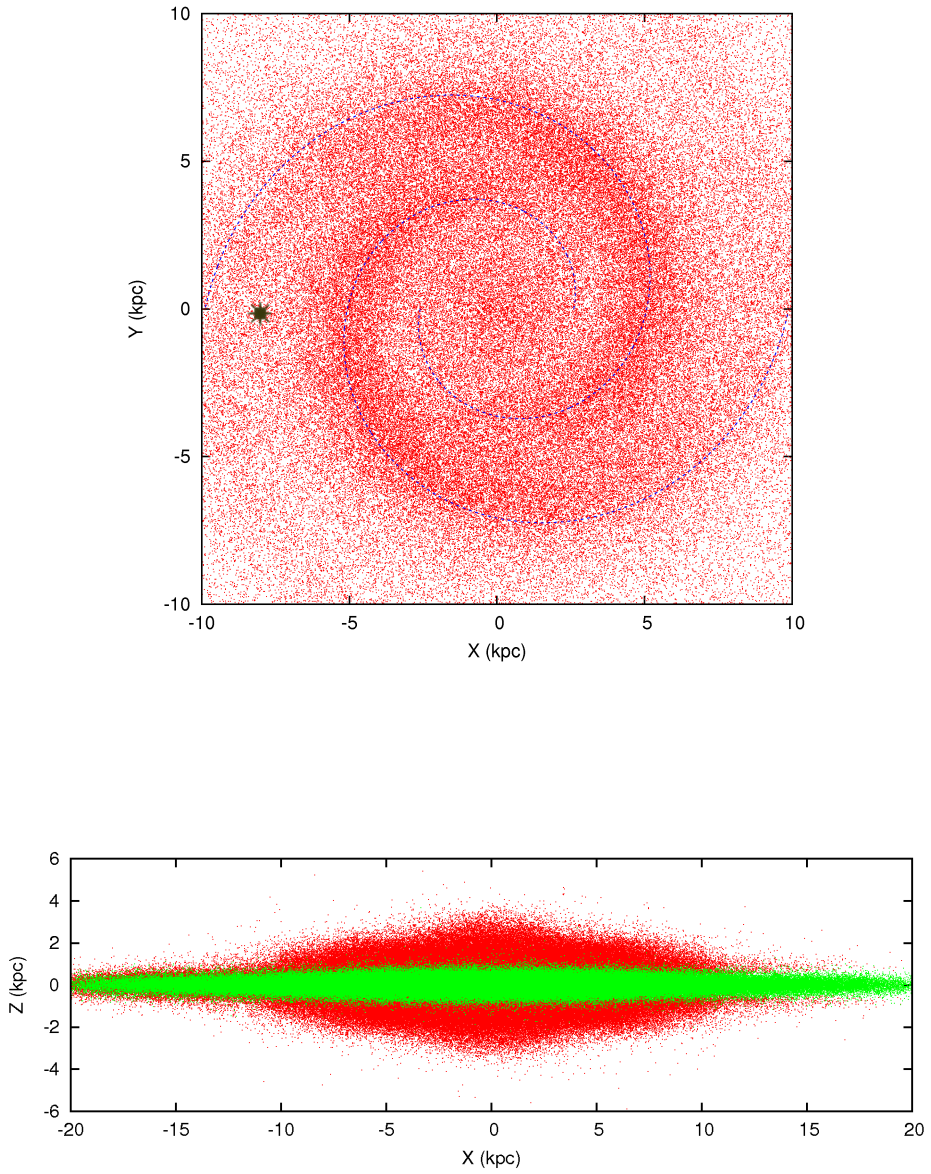

Figure C.1: Top: The x-y distribution of the particles in model C (exaggerated spirals) together with the spiral arms locus (the blue dashed lines). Bottom: the x-z distribution of particles, red points represents model C and green points represents model A (axisymmetric case). We clearly see how the exaggerated spiral arms have induced a higher scale height to the disc particles.

that for the the axisymmetric case (model A), the μ_b has a constant, zero trend.

From Fig. C.2, Looking at the errorbars, we can justify the observed differences between models B and C and model A. We can see that for both model B and C, for $r > 10$ kpc, there is a very small change of $\sim$0.1 masyr^{-1}, in the mean values when having spiral arms compared to the axisymmetric case. However, this difference lies within the error bars.

For $9 < r < 10$ kpc, For model B, the case with realistic spirals, we again can not see any systematic trend. And for model C, with the exaggerated spiral arms, the effects are at the 1-2σ level. This should be due to the presence of a strong spiral arm at this radius bin which can clearly be observed in Fig. C.1 top panel. As mentioned before, this can be the position of the Perseus spiral arm.

In figure C.3, we plot the mean values of W component as a function of longitude for models B (top panel) and C (bottom panel). Here, again, the W velocity has been corrected for the vetical motion of the Sun. From Fig. 5.2 bottom panel, we know that model A has a zero constant trend for W. As we expected, we can see that in the exaggerated case (model C) the difference from case A is bigger than the one for realistic case (model B). This should be due to the fact that spiral arms increase the scale height of the disk, and the more massive they are, the effect is more significant. Moreover, for model C, for $9 < r < 10$ kpc the spiral arms affect the w trend in 3σ level. Here, the largest discrepancy between model A and model C can be observed towards l$\sim 230^\circ$ which is about 2.5 kms^{-1}.

Although it seems that we need to integrate more particles to reach a final conclusions, But looking at the realistic spiral arms model, we can see that the most significant effect can be seen in Galactocentric radial bin of $9 < r < 10$ kpc which is in the order of $\sim$0.1 masyr^{-1}, while the signature of the warp at this radius can reach up to $\sim$0.4 masyr^{-1} (see Fig. 5.5 bottom panel). This trend for the case C, with 10 times more massive spiral arms, can have an amplitude comparable to the one of the warp. Therefore, we can predict that spiral arms do not have a significant effect on the kinematic signature of the Galactic warp. Moreover, we have checked that after applying the Gaia selection function to both of the samples of model B and C (as explained in Sec. 7.2.1), the results does not change significantly.

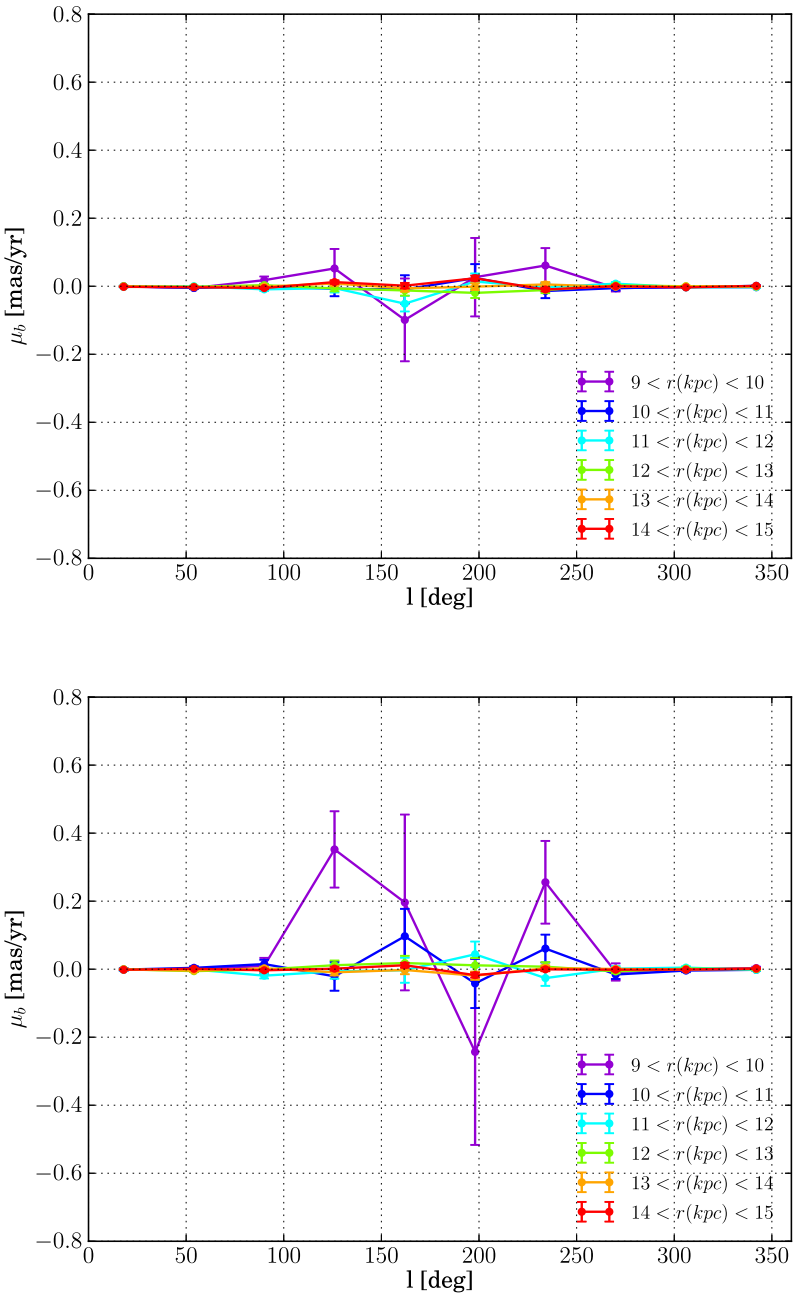

Figure C.2: The mean μ_b proper motion as a function of Galactic longitude for different Galactocentric radius bins for the simulation with Perlas spiral arms. Top panel shows the results of model B and in the bottom panel the results of model C are presented (see Tab. C.1). The error bars show the standard error of the mean. Note that the proper motions are corrected for the vertical motion of the Sun.

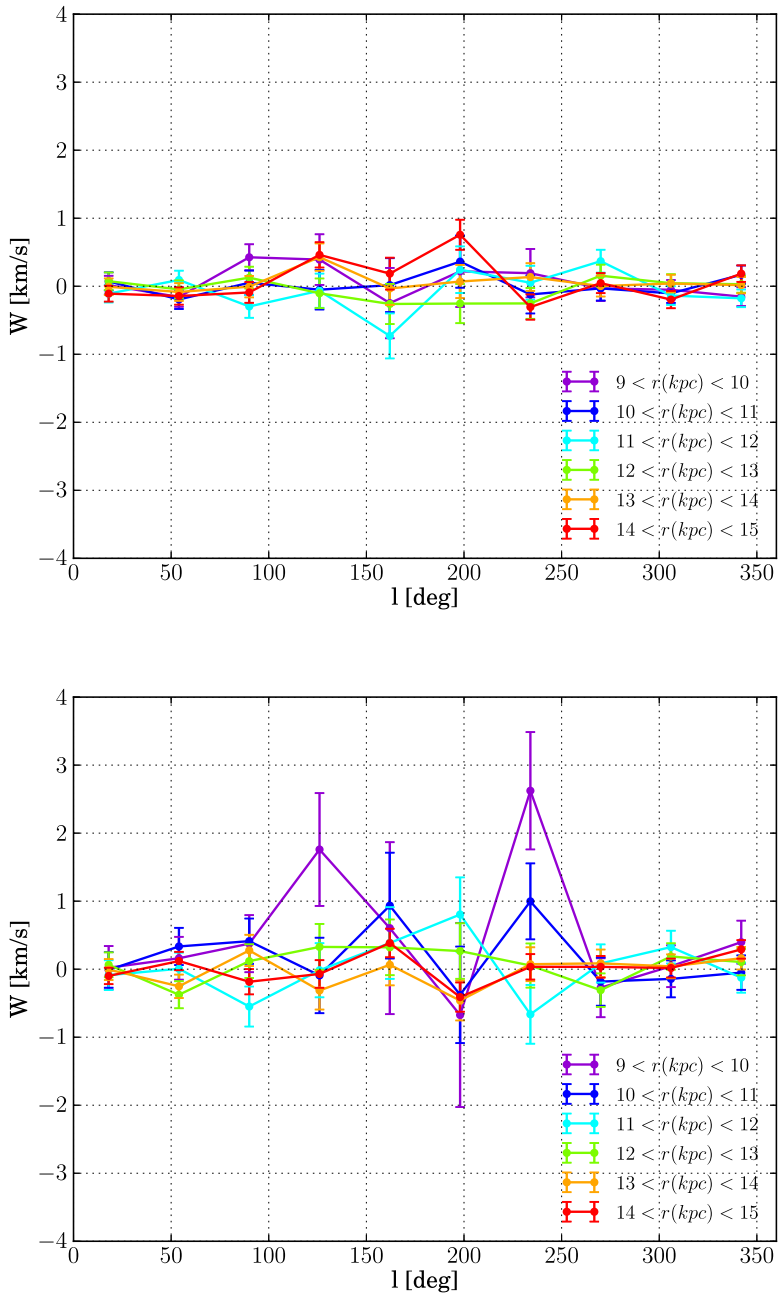

Figure C.3: The mean W velocity component as a function of Galactic longitude for different Galactocentric radius bins for the simulation with Perlas spiral arms. Top panel shows the results of model B and in the bottom panel the results of model C are presented (see Tab. C.1). The error bars show the standard error of the mean. Note that the velocities are corrected for the vertical motion of the Sun.

References

Aguilar L. A., 2008, in Plionis M., López-Cruz O., Hughes D., eds, A Pan-Chromatic View of Clusters of Galaxies and the Large-Scale Structure Vol. 740 of Lecture Notes in Physics, Berlin Springer Verlag, Dynamics of Galaxies and Clusters of Galaxies. p. 71

Allen C., Santillan A., 1991, Rev. Mexicana Astron. Astrofis., 22, 255

Alves D. R., 2000, ApJ, 539, 732

Antoja T., Figueras F., Romero-Gómez M., Pichardo B., Valenzuela O., Moreno E., 2011, MNRAS, 418, 1423

Aumer M., Binney J. J., 2009, MNRAS, 397, 1286

Bailin J., 2003, ApJ, 583, L79

Binney J., 1992, ARA&A, 30, 51

Binney J., Merrifield M., 1998, Galactic Astronomy

Binney J., Tremaine S., 2008, Galactic Dynamics: Second Edition. Princeton University Press

Boboltz D. A., Fey A. L., Puatua W. K., Zacharias N., Claussen M. J., Johnston K. J., Gaume R. A., 2007, AJ, 133, 906

Bobylev V. V., 2010, Astronomy Letters, 36, 634

Bobylev V. V., 2013, Astronomy Letters, 39, 819

Bobylev V. V., Bronnikova N. M., Shakht N. A., 2004, Astronomy Letters, 30, 469

Bobylev V. V., Fedorov P. N., Bajkova A. T., Akhmetov V. S., 2010, Astronomy Letters, 36, 506

Bosma A., 1991, in Casertano S., Sackett P. D., Briggs F. H., eds, Warped Disks and Inclined Rings around Galaxies Warped and Flaring HI Disks. p. 181

Bovy J., Allende Prieto C., Beers T. C., Bizyaev D., et al. 2012, ApJ, 759, 131

Bovy J., Nidever D. L., Rix H.-W., Girardi L., Zasowski G., Chojnowski S. D., Holtzman J., Epstein C., Frinchaboy P. M., Hayden M. R., Rodrigues T. S., Majewski S. R., Johnson J. A., et al. 2014, ApJ, 790, 127

Briggs F. H., 1990, ApJ, 352, 15

Brown A. G. A., Velázquez H. M., Aguilar L. A., 2005, MNRAS, 359, 1287

Burke B. F., 1957, AJ, 62, 90

Burton W. B., 1988, The structure of our Galaxy derived from observations of neutral hydrogen. pp 295–358

Cabrera-Lavers A., Bilir S., Ak S., Yaz E., López-Corredoira M., 2007, A&A, 464, 565
Cardelli J. A., Clayton G. C., Mathis J. S., 1989, ApJ, 345, 245
Carney B. W., Aguilar L., Latham D. W., Laird J. B., 1990, AJ, 99, 201
Cox A. L., Sparke L. S., van Moorsel G., Shaw M., 1996, AJ, 111, 1505
Czekaj M. A., Robin A. C., Figueras F., Luri X., Haywood M., 2014, A&A, 564, A102
Dehnen W., 2000, AJ, 119, 800
Dormand J. R., Prince P. J., 1981, Journal of Computational and Applied Mathematics, 7, 67
Drew J. E., Greimel R., Irwin M. J., Sale S. E., 2008, MNRAS, 386, 1761
Drimmel R., Cabrera-Lavers A., López-Corredoira M., 2003, A&A, 409, 205
Drimmel R., Smart R. L., Lattanzi M. G., 2000, A&A, 354, 67
Dubinski J., Kuijken K., 1995, ApJ, 442, 492
Fedorov P. N., Akhmetov V. S., Bobylev V. V., 2011, MNRAS, 416, 403
Fedorov P. N., Myznikov A. A., Akhmetov V. S., 2009, MNRAS, 393, 133
Foreman-Mackey D., Hogg D. W., Lang D., Goodman J., 2013, PASP, 125, 306
Fricke W., Schwan H., Lederle T., Bastian U., Bien R., Burkhardt G., Du Mont B., Hering R., Jährling R., Jahreiß H., Röser S., Schwerdtfeger H.-M., Walter H. G., 1988, Veroeffentlichungen des Astronomischen Rechen-Instituts Heidelberg, 32, 1
García-Ruiz I., Kuijken K., Dubinski J., 2002, MNRAS, 337, 459
Geffert M., Klemola A. R., Hiesgen M., Schmoll J., 1997, A&AS, 124, 157
Goodman J., Weare J., 2010, Communications in Applied Mathematics and Computational Science, 5, 65
Hernquist L., 1993, ApJS, 86, 389
Hirte S., Schilbach E., Scholz R.-D., 1997, A&AS, 126, 31
Hogg D. W., Bovy J., Lang D., 2010, ArXiv e-prints
Hunter C., Toomre A., 1969, ApJ, 155, 747
Jansky K. G., 1933, Nature, 132, 66
Jiang I.-G., Binney J., 1999, MNRAS, 303, L7
Johnston K. V., Hernquist L., Bolte M., 1996, ApJ, 465, 278
Jordi C., Gebran M., Carrasco J. M., de Bruijne J., Voss H., Fabricius C., Knude J., Vallenari A., Kohley R., Mora A., 2010, A&A, 523, A48
Kenyon S. J., Hartmann L., 1995, ApJS, 101, 117
Kerr F. J., Hindman J. V., Carpenter M. S., 1957, Nature, 180, 677
Kislyuk V. S., Rybka S. P., Yatsenko A. I., Kharchenko N. V., 1997, A&A, 321, 660
Klemola A. R., Hanson R. B., Jones B. F., 1994, in Morrison L. V., Gilmore G. F., eds, Galactic and Solar System Optical Astrometry Lick NPM program: NPM1 Catalog and its applications. p. 20
Kovalevsky J., Lindegren L., Perryman M. A. C., Hemenway P. D., Johnston K. J., Kislyuk V. S., Lestrade J. F., Morrison L. V., Platais I., et al. 1997, A&A, 323, 620

Kuijken K., Garcia-Ruiz I., 2001, in Funes J. G., Corsini E. M., eds, Galaxy Disks and Disk Galaxies Vol. 230 of Astronomical Society of the Pacific Conference Series, Galactic Disk Warps. pp 401–408

Levine E. S., Blitz L., Heiles C., 2006, ApJ, 643, 881

Lindblad B., 1927, MNRAS, 87, 553

Lindblad B., 1933, Handbuch der Astrophysik, 5, 937

Lindegren L., Kovalevsky J., 1995, A&A, 304, 189

López-Corredoira M., 2014, A&A, 563, A128

López-Corredoira M., Abedi H., Garzón F., Figueras F., 2014, A&A, 572, A101

López-Corredoira M., Betancort-Rijo J., Beckman J. E., 2002, A&A, 386, 169

López-Corredoira M., Cabrera-Lavers A., Garzón F., Hammersley P. L., 2002, A&A, 394, 883

Lynden-Bell D., 1965, MNRAS, 129, 299

Mateu C., Bruzual G., Aguilar L., Brown A. G. A., Valenzuela O., Carigi L., Velázquez H., Hernández F., 2011, MNRAS, 415, 214

Mignard F., 2001, in Proc Journées Système de Reférence Astronomical Society of the Pacific Conference Series, From Gaia Frame to ICRF3. pp 53–57

Miyamoto M., Nagai R., 1975, PASJ, 27, 533

Miyamoto M., Zhu Z., 1998, AJ, 115, 1483

Momany Y., Zaggia S., Gilmore G., Piotto G., Carraro G., Bedin L. R., de Angeli F., 2006, A&A, 451, 515

Mottram J. C., Hoare M. G., Davies B., Lumsden S. L., Oudmaijer R. D., Urquhart J. S., Moore T. J. T., Cooper H. D. B., Stead J. J., 2011, ApJ, 730, L33

Murray C. A., Penston M. J., Binney J. J., Houk N., 1997, in Bonnet R. M., Høg E., Bernacca P. L., Emiliani L., Blaauw A., Turon C., Kovalevsky J., Lindegren L., Hassan H., Bouffard M., Strim B., Heger D., Perryman M. A. C., Woltjer L., eds, Hipparcos - Venice '97 Vol. 402 of ESA Special Publication, The Luminosity Function of Main Sequence Stars within 80 Parsecs. pp 485–488

Nelson R. W., Tremaine S., 1995, MNRAS, 275, 897

Oort J. H., 1932, Bull. Astron. Inst. Netherlands, 6, 249

Oort J. H., Kerr F. J., Westerhout G., 1958, MNRAS, 118, 379

Perryman M., Spergel D. N., Lindegren L., 2014, ApJ, 789, 166

Peters III W. L., 1975, ApJ, 195, 617

Pichardo B., Martos M., Moreno E., Espresate J., 2003, ApJ, 582, 230

Press W. H., Teukolsky S. A., Vetterling W. T., Flannery B. P., 1992, Numerical recipes in FORTRAN. The art of scientific computing

Reylé C., Marshall D. J., Robin A. C., Schultheis M., 2009, A&A, 495, 819

Robin A. C., Reylé C., Derrière S., Picaud S., 2003, A&A, 409, 523

Roeser S., Demleitner M., Schilbach E., 2010, AJ, 139, 2440

Romero-Gómez M., Figueras F., Antoja T., Abedi H., Aguilar L., 2015, MNRAS, 447, 218

Sánchez-Saavedra M. L., Battaner E., Guijarro A., López-Corredoira M., Castro-Rodríguez N., 2003, A&A, 399, 457

Schmidt M., 1956, PhD thesis, Leiden Observatory, Leiden University, P.O. Box 9513, 2300 RA Leiden, The Netherlands

Schönrich R., Binney J., Dehnen W., 2010, MNRAS, 403, 1829

Sellwood J. A., 2013, Dynamics of Disks and Warps. p. 923

Shapley H., 1917, ApJ, 45, 118

Shapley H., Curtis H. D., 1921, Bulletin of the National Research Council, Vol. 2, Part 3, No. 11, p. 171-217, 2, 171

Shapley H., Shapley M. B., 1919, ApJ, 50, 42

Shen J., Sellwood J. A., 2006, MNRAS, 370, 2

Sparke L. S., Casertano S., 1988, MNRAS, 234, 873

Straižys V., Lazauskaitė R., 2009, Baltic Astronomy, 18, 19

Toomre A., 1983, in Athanassoula E., ed., Internal Kinematics and Dynamics of Galaxies Vol. 100 of IAU Symposium, Theories of WARPS. pp 177–185

van Leeuwen F., 2007, A&A, 474, 653

Véron-Cetty M.-P., Véron P., 2010, A&A, 518, A10

Vondrak J., Ron C., Pesek I., 1997, A&A, 319, 1020

Weinberg M. D., Blitz L., 2006, ApJ, 641, L33

Westerhout G., 1957, Bull. Astron. Inst. Netherlands, 13, 201

Xue X. X., Rix H. W., Zhao G., Re Fiorentin P., Naab T., Steinmetz M., van den Bosch F. C., Beers T. C., Lee Y. S., Bell E. F., Rockosi C., Yanny B., Newberg H., Wilhelm R., Kang X., Smith M. C., Schneider D. P., 2008, ApJ, 684, 1143

Zacharias N., Finch C. T., Girard T. M., Henden A., Bartlett J. L., Monet D. G., Zacharias M. I., 2013, AJ, 145, 44

Zasowski G., Johnson J. A., Frinchaboy P. M., Majewski S. R., Nidever D. L., Rocha Pinto H. J., Girardi L., Andrews B., Chojnowski S. D., et al. 2013, AJ, 146, 81

Zhu Z., 2001, PASJ, 53, L33

List of Figures

List of Tables